Theoretical study of electronic transport in TCV ELMy H-mode

Gaël Induni

gael.induni@epfl.ch

Master's thesis

Supervisor:
Olivier Sauter
olivier.sauter@epfl.ch

April 14, 2011

Abstract

High-confinement mode (H-mode) is a promising reference scenario for ITER. But we are still facing major issues because of instabilities. They expel periodically some of the energy, which can damage the device. These instabilities are called the edge localized modes (ELM) and are not yet fully theoretically understood.

The present work is a study on the profiles evolution in between ELMs and on the ELM effects. This may help to have a better understanding of the conditions before the ELM. We use the simulations as theoretical tool.

For the purpose of the simulations, we build an H-mode χ_e profile according to a standard L-mode one that we truncate at the edge to create a transport barrier. This gives a good agreement with the experimental data.

Several scaling laws were successfully used. The first one is the energy confinement time scaling which was used for the thermal diffusivity to scale the temperature profile. A scaling between the core and pedestal energies was found recently. It was used to compute the pedestal χ_e to scale the temperature pedestal, which was successful. Finally, we used a scaling for transport barriers which links the density gradient length to that of the temperature to compute the density in the pedestal. It was already found to be good in TCV electron internal transport barriers and in ASDEX Upgrade H-mode pedestals.

Looking at the MHD stability parameters, it was found that for our reference case, ELMs are not likely to be triggered by the time evolution of the pressure gradient and the current density profiles in our model, as these are only varying significantly during the first millisecond after the crash, and are almost constant during the long remaining time until the next crash.

Studying different cases, we investigate the behavior of the plasma when replacing the edge heating by central one to observe the influence of the heating profile, but no significant difference was found, neither in the MHD stability parameters.

Further we change the particle diffusion coefficient to compare the dynamic behavior of the density. Slowing down the density dynamic behavior also slows down the pressure one, this can be seen on the MHD stability parameters. We also vary the ELM period to compare to the change due to the variation of the particle diffusivity. It was found that there may be a sort of relation between the particle diffusivity and the ELM period at least for the density, since both cases change the density recovery time with respect to the ELM period.

A last case considered is doubling the radial ELM interaction range. This is done in order to observe the difference to the reference simulation that takes the density top of pedestal as ELM range, and to compare the spatial range influenced by the MHD activity and the one by the transport improvement. It was found that the MHD stability parameters in the pedestal exhibit a different behavior with the pressure gradient starting to increase very fast.

Contents

Chapter 1

Introduction

Fusion may be our future source of energy. For now, we are not able to achieve it in an economically viable way because we do not understand fully what happens in our tokamaks. A long time ago, Lawson was also working on fusion research. He predicted that we will face some problems he did not know at that moment. This was very smart of him. He also predicted from where those problems will arise: "Conduction loss is difficult to treat in a general way, since it depends on the geometry of the system, its density and temperature distribution, and also the wall material." [1] Actually the wall material has not much to do with the losses, or indirectly. Nowadays we are facing problems coming from within the plasma, instabilities and turbulence.

As the research went further on fusion, we discovered some limitations to our reactors. Looking for a way to overcome them, it was once discovered in ASDEX a regime where the confinement is improved by about a factor two [2]. This was done twenty-nine years ago. This operation mode was not predicted, but it appeared for a sufficient input power. It is called the H-mode, standing for *High-confinement mode*, in opposition to the *Low-confinement mode* (L-mode). Since then this promising operational mode has been studied extensively.

We then discovered that one of the features of H-mode is the instabilities called edge localized modes (ELMs). ELMs expel periodically some particles and energy. They are somehow useful, because it helps the plasma expel the impurities, and not to increase too much the density. But there are many types of them, and some expel very large quantities of energy. The expelled particles and energy onto the vessel. This may cause destructive erosion of the plasma-facing components that could make the device not viable.

In order to have a better knowledge of the physics in H-mode, here is studied the electronic transport in the inter-ELM phase. This can be done through theoretical studies to avoid the machine deterioration. We will do a brief overview of the limits responsible for the ELMs, but this work focuses on the profiles evolution in between ELMs and on the ELM effects. This may help us to better understand the conditions before an ELM.

The next step in fusion research is being built in France, the famous International Thermonuclear Experiment Reactor (ITER). Its operational scenario is an ELMy H-mode. It is therefore of prime importance to have a better knowledge of the transport in the inter-ELM phase.

This work will first recall some theory basis that are needed. We will do an overview of the magnetohydrodynamics theory and instabilities. Then we will speak about the plasma confinement, more specifically of the transport phenomena, leading to the H-mode description. This study being theoretical, we then explain the tool used in this work and how the imple-

mentation has been achieved. Finally, different cases were studied and comparisons between these results are presented. We will study the inter-ELM profiles, time traces and the MHD stability diagrams.

Chapter 2

Magnetohydrodynamics

This chapter is not intended to provide a full description of the MagnetoHydroDynamics (MHD) but will only present the part that is necessary to understand this work. For further knowledge, the reader can refer to the books [3–6].

The ideal MHD is based upon conservation laws, the fluid equations and Maxwell's equations [3]. The MHD model is focusing on the characteristic scales of the macroscopic behavior of the plasma. It can be built from the two-fluid model (described in [3]), reducing it to a single-fluid one and completing it with electrodynamics.

The range of validity of ideal MHD is defined upon three parameters: the characteristic length, time and velocity [3]. They are respectively defined by the plasma radius, the ion thermal transit time across the plasma and the characteristic velocity defined by the ratio of the two previous parameters. Indeed, in ideal MHD it mainly depends on the plasma radius a and on the ion sound speed v_{T_i} because we define the characteristic time as $\tau = a/v_{T_i}$ and the velocity $u = a/\tau = v_{T_i}$.

Taking in consideration the electromagnetic quantities, it yields three conditions [3]:

Length $a \gg r_{L,i} \gg r_{L,e} \sim \lambda_{De}$

Frequency $\bar{\nu}_{ei} \ll \dfrac{1}{\tau} = \dfrac{v_{T_i}}{a} \ll \omega_{c,i}$

Velocity $v_{T_i} \ll v_{T_e} \ll c$

where r_L is the Larmor radius, λ_{De} the Debye length, $\bar{\nu}_{ei}$ the momentum exchange collision frequency and ω_c the cyclotronic frequency. There are some more conditions that fall from these, including that the plasma pressure has to be finite compared to the magnetic pressure, requiring $\beta = p/(B^2/2\mu_0) \sim 1$ [3].

Introducing the Alfvén velocity $v_A^2 = B^2/(\mu_o n_i m_i)$, it is approximately equal to $2v_{T_i}^2/\beta$, implying that the MHD characteristic timescale τ is the Alfvén time $\tau_A = a/v_A$ [4].

We introduce the single-fluid variables as the mass density ρ, the fluid (macroscopic) velocity $\mathbf{u}$ and the pressure [3]. Since a plasma relies on quasi-neutrality meaning $n_e = n_i = n$ and ions having a much larger mass than electrons $m_i \gg m_e$, the mass density is defined as $\rho = m_i n$ and the fluid velocity as $\mathbf{u} = \mathbf{v}_i$. The pressure being not so different for the two species, the fluid pressure is simply the sum of both contributions $p = p_i + p_e$.

Electrons and ions flowing in different directions, it creates a current, defined by the current

density $\mathbf{J} = en(\mathbf{v}_i - \mathbf{v}_e)$ which can be used to express the electron velocity as

$$\mathbf{v}_e = \mathbf{u} - \frac{\mathbf{J}}{en}$$

Using these variables in the two-fluid model, we can now write the ideal MHD equations [3]:

$$\text{Mass conservation} \qquad \frac{D\rho}{Dt} + \rho\, \nabla \cdot \mathbf{u} = 0 \tag{2.1}$$

$$\text{Momentum conservation} \qquad \rho\, \frac{D\mathbf{u}}{Dt} = \mathbf{J} \times \mathbf{B} - \nabla p \tag{2.2}$$

$$\text{Ohm's law} \qquad \mathbf{E} + \mathbf{u} \times \mathbf{B} = \eta \mathbf{J} \tag{2.3}$$

$$\text{Energy} \qquad \frac{D}{Dt}\left(\frac{p}{\rho^\gamma}\right) = 0 \tag{2.4}$$

$$\text{Maxwell} \qquad \begin{cases} \nabla \times \mathbf{E} &= -\dfrac{\partial \mathbf{B}}{\partial t} \\ \nabla \times \mathbf{B} &= \mu_0 \mathbf{J} \\ \nabla \cdot \mathbf{B} &= 0 \end{cases} \tag{2.5}$$

where $\gamma = 5/3$, and the convective derivative is expressed as

$$\frac{D}{Dt} = \frac{\partial}{\partial t} + (\mathbf{u} \cdot \nabla)$$

Treating the **ideal** MHD means we consider the plasma as an ideal conductor and therefore set $\eta = 0$, which drops the right-hand side term of (2.3).

What is interesting now is the behavior of such a system to a small perturbation. The full development can be found in [3,4]. It leads to the conclusion that the system is unstable if the change in potential energy δW is negative. With appropriate boundary conditions we can decompose it in a plasma, a surface and a vacuum contributions [4]:

$$\delta W = \delta W_P + \delta W_S + \delta W_V$$

Introducing the field curvature $\kappa = (\mathbf{b} \cdot \nabla)\mathbf{b}$ where $\mathbf{B} = B\mathbf{b}$, we can rewrite each vector quantity $\mathbf{d}$ as a component parallel to the toroidal field $d_{//}$ and a perpendicular one $\mathbf{d}_\perp$ which gives the relation $\mathbf{d} = d_{//}\mathbf{b} + \mathbf{d}_\perp$. Hence we may write the plasma contribution as [4]

$$\delta W_P = \frac{1}{2}\int_P \mathrm{d}V \left(\frac{B_{1,\perp}^2}{\mu_0} + \frac{B^2}{\mu_0}\left(\nabla \cdot \xi_\perp + 2\xi_\perp \cdot \kappa\right)^2 + \gamma\, p (\nabla \cdot \xi)^2 \right.$$
$$\left. - 2(\xi_\perp \cdot \nabla p)(\kappa \cdot \xi_\perp) - j_{//}(\xi_\perp \times \mathbf{b}) \cdot \mathbf{B}_{1,\perp} \right) \tag{2.6}$$

where the quantities without index are from the equilibrium whereas those with index 1 are the perturbed ones, $\mathbf{J} \simeq j_{//}\mathbf{b}$ and ξ is the perturbation displacement defined by

$$\xi(\mathbf{r}, t) = \xi(\mathbf{r}) e^{i\omega t} \tag{2.7}$$

We usually have no currents flowing on the plasma surface and thus the surface term vanishes. The δW_V represents the perturbed magnetic vacuum energy. An ideal conducting wall near the plasma has a stabilizing effect, as it is the vacuum region that destabilizes.

The plasma perturbed energy contains many terms. The two first ones are linked to the bending of the magnetic field lines. They are always positive and therefore stabilizing. The third term represents the energy needed by the plasma to be compressed, it is also a stabilizing term.

The last two terms are proportional to $\mathbf{j}$ and ∇p and thus can be either positive or negative. If negative, instabilities will arise. There are lots of them and they can be characterized in different ways. Those caused by the pressure gradient term are often called *pressure-driven* modes, while instabilities caused by the parallel currents are called *current-driven* modes [3,4]. This denomination means that those instabilities can arise even though the other destabilizing term does not act. For instance, current-driven modes can exist in the low β limit where all the pressure-modes are stabilized. Nevertheless, we usually have both pressure gradient and current density contributions together.

2.1 MHD stability parameters

With coordinates (R, ϕ, z) and using the relation $\mathbf{B} = \nabla \times \mathbf{A}$, we can define the *poloidal flux* $\psi = RA_\phi$, yielding $(\mathbf{B} \cdot \nabla)\psi = 0$ [4]. This means that the poloidal flux is constant along the magnetic surfaces and therefore ψ can be used as a coordinate. We can show after some algebra that surfaces of constant ψ are also surfaces of constant current and of constant pressure [4].

We define the ratio of change of the magnetic helicity in toroidal angle to that of the poloidal angle as [4]

$$q = \frac{1}{2\pi} \oint_{\substack{poloidal \\ circuit}} \mathrm{d}l \, \frac{B_t}{RB_p} \tag{2.8}$$

where B_t and B_p are respectively the toroidal and the poloidal magnetic field. The latter is created by the plasma current. This ratio can hence be seen as

$$q = \frac{\Delta\phi}{2\pi}$$

where $\Delta\phi$ is the change in toroidal angle for a change of 2π in poloidal angle along a magnetic surface. If q is rational, we can write $q = m/n$ where m and n are integers, meaning that the magnetic field lines join themselves after m toroidal revolutions and n poloidal ones. Hence the field lines are joining themselves after a finite number of revolutions. If we recall of (2.7), we can also see m and n as the poloidal and toroidal mode number respectively [7]:

$$\xi(\mathbf{r}) = \sum_{m,n} \hat{\xi}_{m,n}(r) e^{i(n\phi + m\theta)}$$

At a given equilibrium, q has a fixed profile, but the mode numbers can be numerous. This means that, at a given location, we have a variety of mode numbers for a single value of q, linking the toroidal mode number to the poloidal one by the relation $q = m/n$.

The instabilities following the field lines, we understand that the joining of the latter will help the instabilities to grow up. Thus rational values of q are dangerous for the plasma stability. This ratio q is an important parameter of MHD stability and is called the *safety factor*.

The shear of a vector $\mathbf{F}$ is defined as $\nabla\mathbf{F}$. The magnetic shear s is the shear of the safety factor. As the latter is radial and we are only interested in the radial direction, we define the

magnetic shear $s = s(\rho)$ as

$$s = \frac{\rho}{q}\frac{\mathrm{d}q}{\mathrm{d}\rho}$$

ρ being the radial coordinate. The higher the magnetic shear, the lower the radial transport. Thus high values of the shear have a stabilizing effect on the plasma.

2.2 Instabilities

Instabilities are numerous in the MHD theory. We do not intend to describe all of them in this work, but H-mode plasmas deal with some that may be recalled here.

Looking at (2.6), we have discussed the last two terms about their capability of destabilization. The first one concerns the pressure. If we have a pressure gradient ∇p and a magnetic field curvature κ in the same direction, we understand that this term will be destabilizing. Tokamaks have a curvature aimed at their center, and the pressure gradient is generally directed towards the center of the plasma. On the inner part of the tore, ∇p and κ are aiming at different directions. But looking at the outer part, both ∇p and κ are directed towards the center of the plasma. This yields that the destabilization-drive is mainly on the outer part and the perturbation amplitude tends to maximize them.

Such perturbations are called the *ballooning modes* in the $n \to \infty$ limit. The ballooning stability parameter is defined by the normalized pressure gradient

$$\alpha = -R_0 q^2 \frac{\mathrm{d}\beta}{\mathrm{d}r}$$

where R_0 is the major radius of the tokamak and r the metric radius of the plasma.

For finite n, we encounter some other modes called *external kink*. These modes are more difficult to understand, but the literature provides documentation, e.g. references [8,9]. Considering the second-order potential energy, the destabilizing term is the radial gradient of toroidal current density $\mathrm{d}j_t/\mathrm{d}r$ [8].

The origin of this term comes from the properties of the kink modes. They are incompressible and therefore need a torque to kink. The latter is provided by the $\mathbf{j} \times \mathbf{B}$ force. The torque being the curl of the force, the gradient of the current density appears in the torque, hence driving the instability. However, this term is also present in the magnetic shear, which has a stabilizing effect [8]. We must ask ourselves what are the conditions for this destabilizing force to become an instability.

Considering first no vacuum between the plasma and the wall, we find after some algebra that the destabilizing term in the potential energy is $j_{t,a}/\langle j_t \rangle$, the index a referring to the edge value and $\langle \cdot \rangle$ being the volume average. Thus the stability criterion in this limit is given by $j_{t,a} \leq 0$. This limit case is the same when the wall is further for $m \to \infty$ modes. Looking at finite high m modes, further analysis yields an additional stability criterion as

$$\left.\frac{\partial j_t}{\partial r}\right|_a = 0$$

The edge current density plays an important role for these modes [10]. In particular the bootstrap current (see §3.1) has a destabilizing effect on the external kink [7]. It is thus

understandable that H-mode will often have to face them because of the pressure pedestal which implies the arising of the edge pressure gradient and thus a finite edge current density.

In the H-mode regime, the most common instabilities are non-negligible. They are called edge localized modes (ELM). They are characterized by the emission of H_α radiation [6]. They are not yet fully understood but are believed to be due to the combination of the ballooning modes and the external kink [11].

There are many types of these ELMs but we will only discuss about type-I and type-III ELMs. The main difference between these two types is the occurrence of the ELMs according to the input power. Type-I ELMs increase their frequency with respect to the input power whereas type-III ELMs decrease theirs. Type-I ELMs are very large ELMs and are very dangerous for the plasma facing-components due to the large energy loss ($\Delta W/W \simeq 8 - 25\%$ [12]) that go directly onto the divertor plates [6]. The latter type being the most dangerous for the machine, this study is focused on them.

ELMs do not have a specific stability parameter but are studied using the stability parameters of both ballooning modes and external kink, respectively α and $j_{t,a}$. The proper way to observe the evolution of the plasma among the ELMs is using a diagram of $j_{t,a}$ as function of α, where we have a stability region for the plasma.

Another instability often present in tokamak plasmas is the sawtooth instability. It is an internal instability and is supposed to be due to the internal kink. This mode is described by $n = 1, m = 1$. This means the $q = 1$ surface plays an important role since the instability occurs inside it. We denote the radius of this surface by r_1. $q = 1$ is the surface where the magnetic toroidal angle is equal to the poloidal one, joining the field lines after a single revolution of the machine only. Therefore the small instabilities are allowed to grow very much because they follow the same magnetic field line for many revolutions.

Chapter 3

Plasma confinement

3.1 Transport

The transport of energy and particle are governed by the conservation laws [13,14]

$$\frac{\partial W_j}{\partial t} + \frac{1}{V'}\frac{\partial}{\partial \rho}\left(V' q_j\right) = S_j \qquad j = i, e \tag{3.1}$$

$$\frac{1}{V'}\frac{\partial}{\partial t}\left(V' n_e\right) + \frac{1}{V'}\frac{\partial}{\partial \rho}\left(V' \Gamma_n\right) = S_n \tag{3.2}$$

where $W_j = \frac{3}{2}\int \mathrm{d}V\ n_j T_j$ with $j = e, i$, S_j and S_n denote respectively the heat and particle sources and sinks, q_j and Γ_n the heat and particle fluxes and $V' = \frac{\partial V}{\partial \rho}$. The particle sources are mainly the gas injected, but also some interactions with the walls, thus it is localized at the edge of the plasma.

The heat sources are different whether we talk about the ions or the electrons. In the Tokamak à Configuration Variable (TCV), the electron heat sources are the ohmic heating and the electron cyclotron heating (ECH). There are no external ion heat source. Thus at TCV the electron temperature is higher than the ion temperature. Since this machine has dominant electron heating, the equipartition of energy (due to collisions) yields a source for the ions and a sink for the electrons. The heat sources are defined by [13]

$$S_e = P_{\mathrm{ohm}} + P_{\mathrm{ECH}} - n_e \nu_{ei}(T_e - T_i) - P_{\mathrm{rad}}$$
$$S_i = n_e \nu_{ei}(T_e - T_i) - P_{\mathrm{rad}}$$

The fluxes are given by the general equation [6]

$$\begin{pmatrix} \Gamma_n \\ q_e \\ q_i \end{pmatrix} = -\underline{\underline{A}} \begin{pmatrix} \nabla n_e \\ \nabla T_e \\ \nabla T_i \end{pmatrix}$$

where the diagonal elements of $\underline{\underline{A}}$ are the diffusion coefficients, D_n, $n_e\chi_e$ and $n_e\chi_i$. We usually assume that the heat fluxes depend mainly on the gradient of their species' temperature, which yields that the low-diagonal part of $\underline{\underline{A}}$ is null, and so is A_{23}. We thus can write the heat fluxes as

$$q_j = n_j \chi_j \nabla T_j \qquad j = i, e \tag{3.3}$$

On the other side, the particle flux may be somehow more complex thus much more difficult to compute, taking into account those crossed contributions. A simpler way to write it is

$$\Gamma_n = -D_n \nabla n_e + V_n n_e \tag{3.4}$$

where V_n is the pinch velocity and the convection term $V_n n_e$ could be seen as the contributions from the off-diagonal terms [6].

From a two-fluid model, we can compute the relation for the three diffusion coefficients [3]

$$D_n \sim \frac{\rho_{L,e}^2}{\bar{\tau}_{ei}} \qquad \chi_i \sim \frac{\rho_{L,i}^2}{\bar{\tau}_{ii}} \qquad \chi_e \sim \frac{\rho_{L,e}^2}{\bar{\tau}_{ee}} \tag{3.5}$$

where $\bar{\tau}_{ii}$ and $\bar{\tau}_{ee}$ are the mean time between collisions respectively for ions and for electrons, $\bar{\tau}_{ei}$ is the momentum exchange collision mean time and $\rho_{L,k}$ is the Larmor radius of species k.

This is valid for the classical transport. Toroidal geometry implies other effects. This is the neoclassical transport theory. In this theory, we decompose the vector quantities into a parallel component (scalar) along the magnetic field, and a perpendicular component (vectorial) which is the other part. For instance, the velocity becomes $\mathbf{v} = v_{//}\mathbf{b} + \mathbf{v}_\perp$. We do not need to redo the whole computation to find the new diffusion coefficient. From simple calculations arise correction factors to the classical coefficients [3], which we will not expand here.

Neoclassical theory also predicts a very interesting phenomenon that is the bootstrap current [3]. In a magnetic tore, the outside of the tore has a lower magnetic field than the inside, because the amplitude is inversely proportional to the major radius. We respectively speak of *low-field* and *high-field side* of the tokamak. Moreover, the total magnetic field is helical, meaning the particles will have elliptic poloidal paths. Thus they may be trapped in the low-field side if they do not have enough parallel velocity to overcome the magnetic barrier. The bootstrap current arises from this through subtle transport phenomena [3]. It flows parallel to the magnetic field and its magnitude can be larger than the ohmic current. An economically viable reactor needing at least a bootstrap fraction of 0.7, this phenomenon is very important for the future of fusion research.

To achieve fusion, it is important for the plasma to accumulate energy. Before we can do this, arises another problem: the energy is carried out of the plasma by radial heat and particle transport and we must keep it inside. We need a quantity which can tell us how well the energy is kept inside the plasma; this quantity is the energy confinement time τ_E defined by the energy balance equation [15]

$$\frac{\mathrm{d}W_P}{\mathrm{d}t} = P_{in} - \frac{W_P}{\tau_E} \tag{3.6}$$

where $W_P = W_e + W_i$. This yields the relation for the energy confinement time as

$$\tau_E = \frac{W_P}{P_{in} - \dfrac{\mathrm{d}W_P}{\mathrm{d}t}} \tag{3.7}$$

In steady-state we can write $W_P = \tau_E P_{in}$.

Contrary to what collisional transport theory predicts, the energy confinement time dependences have been observed to vary with the increase of the temperature [15]. We can build an empirical formula by taking all the data from every devices around the world, the scaling confinement time. This is an empirical law that is not fully theoretically understood. We have

many of them depending on which case we consider. For the standard ELMy H-mode (the reference scenario for ITER), we use the following [16]:

$$\tau_{\text{IPB98}(y,2)} = 5.62 \cdot 10^{-2}\ I_{\text{MA}}^{0.93}\ B_0^{0.15}\ n_{e,19}^{0.41}\ P_{\text{MW}}^{-0.69}\ R^{1.97}\ \kappa_a^{0.78} \left(\frac{a}{R_0}\right)^{0.58} M_{\text{amu}}^{0.19} \tag{3.8}$$

To compare the experimental results with this scaling, we introduce a factor that is the ratio of the two different confinement times $HH = \tau_E/\tau_{\text{IPB98}(y,2)}$. This scaling law depends on the input power too. We see that the exponent of the latter is around -0.7. Using the steady-state confinement time definition together with the scaling law, we get

$$W_P = \tau_E P_{in} \simeq \tau_{\text{IPB98}(y,2)} P_{in} = \hat{\tau} P_{in}^{0.31} \qquad \text{where } \hat{\tau} = \tau_{\text{IPB98}(y,2)} \cdot P_{in}^{0.69}$$

This means that the plasma energy is proportional to the input power at the exponent 0.3, thus requires a large amount of additional input power to increase not so much.

3.1.1 Characteristic timescales

There is a bunch of phenomena happening in a plasma. But they do not all happen on the same timescale. We are mainly dealing with four characteristic timescales.

The first one concerns the energy and is the governing timescale for the electron and ion temperatures. Its characteristic time is obviously the energy confinement time τ_E. It is generally a global value, but it can also be used locally with a great care. We can link this parameter to some other. Recalling of (3.1), we can consider that the stored energy is much more important than the source. Approximating that the volume derivative is constant along the plasma, the equation then becomes

$$\frac{\partial W_j}{\partial t} + \frac{\partial q_j}{\partial \rho} \simeq 0$$

Using the definition of the heat flux (3.3), we replace it in the above equation, then approximate the derivatives by finite small elements to obtain

$$\frac{\Delta W_j}{\Delta t} \simeq \frac{n_j \chi_j \nabla T_j}{\Delta r} \simeq \frac{n_j \chi_j T_j}{\Delta r^2} = \frac{\chi_j}{\Delta r^2} W_j$$

Taking $\Delta W/\Delta t \sim W/\tau_E$, this implies that

$$\tau_E \simeq \frac{\Delta r^2}{\chi_j} \qquad\qquad j = i, e \tag{3.9}$$

Another timescale concerns the particles and describes the behavior of the density. The previous equation says the timescale depends on the diffusion coefficient, we can guess it would be the same for the density. It yields

$$\tau_n \simeq \frac{\Delta r^2}{D_n} \tag{3.10}$$

where τ_n is the diffusion time.

There is a last timescale that will be spoken here. It concerns the current density and is the characteristic timescale for all the current densities. The plasma current is created by the loop

voltage and creates the poloidal magnetic field. Recalling of the definition of q (2.8), the latter is present in the definition of the safety factor and therefore also in the shear. The classical theory gives us the resistive characteristic time [4]

$$\tau_\eta \simeq \frac{\mu_0 \Delta r^2}{\eta} \tag{3.11}$$

where $\eta = m_e \bar{\nu}_{ei}/(e^2 n_e)$ is the plasma resistivity [3].

Recalling of the chapter on MHD, we defined the MHD timescale as the Alfvén time τ_A. The MHD conditions at the beginning gave us that $1/\tau_A \gg \bar{\nu}_{ei} \sim \nu_{ei}$. According that $\nu_{ei} \sim \nu_{ee} \gg \nu_{ii}$ [3] with $\nu_{jj} = 1/\tau_{jj}$, and using (3.5), it implies that $\tau_A \ll \tau_E, \tau_n, \tau_\eta$. The MHD is the fastest phenomenon among those considered in this work. The ELMs will occur on a timescale much shorter than the recovery phase.

3.2 H-mode

The formation of the H-mode consists of the vanishing of the edge turbulence, therefore building an edge transport barrier improving the energy confinement. The energy being computed from the pressure $p = nT$, the pressure profile shows a typical edge barrier. We can see on the figure on the right this barrier, called *pedestal*. Here we only display the density as function of $\rho_V = \sqrt{V/V_{\text{tot}}}$, as it is easier to view the barrier on this profile than on the pressure one. The change in slope between the pedestal and the rest is called the *top of pedestal* or *pedestal shoulder*. The inner region of the plasma is the *core*.

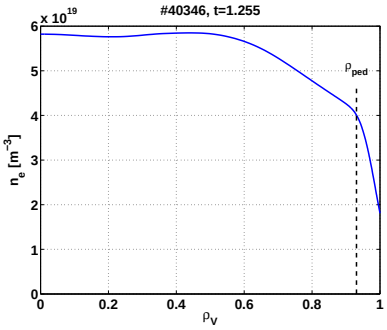

Figure 3.1: H-mode density profile.

This barrier is a great improvement factor as the core density and temperature profiles obey to [17]

$$\frac{R}{L_{n_e}} \simeq \text{cst} \qquad \text{and} \qquad \frac{R}{L_{T_e}} \simeq \text{cst} \tag{3.12}$$

where we have introduced the scale lengths of the temperature and the density defined by

$$\frac{R}{L_{T_e}} = R\frac{\nabla T_e}{T_e} \qquad \frac{R}{L_{n_e}} = R\frac{\nabla n_e}{n_e}$$

We then understand that if we multiply by two the density or the temperature at $\rho_V \simeq 0.9$, not only the core value would be higher but also the core gradient, which helps the center value to increase. Thus the boundary conditions play an important role for the whole plasma.

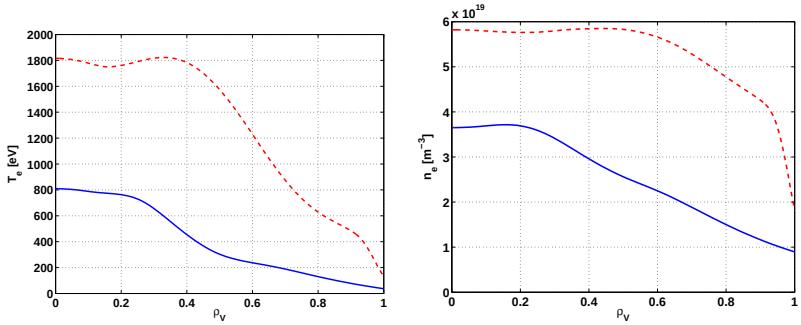

(a) (b)

Figure 3.2: Electron temperature and density comparison between an L- (solid blue, data from TCV #39319 at $t = 0.4s$) and an H-mode (dashed red, data from TCV #40346 at $t = 1.255s$).

The H-mode plasma being formed upon a transport barrier, the properties of the latter have to be studied. For instance, we know from [14] that in electron internal transport barriers (eITB) we have the relation

$$\frac{\nabla n}{n} \simeq 0.5 \, \frac{\nabla T}{T} \tag{3.13}$$

which can be rewritten using the gradient scale length as $L_n \simeq 2L_T$.

It was also found that this approximation is good for type-I ELMy H-mode in ASDEX Upgrade [18]. This could be an interesting result if a similar law can be generalized for H-mode pedestals and therefore needs to be investigated in the present work.

3.2.1 The divertor configuration

The H-mode regime has been discovered when overcoming an input power threshold. The configuration of ASDEX is diverted, and it was later found that the divertor configuration provides an easier access to the H-mode.

The shape of the plasma is controlled by the magnetic fields, created by the currents flowing in the external coils. The configuration is such that there are somewhere points of null poloidal field, called the *X-points*. The magnetic surfaces are all closed, but there are not many closing inside the vessel. The biggest one is the last to close inside and is called the *last closed flux surface* (LCFS) or *separatrix*. In a limiter plasma, the X-points are all outside the vessel and the LCFS is touching the wall.

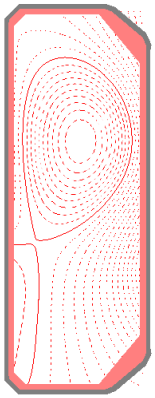

Nearing an X-point towards the LCFS can make a divertor plasma if it enters into the vessel. In this configuration the LCFS is not touching the wall directly but only by the prolongation of its field lines. The usual divertor configuration at TCV is called *single-null (down)* (SN or SND) because it only has one active X-point, below the plasma.

Recalling that ψ is the poloidal magnetic flux, we see on the left the lines at which ψ is constant inside the TCV vessel for the shot #40080 at time $t = 0.8s$. This is a divertor configuration. The solid line is the LCFS. Inside this surface the plasma is confined, whereas plasma outside is not. This latter region is called the *scrape-off layer* (SOL). The point where we figure that the lines of the LCFS are crossing is the X-point where the poloidal magnetic field is null.

Having the X-point so close gives a profile of the safety factor that has a very sharp slope at the edge. Indeed, the safety factor goes like $q \sim B_t/B_p$; we understand that nearing a point

where the poloidal field is null implies that $q \to \infty$. This very sharp slope yields a high value for the magnetic shear too. The reduced edge transport could be due to these observations.

Plasma particles following the field lines, the ones that are on this closed surface in the upper-half can go down and reach there the vessel (as shown on the left). Instabilities expel sometimes particles and energy from the plasma. These particles being still charged, they continue to follow the field lines outside the LCFS. In a limited plasma, they will reach the wall soon anywhere. However, in a divertor plasma, they all go down onto the divertor plates, yielding a large amount of energy on a small surface. This is a major issue for ITER as its reference scenario includes instabilities which may cause destructive erosion of the plasma-facing components.

Varying the currents inside the shaping coils (which change the magnetic topology), we can change the shape of the plasma to get, for instance, *snowflake* configuration (SF) [19,20]. The SN configuration being the most common among the different devices, this work is focused on this configuration, though it would be interesting to study SF configurations as well. Indeed, a recent work reported that in SF H-modes, the confinement is a little higher and the ELM frequency is reduced by a factor two to three to that of SN H-modes [19].

Another recent work about H-mode reports that for SN configurations in TCV, we can apply the relation [12]

$$W_{core} \simeq 3.5 W_{ped} \tag{3.14}$$

The figure on the right has been done using experimental measurements. With the temperature and density profiles, we compute the integrated energy profile. Then we choose a position that we define as $\rho_{\text{core-edge}}$ and we compute the energy on the left (core) and on the right (edge) of this position. Varying this position on the whole profile gives us this graph. As we can see, the ratio is very sensitive to the position and may change significantly for a small change in $\rho_{\text{core-edge}}$ for the considered shot (#40080 at $t = 0.8s$).

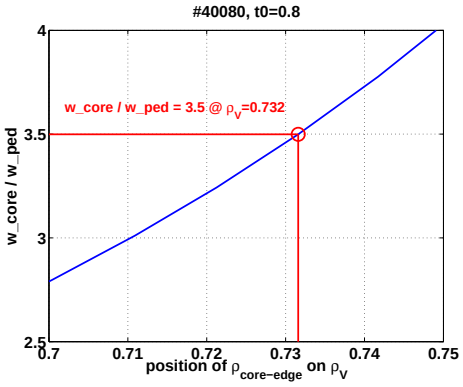

Figure 3.3: Energy in the core compared to that in the pedestal as function of the pedestal position.

Chapter 4

Simulations implementation

The theoretical tool used in this work is the simulation using the transport code ASTRA v. 6.2 (Automated System for TRansport Analysis) [21]. This allows us to use experimental data as input and modify some parameters, even during the run. It solves 1D radial transport of heat and particles using a set of four flux-surface-averaged diffusive equations. It supports also user-defined additional modules such as additional heating. The equilibrium reconstruction is computed using a 2D fixed-boundary 3-moment equilibrium solver which solves the Grad-Shafranov equation.

The sawtooth instability can be added to the simulations with the additional package from E. Fable [22]. However, this model has been observed to give questionable data in our simulations with density evolution and we decided not to enable the sawteeth to keep the accuracy of the data.

The spatial resolution of the output of ASTRA is not very good since its space-step is $\Delta\rho \sim 0.02$ in our version (ASTRA uses $\rho_\Phi = \Phi/\Phi_a$, Φ being the toroidal magnetic flux). However, the input parameters that define the radial grid are bound to some other parameters, making them very difficult to change without losing the simulation consistency. We were not able to get a better resolution for this work.

4.1 Temperature computation

The temperature computation in ASTRA is done with the heat flux. The definition of the heat fluxes implemented in the code have the following form:

$$\frac{625 q_e}{V' G_1 n_e T_e} = -\chi_n^e \frac{1}{n_e}\frac{\partial n_e}{\partial \rho} - \chi_e \frac{1}{T_e}\frac{\partial T_e}{\partial \rho} - \chi_i^e \frac{1}{T_i}\frac{\partial T_i}{\partial \rho} + C_e$$
$$\frac{625 q_i}{V' G_1 n_i T_i} = -\chi_n^i \frac{1}{n_e}\frac{\partial n_e}{\partial \rho} - \chi_e^i \frac{1}{T_e}\frac{\partial T_e}{\partial \rho} - \chi_i \frac{1}{T_i}\frac{\partial T_i}{\partial \rho} + C_i$$

where $G_1 = \langle(\nabla\rho)^2\rangle$ and the χ_j^k are the diffusion coefficients contribution from the other species' temperature or the density to the k species' temperature. As discussed above (§3.1), the off-diagonal terms are negligible, allowing us to set $\chi_i^e, \chi_e^i, \chi_n^i$ and χ_n^e to zero in our simulations, as well as C_e and C_i.

The electron and ion temperatures are computed using fixed boundary conditions, upon which the whole profile is then built. This implies we must provide consistent data to ASTRA, the better being experimental data. The electron temperature and density are measured using

Thomson scattering diagnostic [23]. Using these quantities, a few others and some transport scripts, we can build the profiles for every other quantities. But those scripts do not have a good accuracy for H-mode transport since the pedestal steep gradients are not measured precisely enough for them. We must take our "experimental" data with a great care if we do not want to provide wrong input to our simulations.

In particular, we have to be careful with the ion temperature, as the said scripts cannot compute it right for H-mode. We can take those data directly from the Charge-eXchange Recombination Spectroscopy (CXRS) measurements. This diagnostic measures specifically the ion temperature [24]. Using these data we can have a good ion temperature boundary condition for our simulations.

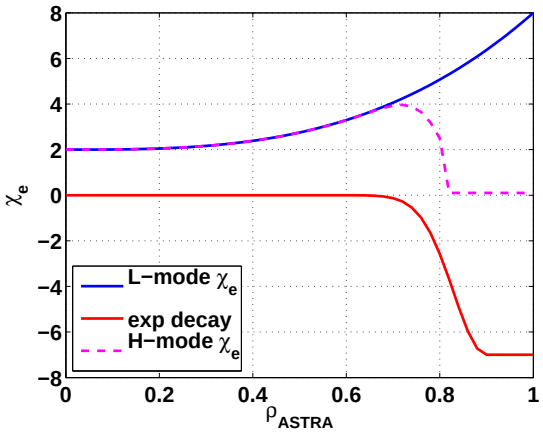

Figure 4.1: Self-made χ_e used for H-mode simulations.

The experimental electron heat diffusivity χ_e is not available, and the computed one is not accurate. Thus we have to use a self-made χ_e in the simulation. To achieve this we use a standard L-mode χ_e, i.e. a parabolic one, that we truncate to create the pedestal.

To build an H-mode χ_e, we look for the good L-mode χ_e without step by running the simulation and changing its profile until the simulated electron temperature presents more or less the same slope as the experimental one, though lower. Then we can truncate this profile to create the pedestal. The temperature pedestal height may be small, but in this work it is important because simulations are implemented such that the density pedestal is computed according to $L_{n_e} \simeq 2L_{T_e}$ (explained in §4.2). Thus to adjust the truncation of χ_e we try to match the pedestal density profile. To prevent singularities, we do not make a step for the truncation but we use an exponential function to make this step a little smoothed.

To have the energy as near as possible to that given by the scaling law (3.8), we use a scaling on χ_e. During the steady-state phase, we multiply the electron thermal diffusivity by the ratio of the instantaneous energy confinement time divided by the scaling one (see appendix B.1). This leads the temperature to what the scaling predicts. To have a little freedom in this procedure, we put a parameter manually modifiable during the simulation, which can be seen as the *HH* factor.

The height of the pedestal of χ_e is scaled using the same principle as the energy scaling. We use the scaling law (3.14) which states that the core energy should be around 3.5 times the pedestal one. We adjust the value of χ_e in the pedestal region where we have truncated it. This scaling is done during the steady-state standard simulation and is disabled for ELMy simulations.

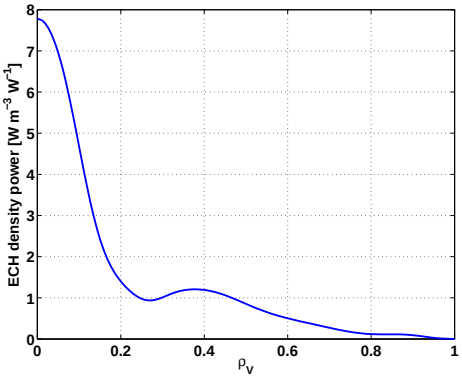

Figure 4.2: ECH power deposition profile.

The ion temperature computation was done using an ASTRA script computing the neoclassical Angioni-Sauter ion heat conductivity [25]. As the experimental data are not very good, we cannot determine if there is a pedestal, though the ion temperature should be equal to the electron temperature for $\rho_\psi = \sqrt{\psi/\psi_a} > 0.85$ in TCV [12]. The ion thermal diffusivity was left unchanged for the H-mode simulation.

The ECH power is computed with the TORAY-GA code [26]. It is then given to the ASTRA

code by the profile of absorption and by the total input power. We thus implement the ECH power as the product of these terms. We must watch this power to stay as it is intended. The total input power is the power integrated over the whole volume. Thus at each time step we renormalize the profile to ensure ourselves that the integrated ECH power remains equal to the experimental injected power.

4.2 Density computation

The density computation is achieved using the same kind of equation as the temperature computation, the particle flux equation. It is implemented as

$$\frac{\Gamma_n - \int_0^\rho \mathrm{d}\rho \left(V' S_e - \frac{\partial V' n_e}{\partial t} \right)}{V' G_1 n_e} = -D_n \frac{1}{n_e}\frac{\partial n_e}{\partial \rho} - \chi_e^n \frac{1}{T_e}\frac{\partial T_e}{\partial \rho} - \chi_i^n \frac{1}{T_i}\frac{\partial T_i}{\partial \rho} + V_n$$

with S_e the particle source. As discussed above (§3.1), the off-diagonal terms are contained in V_n, thus we set $\chi_e^n, \chi_i^n = 0$. We also do not want any particle source, which is set by $S_e = 0$ for the particle number conservation.

However, ELMs expel particles and energy. The energy is carried by the particles onto the divertor plates. Once there, particles can recombine to form neutral atoms again. If neutral, they are free to move wherever in the vessel, therefore can get back into the plasma and be re-ionized. This yields the density increase right after the ELMs.

Recalling of equation (3.4), taking the equilibrium steady-state case means the flux is null and it yields $\nabla n_e/n_e = -V_n/D_n$. We thus have a way to control precisely the density computation through these parameters. It must be noted that the V_n from ASTRA is the opposite of the one we saw in the theory, which yields in ASTRA $\nabla n_e/n_e = V_n/D_n$.

We specify them in such a way that the ratio V_n/D_n is well defined. This is achieved by doing $V_n = aD_n$, so that the ratio is a. The diffusion coefficient being a little more free, and according that $D_n \sim 0.2\chi_e$ in TCV shot with ECH and transport barriers [27], we set $D_n = 0.2\chi_e$.

Recalling of (3.13), we use this scaling linking the density to the temperature for the pedestal region to compute the density. Being unsure about the validity of this scaling, we introduce a free parameter to be able to adjust our profile. The density peaking $n_{e,0}/\langle n_e \rangle$ gives us information about the gradient length for the density. Having a highly peaked profile we understand the gradient length L_n associated is small. The profile peaking values for TCV SN shots may be in the range 1 – 1.4 [12]. This allows us to give ASTRA a value around the unity for the ratio V_n/D_n for the core region.

In summary, once the values of $n_e(\rho = 1)$, $T_e(\rho = 1)$ and $T_i(\rho = 1)$ are given, the profiles are determined by the following assumptions (except if stated otherwise):

- $\chi_e \sim \rho^2$ in the core
- $\tau_E = HH\ \tau_{\mathrm{IPB98}(y,2)}$
- $W_{core} = 3.5\ W_{ped}$ acting on χ_e in the pedestal region
- $D = 0.2\ \chi_e$ in the core
- $\nabla n_e/n_e = 0.5\ \nabla T_e/T_e$ in the pedestal region

4.3 ELM implementation

The ELMs were not triggered in the simulations from MHD instabilities as explained above (§2.2), but done manually. They were achieved by modifying the profile of χ_e, χ_i and D_n radically. Increasing these transport coefficients by many orders of magnitude at the edge, this means the edge transport is very important and therefore the profiles flatten near the edge while keeping the boundary value fixed to the imposed value. This mimics an unstable mode which would be localized near the edge.

The profiles for χ and D_n are shown below. The density diffusivity was raised less because its pedestal has been observed to decrease less in experiments with type-I ELMs [12].

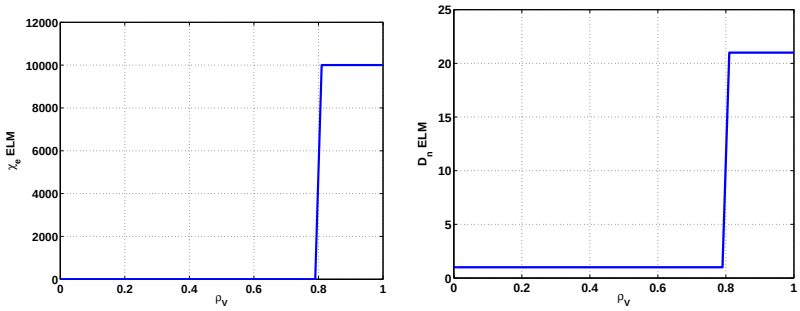

(a) (b)

Figure 4.3: χ and D_n used to create the ELMs.

The ELM "standard parameters" for our simulations are a duration of $100\mu s$ and a frequency of $50Hz$ (experimental data), the changes have a radial interaction range of the temperature pedestal range (approximately $0.78 < \rho_\Phi < 1$), and an amplitude of $10'000\ m^2s^{-1}$ in χ_e and χ_i and of $20\ m^2s^{-1}$ in D_n. This choice was made to have the temperature pedestal fully flattened by the ELM. The density pedestal has been observed to be slower to be destroyed [12]. The choice of the $20\ m^2s^{-1}$ has been made to reproduce this behavior. However, the experiment ELM expelled energy was higher than what we got in our simulations. We tried to increase this value, but the density pedestal flattened much faster than the expelled energy increased. It was thus chosen to let this arbitrary value to keep the desired behavior of the density pedestal during the ELM.

The registered ELM was the eleventh one, but we also saved the first one of the same simulation to compare them together in further analysis. As can be seen on the time trace of the thermal diffusivity fig. 4.4b, we set the simulation time to be at $t = 0$ at the onset of the ELM. Then the ELM stops at $t = 0.1ms$ and the next one starts at $t = 20ms$.

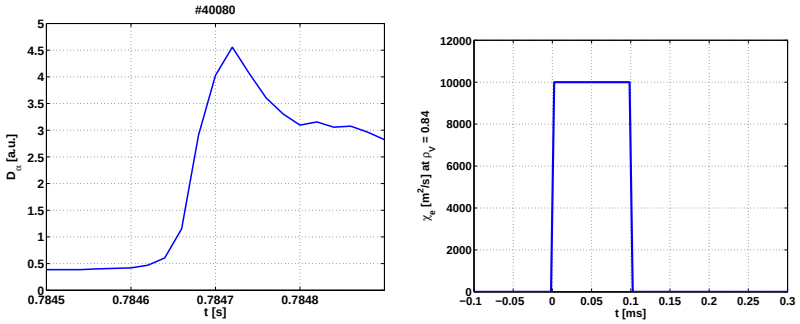

(a) D_α time trace showing the ELM crash.

(b) Time trace of χ_e. χ_i is the same, and D_n is like this one but not as high during the ELM.

Figure 4.4: ELM experimental and simulation time traces.

Chapter 5

ELMy H-mode simulations

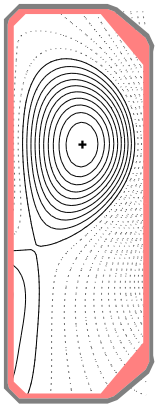

The input data for our simulations were taken from TCV shot #40080 at time $t = 0.8s$. This choice was made upon many characteristics, mainly that it is a divertor ELMy H-mode with constant ECH power input. Another characteristic is that there is available data from the CXRS diagnostic, which is not yet standard in TCV. On the right we have a poloidal section of the plasma flux surfaces (#40080, $t = 0.8s$).

Simulations have been done for several cases. The reference case is using the self-made χ_e scaled for the total and pedestal energy, computing the pedestal density using the $L_n \simeq 2L_T$ scaling except during ELMs. The central density computation uses $V_n/D_n = 1$ to be not too far from the experimental data. This value is well in the range of [1 1.4] discussed above. The ion temperature was taken from experimental CXRS data.

5.1 H-mode simulations

5.1.1 Experimental data vs simulation

Running simulations cannot be performed without a special care of what we are doing. Here we compare the electron temperature and density because of their important role and the assurance that the experimental data are very good. The ion temperature is also presented on fig. 5.1. The dots represent the measured data, while the lines are the fitted profiles with upper and lower error boundaries, and the ASTRA output data.

We note that the simulated electron temperature is pretty good matching the experimental data except in the very center. The pedestal density is also well matching, giving us good confidence in the $L_n \simeq 2L_T$ scaling. We adjusted it to have the best matching achievable, and this gives the relation $L_n \simeq 1.7L_T$, which is $\nabla n_e/n_e \simeq 0.6\ \nabla T_e/T_e$. Although it was adjusted, this scaling seems to give pretty good results. But the core density appears to be overestimated in the simulation, like the center temperature. This may be due to a sawtooth crash right before the measurements were taken, implying the experimental profiles are post-sawtooth ones.

The χ_e used in this simulation had been scaled with regards to the total (3.6) and pedestal energy (3.14). Figure 5.1f shows us that the self-made χ_e was very different from the one in TCV data nodes, whatsoever its profile or its amplitude.

The ion temperature showed on figure 5.1c is not matching the initial condition showed here

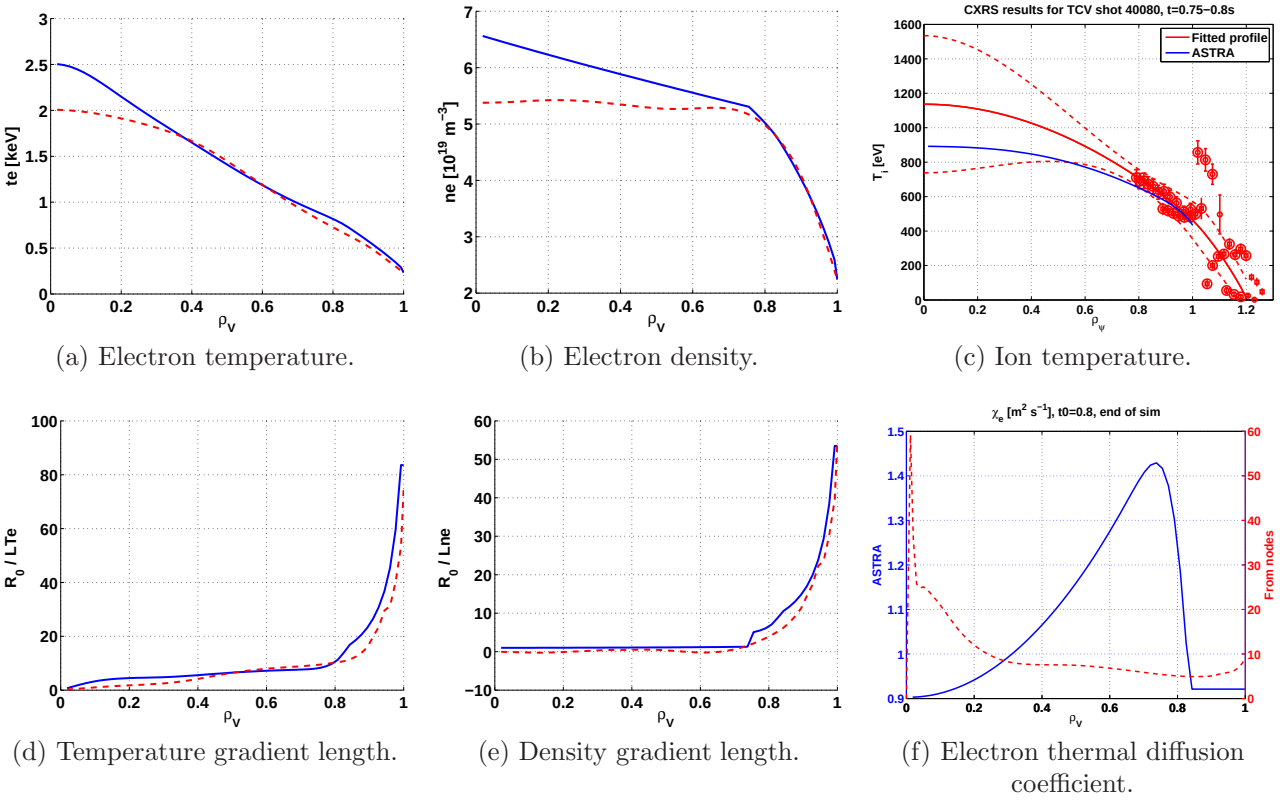

(a) Electron temperature. (b) Electron density. (c) Ion temperature.

(d) Temperature gradient length. (e) Density gradient length. (f) Electron thermal diffusion coefficient.

Figure 5.1: Electron temperature and density with their gradient length, ion temperature and electron thermal diffusivity. The solid blue lines are the simulation output data, while dashed red ones are the experimental data. The ion temperature is presented as function of ρ_ψ. The electron thermal diffusivity dashed line (linked to the right axis) represents the data computed with the L-mode scripts. (Colors in the electronic version.)

as the fitted profile, but is still everywhere in an acceptable range. The boundary condition (at $\rho = 1$) is well in the experimental data.

5.1.2 Effect of edge EC Heating

We have altered the ECH profile such that we have only ECH power deposited in the center, but the volume integrated power is the same. We keep the same χ_e to ease the comparison of the data. The altered ECH profile is shown in fig. 5.2d together with the standard case. The energy confinement time being better in the center, it is normal to observe a higher temperature in the center when it is more heated, as we can see in fig. 5.2a. The edge is heated the same, but in this case the heating comes more from the transport. The center density provides high transport of energy through the species, yielding the higher ion temperature shown on fig. 5.2b.

The electron heat flux (fig. 5.2f) shows a clear difference in the core plasma. The pedestal is also affected by this change, but the difference becomes smaller compared to that of the core and both profiles are essentially the same in this edge region. The figure 5.2e shows the pressure gradient to view the position of the maximum, which is the same in both cases.

The ELM cycle will be studied in the next section. Since the changes in the pedestal pressure are not significant, we will shift the time traces to match the initial values of the reference case, in order to facilitate the comparison between these two cases.

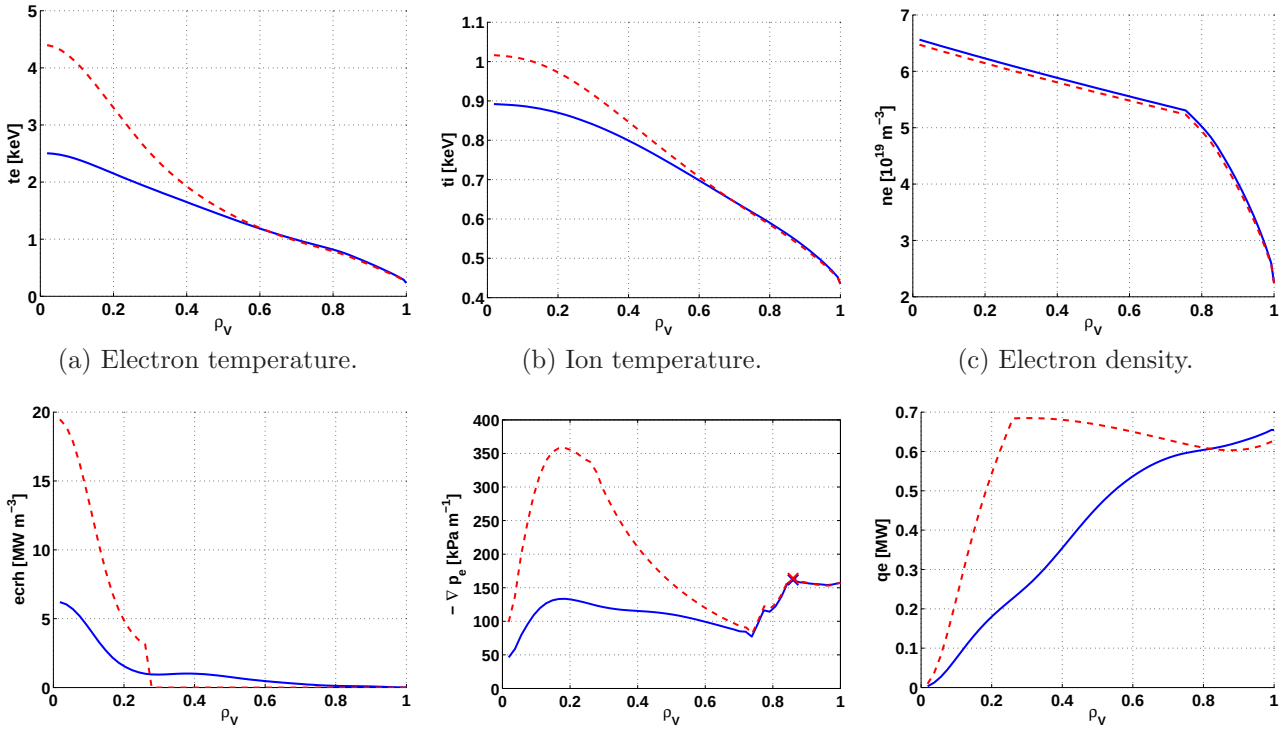

(a) Electron temperature. (b) Ion temperature. (c) Electron density.

(d) ECH deposition profile. (e) Pressure gradient. (f) Electron heat flux.

Figure 5.2: The electron temperature, density and heat flux, the ion temperature, the pressure gradient and the ECH deposition profiles are shown here to compare the central ECH case to the reference one. The latter is represented by the solid blue line while the dashed red shows the former.

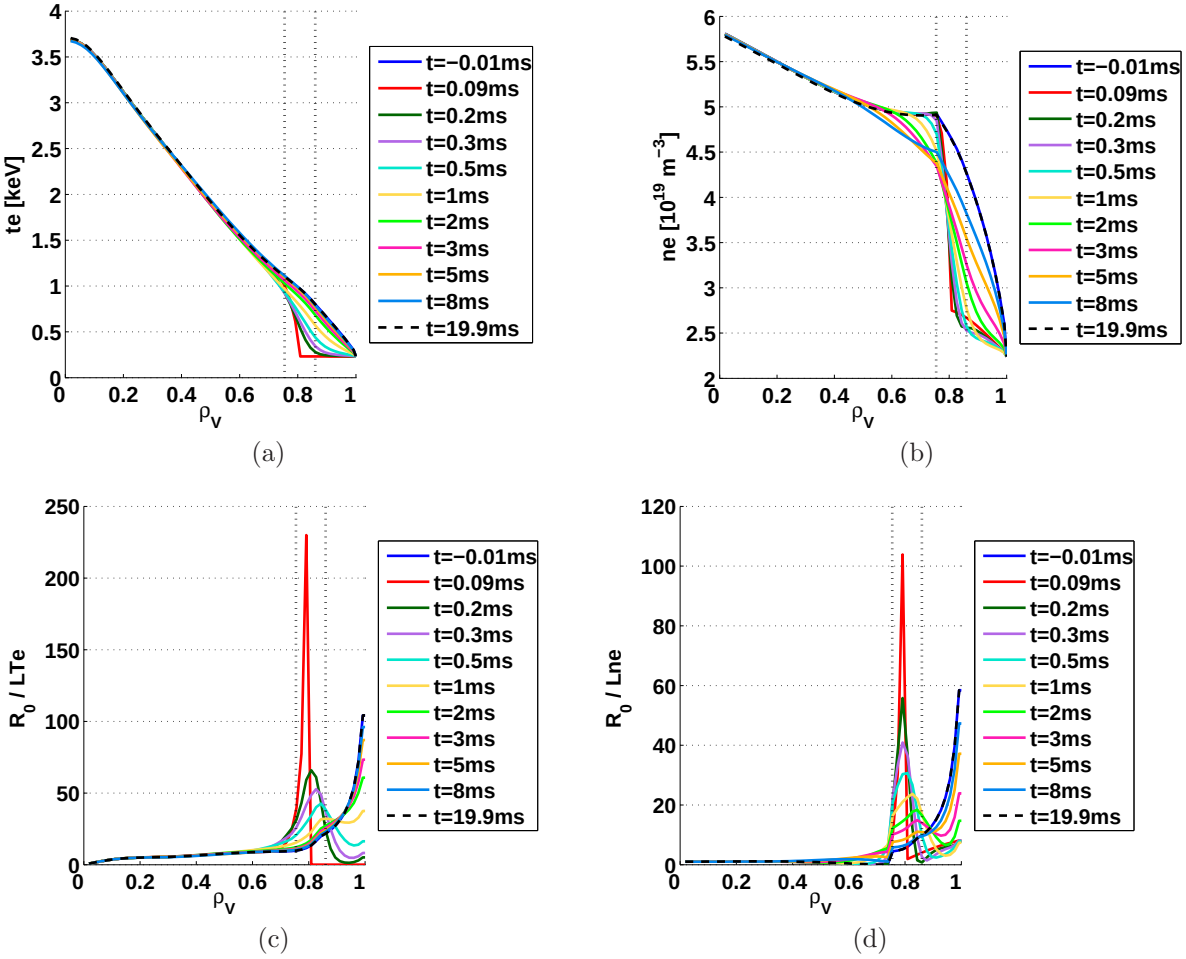

Figure 5.3: Profiles of the main quantities with the chosen values of ρ_V. The vertical dotted lines are the position which will be studied in the time traces.

5.2 ELMs simulations

5.2.1 Simulated ELM cycle

The figure 5.3 displays a chosen set of profiles during an ELM cycle together with the chosen values of ρ_V (vertical dotted lines) that will be used to investigate the time traces of the quantities. The left one is the top of the density pedestal, and the other one is at the maximum of the pressure gradient in the equilibrium case. They will respectively be denoted ρ_1 and ρ_2. The latter happens to be also the surface of $q = 2$. The times are defined according to what we said before (§4.3), $t = 0$ is the ELM onset, the ELM has a duration of $0.1ms$ and a period of $20ms$.

First looking at the temperature on figure 5.3a, we note that it recovers pretty fast. The first time is similar to the last one right before the next ELM. The third is $100\mu s$ after the ELM end and shows that the temperature pedestal has already begun to rebuild itself. But this little start does not give yet $1/L_{T_e}$ pedestal values as high as pre-crash (fig 5.3c). The pedestal density being computed from it (fig. 5.3b), we understand that it is not sufficient for the pedestal density to grow. On the density graph we even observe that the density continues to decrease in the pedestal for more than a half millisecond after the ELM stops. We also note that the temperature characteristic length has higher values at the edge of the ELM until $1ms$ after the ELM. This leads to the same remark for the $1/L_{n_e}$ profile which uses the latter,

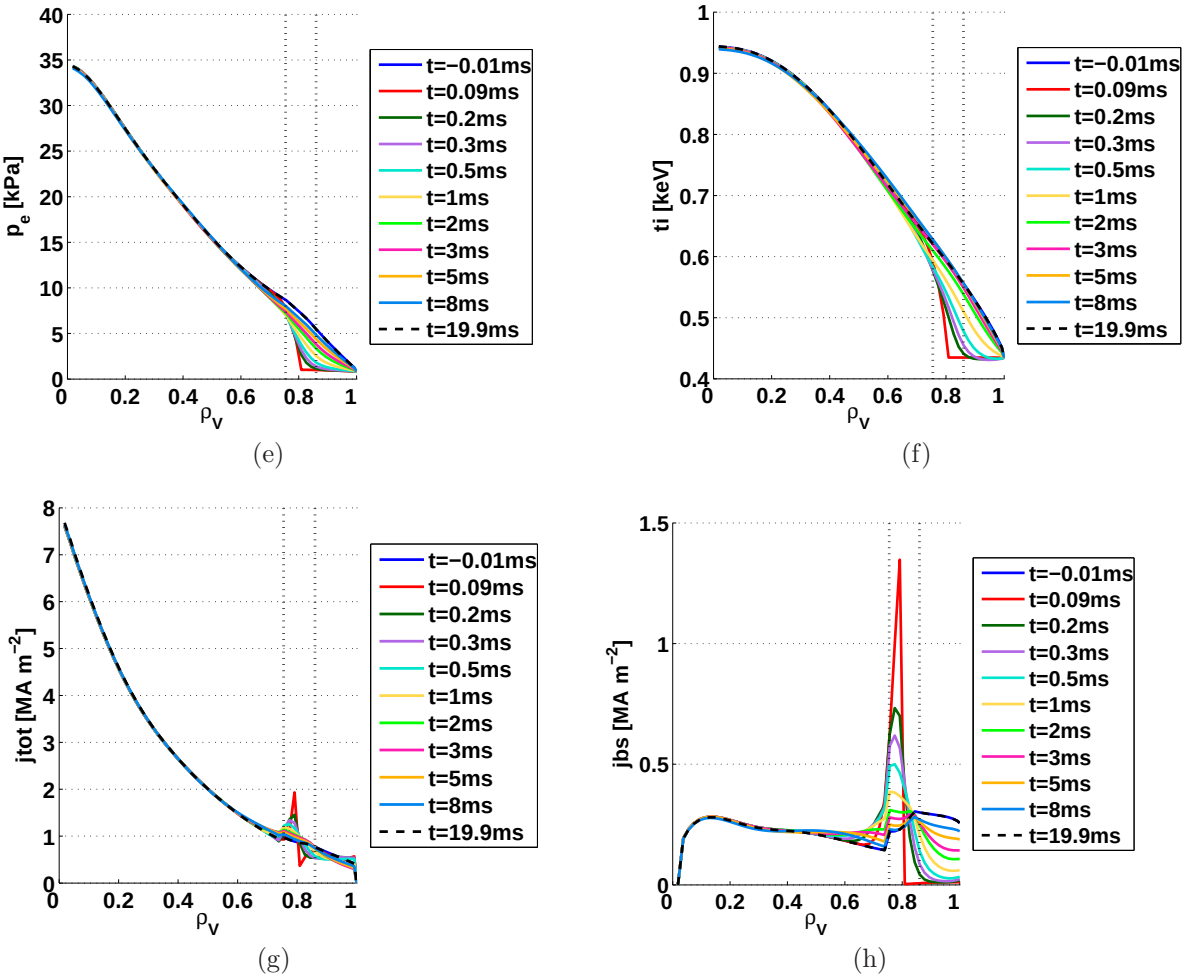

Figure 5.3: Profiles of the main quantities with the chosen values of ρ_V. The vertical dotted lines are the position which will be studied in the time traces.

implying a soft slope for the edge density for a longer time.

Looking closely at the density profiles, we note that at the top of pedestal we also see this phenomenon. This is due to the computation of the density. The ELM makes an almost flat density profile at the edge and a very sharp gradient to match the almost unaffected core density profile. Once the ELM is gone, the normal parameters are applied again and our model tries to make $\nabla n_e/n_e = V_n/D_n$. The inner part has a very low value (see fig. 5.3d) and therefore tries to reduce the gradient. The pedestal part depends on the $\nabla T_e/T_e$ ratio, which is pretty high at this location right after the crash. Thus we understand that our model tries to flatten the inner density profile while it sharpens the pedestal one.

We used the relation $V_n/D_n \simeq 0.6\ \nabla T_e/T_e$ and we have approximately in the pedestal $L_T \simeq 1.7 L_n$ on figures 5.3c and d.

Comparing the electron temperature to the ion one on figure 5.3f, we note that the latter does not rebuild its pedestal as fast as that of the electron. This is due to the fact that our boundary value for the ion temperature is higher than that of the electrons. Hence when the pedestal flattens for these quantities to the boundary value, the ion temperature becomes higher than the electron one, reversing the sign of the equipartition term. The latter yields a sink for the ions and a source for the electrons. This explains the small decrease observed on the pedestal ion temperature right after the ELM.

Assuming that we have never $T_i > T_e$ in TCV, this reversal of the equipartition is not ex-

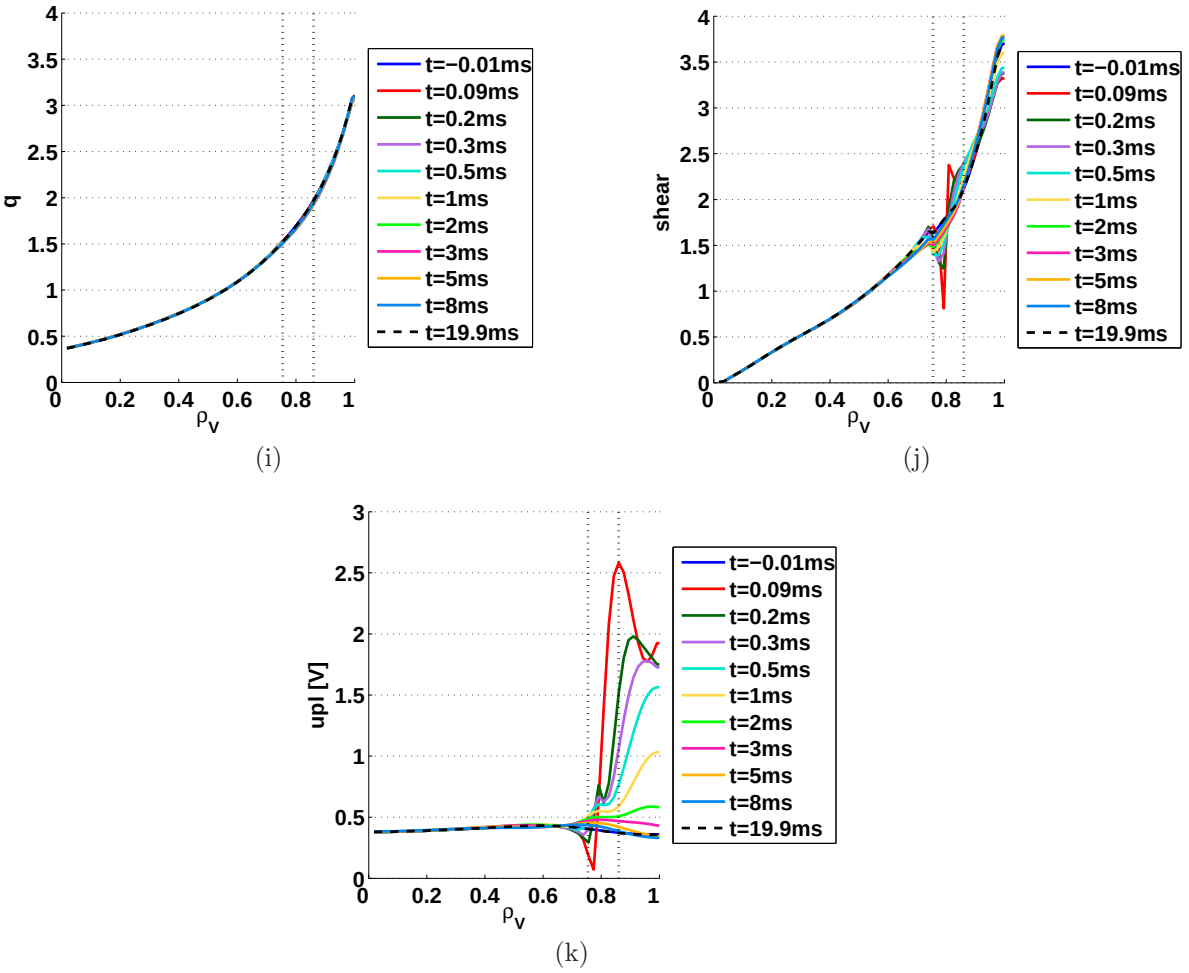

Figure 5.3: Profiles of the main quantities with the chosen values of ρ_V. The vertical dotted lines are the position which will be studied in the time traces.

pected. To prevent this, the ion temperature could be implemented in another way. [12] reported that in TCV SN H-mode, we have $T_i \simeq T_e$ for $\rho_\psi > 0.85$. It could be interesting to study a case with both boundary temperatures equal $T_{i,a} = T_{e,a}$ and building an ion temperature pedestal on χ_i.

Considering the total and bootstrap current density (figs. 5.3g and h), and the loop voltage (5.3k), we note that the recovery is pretty fast. For the loop voltage and the total current, around $2ms$ after the crash we have almost completely recovered. The bootstrap current is a little longer because it needs the pressure gradient which depends upon both the temperature and the density. The latter is somehow slower to rebuild its pedestal and therefore slows down the bootstrap recovery.

The safety factor profile (figure 5.3i) is almost constant in time. On the contrary, the magnetic shear (fig. 5.3j) shows a clear crash and a recovery time of the same order of the total current density. This means that the flux surfaces are almost unaffected by the ELM according to our model, but the magnetic shear is much more perturbed.

Computing the energy difference, we obtain the proportion of the energy expelled by the ELM. In this reference case, we have $\Delta W/W \simeq 12\%$, which is reasonable for type-I ELMs [12], but a little far from the experimental results ($\sim 20\%$). The absolute loss of energy is around $1.8kJ$.

What can be noted about these profiles is an interesting result in the electron temperature

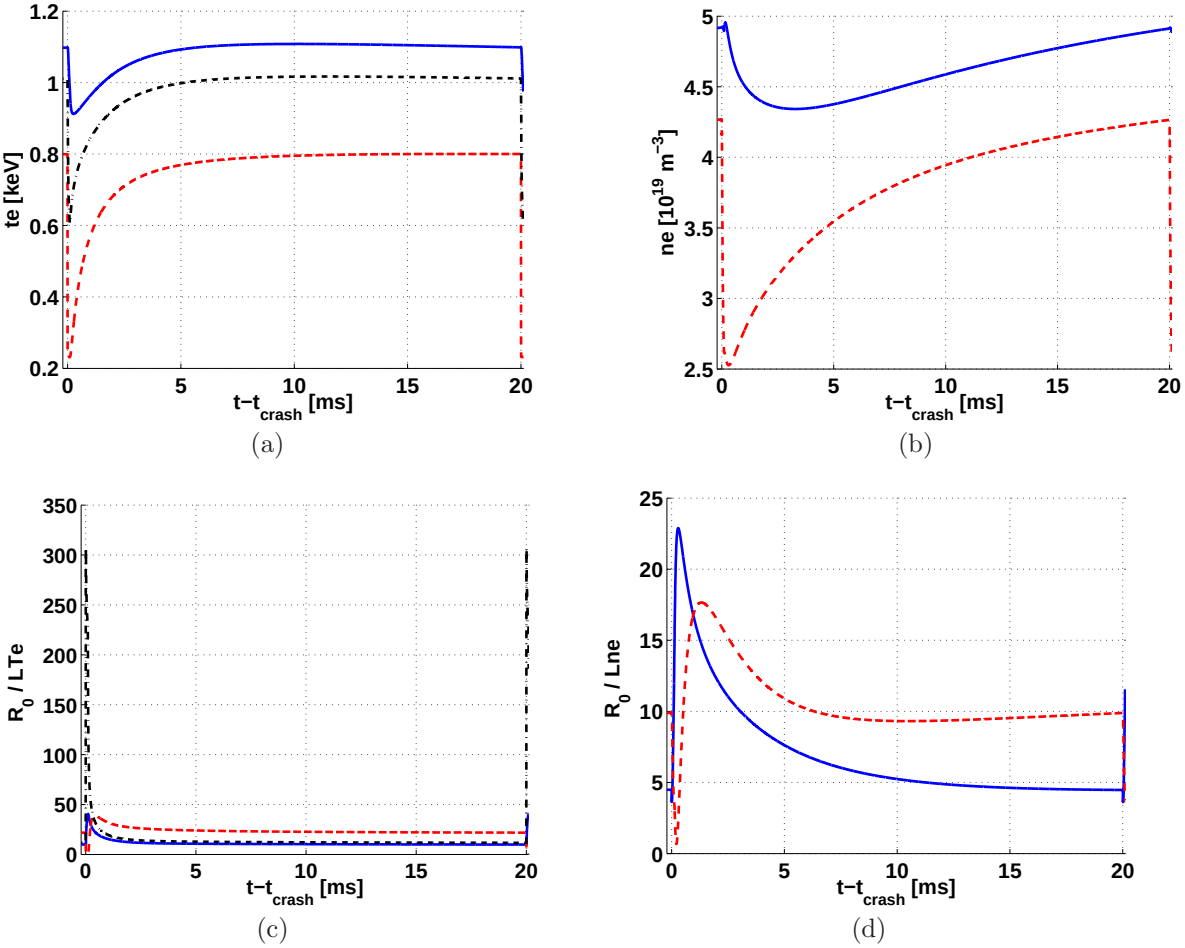

Figure 5.4: Standard simulated ELM cycle. The solid blue one is at the top of the density pedestal and the dashed red one is at the maximum of ∇p from equilibrium. Exceptionally shown is the temperature time trace at its top of pedestal on the temperature and temperature gradient length time traces in dash-dotted black.

and density (figs. 5.3a and b). The crash lets the center values almost unaffected. Nevertheless, [12] reported that the ELMs significantly affect the center temperature almost instantaneously. This could lead us to some global confinement phenomena that might happen during the ELM. Another explanation could be with the strong gradient observed on these figures. The ballooning-kink stability criteria are related to the pressure gradient. At the ELM onset, both profiles reveal sharp slopes at the border between the ELM affected zone and the unaffected core. It is thus possible that these gradients then active another "ELM" there, and this phenomenon could repeat until it reaches the center. A last explanation we can provide here is that the MHD mode itself could be global.

Now we have studied the whole profiles, we can investigate the time traces at the selected locations. The temperature (fig. 5.4a) shows different behavior whether we are looking at the edge of the pedestal or at where we find the maximum pressure gradient in equilibrium. The latter exhibits a shorter characteristic recovery time (about half). However, the former might not show a local confinement time as the global effects can rapidly acts at this position in the temperature core.

The temperature drop at the top of its pedestal is of the order of $0.6keV$. Experiments reveal that this drop should be around $0.2keV$ (fig. 6.3 in [12]), thus it is too high in our simulations.

These time traces exhibit a very fast recovery for the temperature after the crash, which is

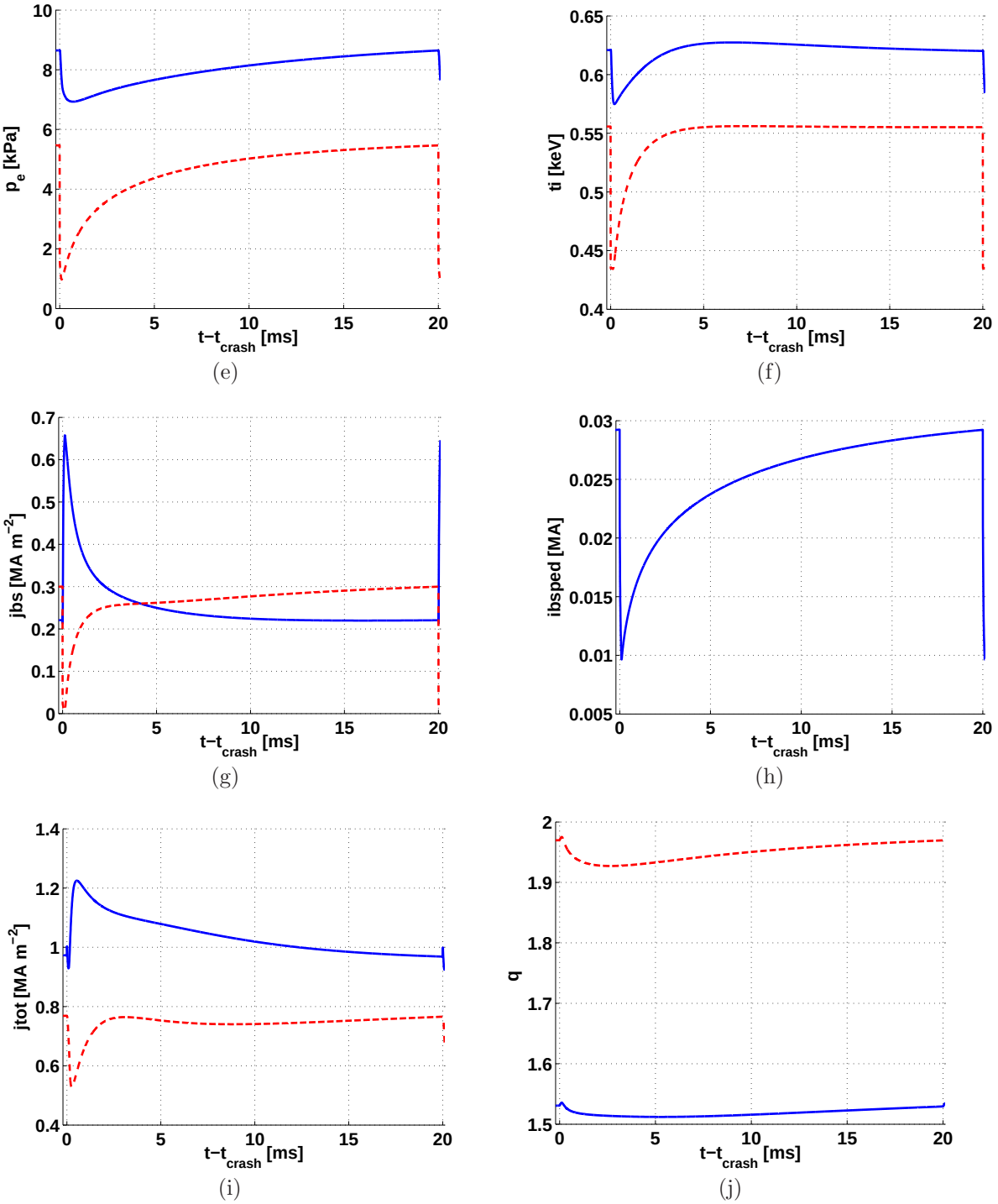

Figure 5.4: Standard simulated ELM cycle. The quantity "ibsped" is the bootstrap current density integrated over the pedestal. The solid blue one is at the top of the density pedestal and the dashed red one is at the maximum of ∇p from equilibrium.

the observed behavior for type-I ELMs at TCV [12]. Though, the experimental data show a recovery to the steady-state value less than our simulations ($\sim 300\mu s$ from fig. 6.3 in [12] instead of $\sim 3ms$ which corresponds to 90% of recovery in fig. 5.4a in the present work). To meet the experimental data, the heat conductivity in the ELM phase may be too much increased in the pedestal (or the pedestal duration may be too long) while in the post-ELM phase it might not be large enough, also in the core region.

Considering the density (fig. 5.4b), we note that at the top of pedestal, we see the small

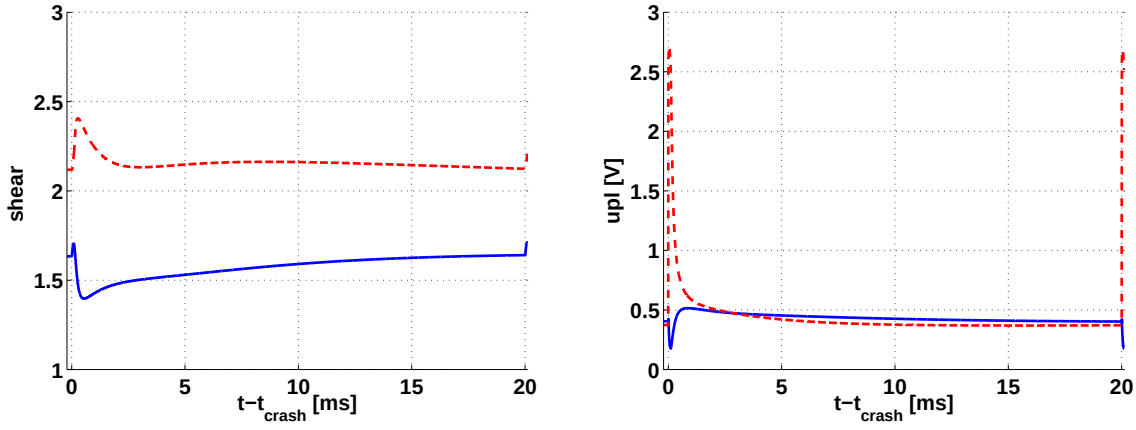

(k) (l)

Figure 5.4: Standard simulated ELM cycle. The solid blue one is at the top of the density pedestal and the dashed red one is at the maximum of ∇p from equilibrium.

relaxation we discussed above and will not be discussed here. In the inner part, we see a larger drop, but it occurs *after* the crash. The latter causes only the tiny change we see on the very left of the graph. The following drop is caused by the energy loss, the plasma tries to refill its pedestal after the ELM. Thus here we cannot speak of a recovery time.

Comparing with experimental results from [12] figure 6.4, we note that our pedestal density drop at its top is about $0.6 \cdot 10^{19} m^{-3}$, a little less than what was experimentally observed ($\sim 1 \cdot 10^{19} m^{-3}$). We also have a longer recovery time ($\sim 10ms$) whereas observations of experiments reveal a very fast recovery ($\sim 1ms$) for the density pedestal [12]. On the other hand, comparison between the temperature and the density shows that the temperature is faster to recover than the density, as is the case in the experimental results.

The temperature (fig. 5.4a), the density (b) and the pressure (e) time traces reveal that the pressure recovery is more similar to that of the density than that of the temperature and is therefore dominated by the density, in agreement with the experimental observation [12] figure 6.5. The pressure gradient depends strongly on the density gradient, which we have seen is slower to rebuild than the temperature gradient.

Looking closely at the total current density (fig. 5.4i), the solid time trace goes down and right after up. This phenomenon happening during the ELM, it will not be discussed here as it is beyond the scope of this work.

We also note that there is a change at about $4ms$ on the time trace of the total current (fig. 5.4i) and of the magnetic shear (fig. 5.4k) at the maximum pressure gradient. This is due to the pedestal building. Indeed, the ELM flattens both temperature and density pedestals. When the relaxation begins, the plasma wants to recover it, implying a sharp increase in the temperature and density gradients. When they come to the desired profile, the gradients decrease. But they decrease too much and have to increase a little again. This strongly affects the pressure.

The $j - \alpha$ diagram (fig. 5.5) gives information about the MHD instabilities we spoke earlier (§2.2). Here the cycle is pretty fast to recover its equilibrium state. It is almost finished after only $1ms$. It means that the instability criteria defined in the theory preamble could not, within the model of ELM we used, trigger these instabilities. Though, we discussed of the possibility that the ELM affects the whole plasma. In such a case, the trajectory of $j - \alpha$ may be different and thus could be changing in the last phase before the next ELM.

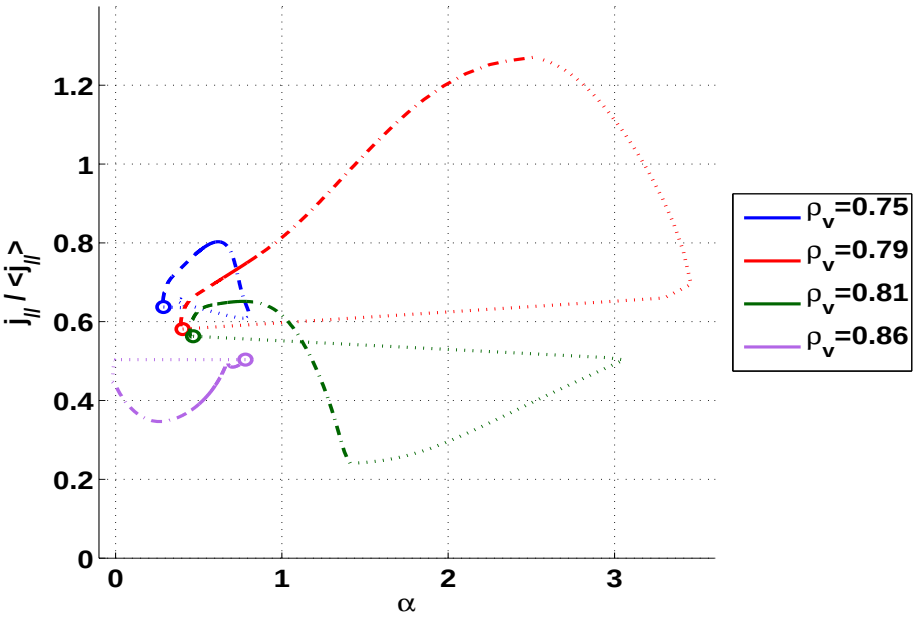

Figure 5.5: $j - \alpha$ diagram for the reference ELM cycle. Dotted lines are during the ELM crash $0 \leq t < 0.1$, dash-dotted is for $0.1 \leq t < 0.5$, solid lines are $0.5 \leq t < 1$ and dashed lines are from 1 to the next ELM (20) with the time in ms. $\rho_V = 0.75$ is the top of the density pedestal, $\rho_V = 0.79$ is where this diagram is the largest, $\rho_V = 0.81$ is the top of the temperature pedestal and $\rho_V = 0.86$ is the maximum of the pressure gradient.

5.2.2 Edge EC heating replaced by central

We are interested in the way the edge EC heating modifies the dynamic behavior of the plasma. As discussed about the equilibrium profiles, this case presents higher center temperatures. Except for this difference, the profiles are almost similar to that of the reference case and are therefore in appendix C.1.

The time traces at the top of the density pedestal show no significant changes from the reference case (shown in appendix C.1, p. 59). We note that they almost all start with a different value, but the slopes are quite the same and the characteristic times do not really vary.

At the maximum pressure gradient, we are interested in the recovery of the pressure gradient. Figure 5.6b shows that the pressure is a little lower in this case as we already saw it. We note that both drop down to the same value and start to recover with the same slope. However, while increasing, the slope of the considered case seems to decrease, yielding no significant improvement in the pressure gradient recovery. If we look at the latter (fig. 5.6d), we find that it has gotten back at 90% of its previous value approximately at the same time as the reference case. The first recovery phase of the pressure gradient lasts about $1.5ms$ as is clearly shown for both cases. This is in good agreement with experimental observations (fig. 6.5 in [12]).

Other quantities exhibit neither significant modification compared to our reference case.

Looking at the $j-\alpha$ diagram (fig. 5.7), we note no significant change in the aspect compared to the reference case (fig. 5.5). The one from this case seems a little shifted downwards. This is because the center current density is higher, due to the higher central temperature, which decreases the normalized edge current density.

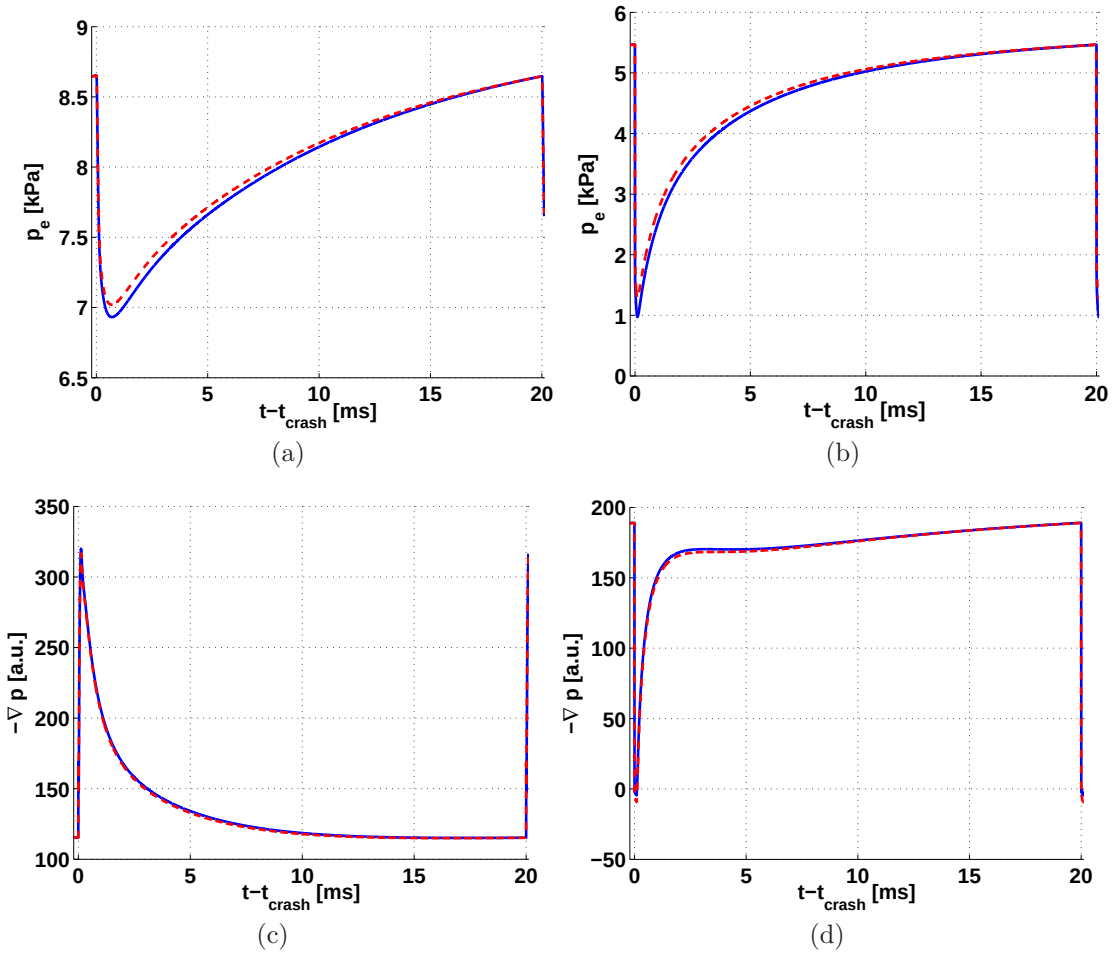

Figure 5.6: Comparison between experimental profile and only central ECH. The solid blue line is the standard case, the dashed red one is the central ECH one. The left figures show the traces at the top of the density pedestal while the right ones are at the maximum of the pressure gradient.

5.2.3 Varying D_n

When varying the particle diffusion coefficient, we therefore change the dynamical behavior of the particles. Recalling of the definition of the diffusion time (3.10), it will have a strong effect on it and therefore slow down or speed up the density processes. The cases considered here are "Dn01", "Dn05" and "Dn10" where we have respectively divided by ten, by two and multiplied by ten the particle diffusion coefficient in the inter-ELM period, and the pinch velocity as well to keep the same ratio V_n/D_n. The equilibrium profiles being unchanged, the profiles of these case do not exhibit a lot of difference comparing to the reference case. We are only showing here the density profiles for the "Dn01" case, the other profiles and cases' profiles being in appendix C.2 (p. 65).

The density profile (fig. 5.8) shows that the density pedestal has been much more flattened among the ELMs than the reference case (fig. 5.3b), and the central density has increased compared to the latter.

The time traces (fig. 5.9), particularly the density time traces, exhibit a clear difference when varying D_n. We understand that lower diffusivity yields a slower behavior for the density. This has an impact on the other quantities too since they depend on the density. For the lowest particle diffusivity ("Dn01"), we observe that this case has a decreasing temperature at the end of the cycle, before the next crash. This might be due to the slow recovery of

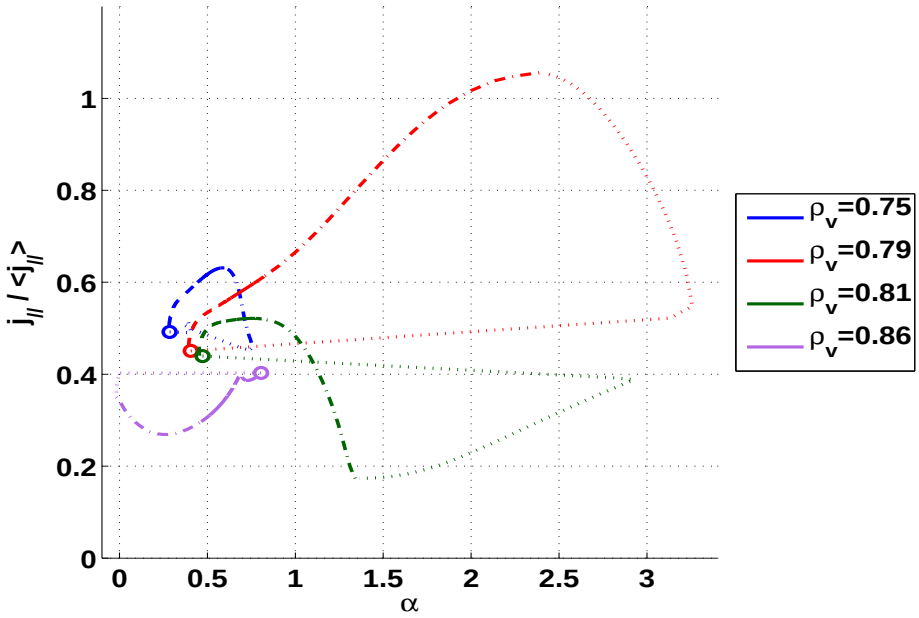

Figure 5.7: $j - \alpha$ diagram for the ELM cycle with only central EC heating. Dotted lines are during the ELM crash $0 \leq t < 0.1$, dash-dotted is for $0.1 \leq t < 0.5$, solid lines are $0.5 \leq t < 1$ and dashed lines are from 1 to the next ELM (20) with the time in ms. $\rho_V = 0.75$ is the top of the density pedestal, $\rho_V = 0.79$ is where this diagram is the largest, $\rho_V = 0.81$ is the top of the temperature pedestal and $\rho_V = 0.86$ is the maximum of the pressure gradient.

the density: the crash decreased the temperature and the density, the former rebuilding right after, faster than the latter. This means that the heating is well spread among the plasma very fast compared to the change in density, having a near-equilibrium temperature profile. But the density continues to regrow and soon the heating losses become more important than the source and the temperature decreases. The ion temperature is also affected by this change since the source of ion heating is the equipartition depending on the collisionality and on the electron temperature. We observe this for all but the high-diffusivity case after around $10ms$.

These changes are less visible at the maximum of the pressure gradient, because here the temperatures are also flattened by the crash.

Looking at the total current density and the shear time traces (figs. 5.9m, n, r and s), we note that at about $5ms$ we seem to have a change in the behavior of these quantities. In the other cases this change is also present but comes faster and has already been discussed. This

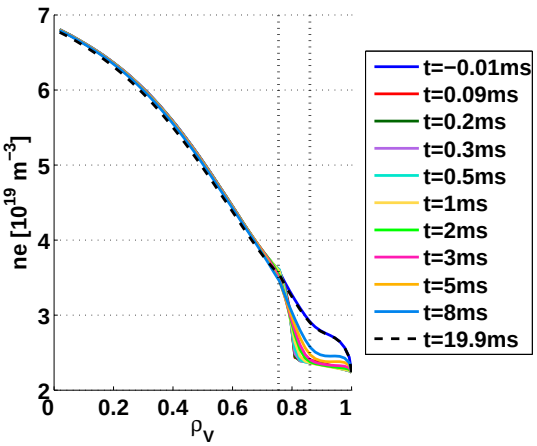

Figure 5.8: Profiles of the main quantities for an inter-ELM with particle diffusivity divided by ten.

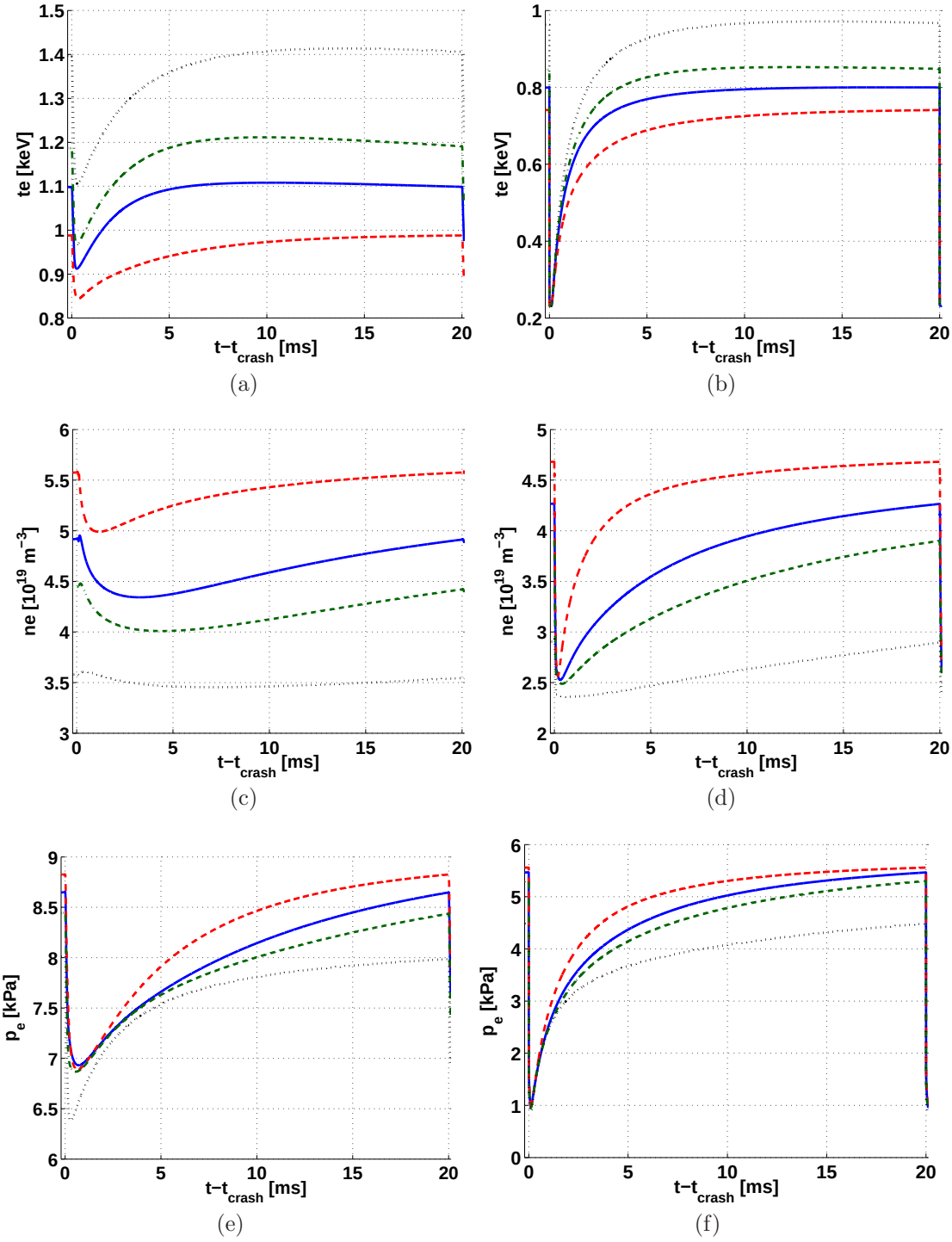

Figure 5.9: Comparison between different values for Dn. The solid blue line is the reference case, the dashed red one is the "Dn10" case, the dash-dotted dark green is "Dn05" and the dotted black is "Dn01". The left figures show the traces at the top of the density pedestal while the right ones are at the maximum of the pressure gradient.

is particularly visible at the maximum of the pressure gradient.

Increasing the density recovery time means it would not necessarily have finished to recover when the next ELM comes. We understand that stopping the recovery earlier will prevent the density to recover as much as it was pre-crash, yielding a gradual decrease.

The energy loss for the tenth-diffusivity case is not quite the same as the reference case.

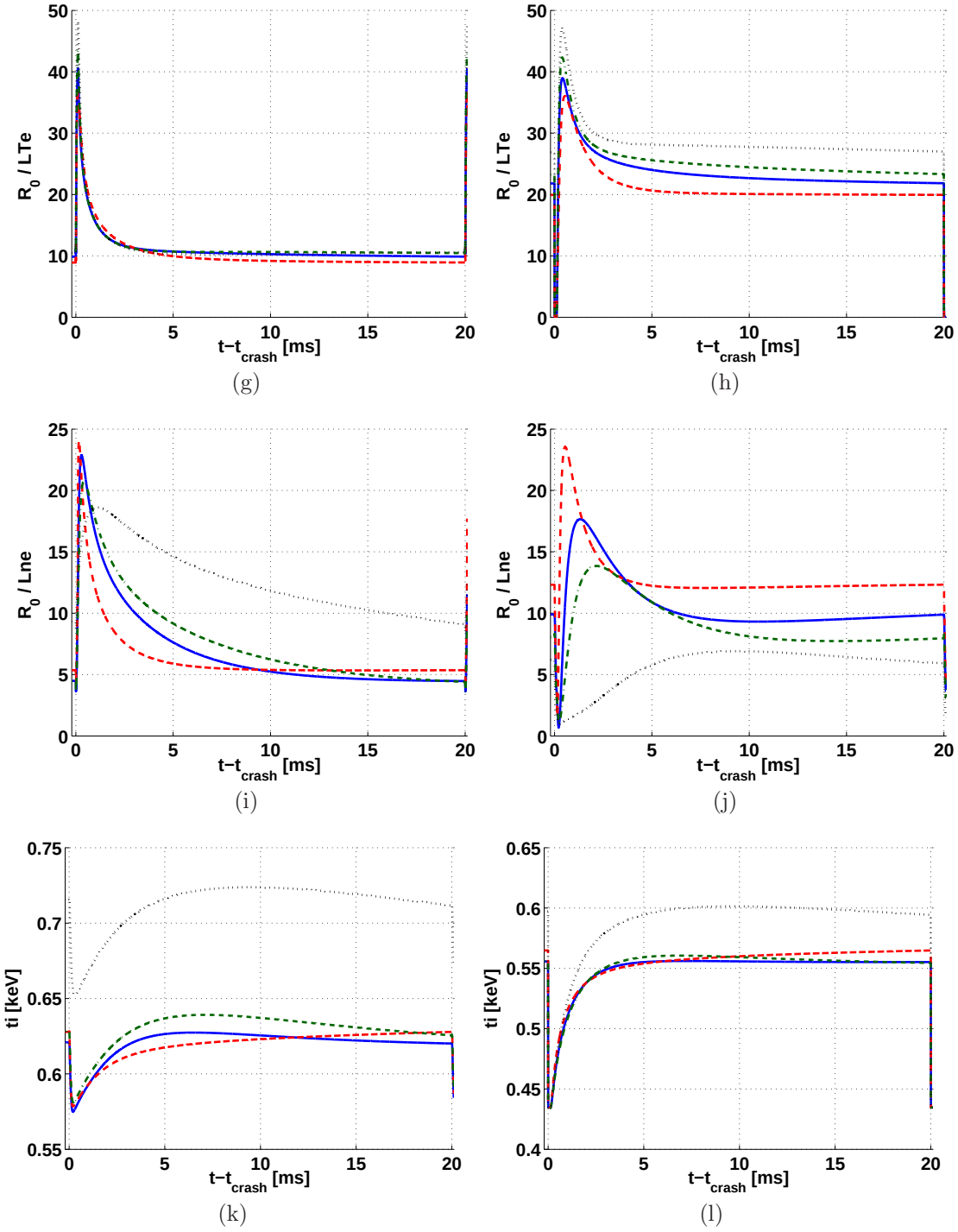

Figure 5.9: Comparison between different values for Dn. The solid blue line is the reference case, the dashed red one is the "Dn10" case, the dash-dotted dark green is "Dn05" and the dotted black is "Dn01". The left figures show the traces at the top of the density pedestal while the right ones are at the maximum of the pressure gradient.

Indeed, it has decreased to 9% (approximately $1.5kJ$). This is explained by the increase of the temperature that compensate the loss of density from the energy point of view. The total energy is almost the same, but the density has been considerably decreased at the considered ELM. Our ELM model is set to not flatten completely the density pedestal. Since the latter did not fully recover, it is already a bit flat, hence the ELM cannot decrease it much.

The $j - \alpha$ diagram for the tenth-diffusivity case (fig. 5.10) seems a little changed compared

to (fig. 5.5). We note that the pressure gradient seems lower, due to the progressive flattening of the density pedestal, but we also note that the cycles seems more compact. This is due to the density recovery time that has been multiplied by ten. The pressure gradient and the edge current density are also affected by this change, particularly visible in the fourth phase (dashed lines).

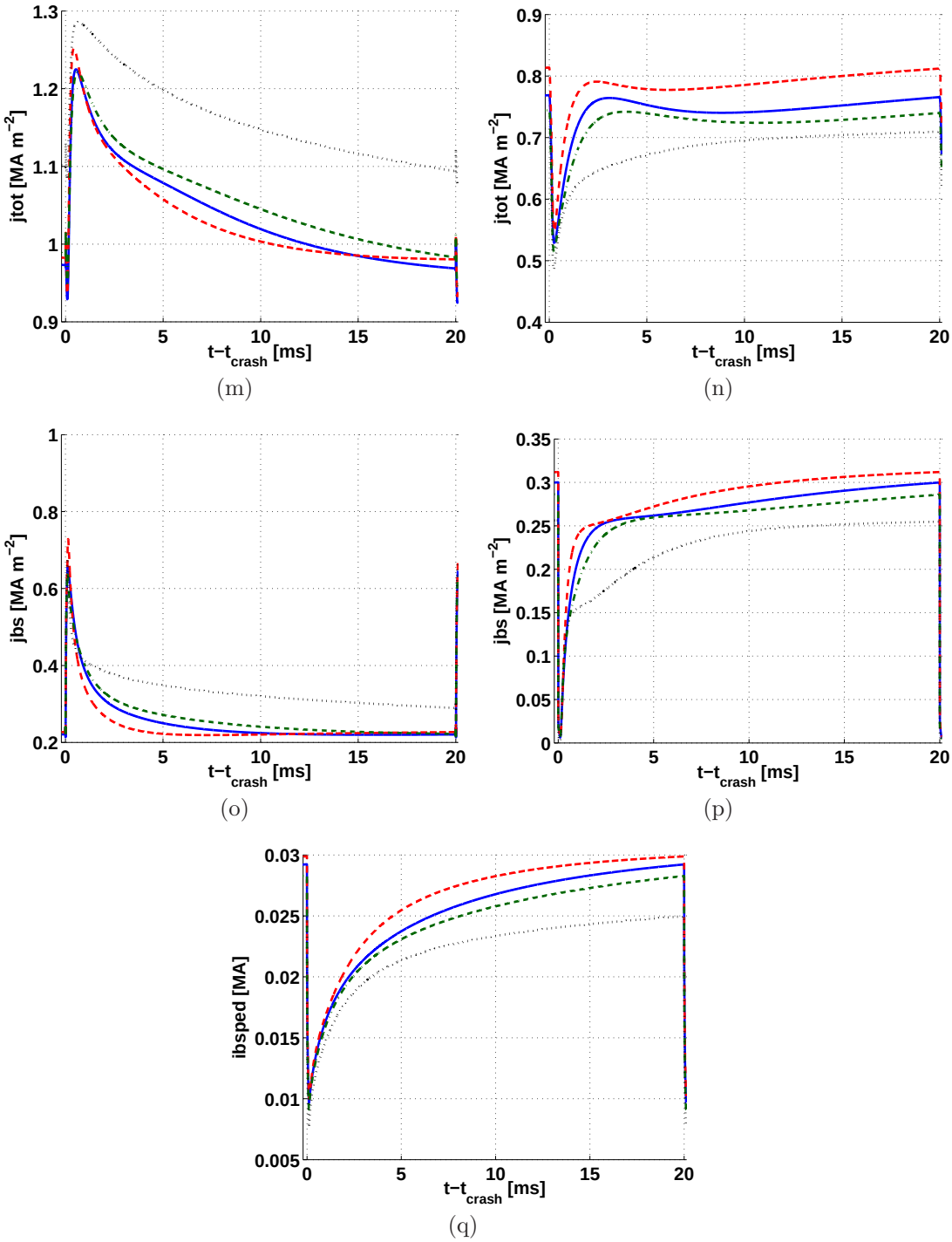

Figure 5.9: Comparison between different values for Dn. The solid blue line is the reference case, the dashed red one is the "Dn10" case, the dash-dotted dark green is "Dn05" and the dotted black is "Dn01". The left figures show the traces at the top of the density pedestal while the right ones are at the maximum of the pressure gradient.

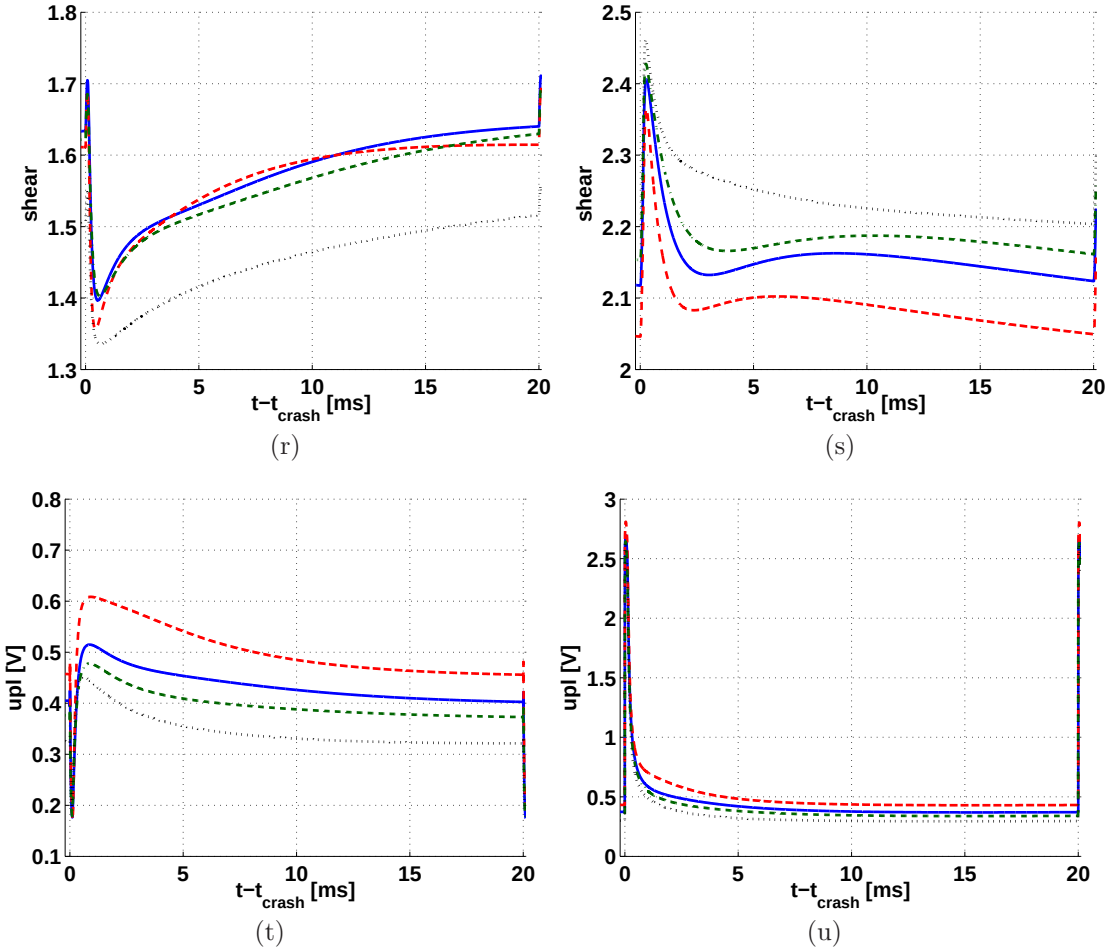

Figure 5.9: Comparison between different values for Dn. The solid blue line is the reference case, the dashed red one is the "Dn10" case, the dash-dotted dark green is "Dn05" and the dotted black is "Dn01". The left figures show the traces at the top of the density pedestal while the right ones are at the maximum of the pressure gradient.

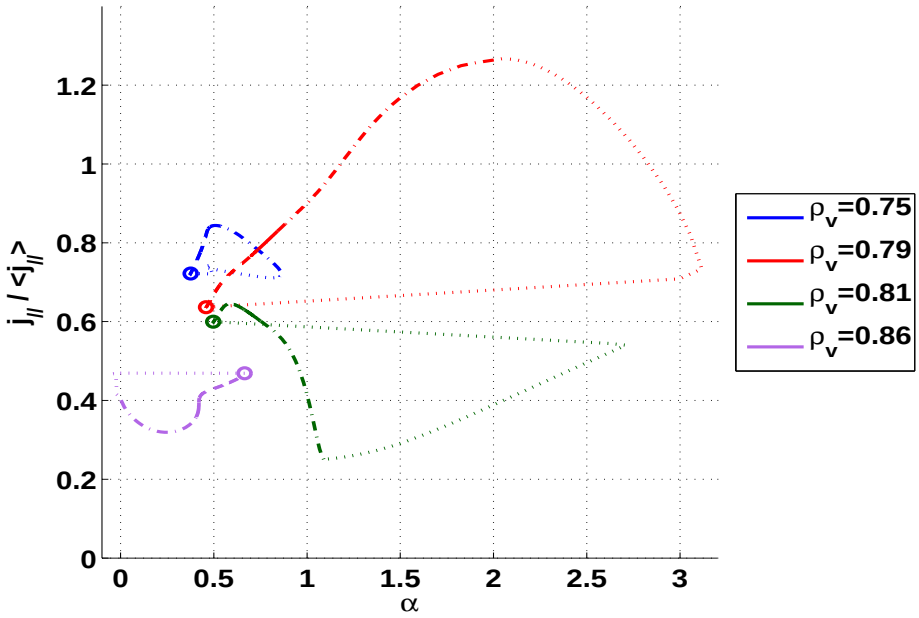

Figure 5.10: $j-\alpha$ diagram for the ELM cycle of "Dn01". Dotted lines are during the ELM crash $0 \leq t < 0.1$, dash-dotted is for $0.1 \leq t < 0.5$, solid lines are $0.5 \leq t < 1$ and dashed lines are from 1 to the next ELM (20) with the t in ms. $\rho_V = 0.75$ is the top of the density pedestal, $\rho_V = 0.79$ is where this diagram is the largest, $\rho_V = 0.81$ is the top of the temperature pedestal and $\rho_V = 0.86$ is the maximum of the pressure gradient.

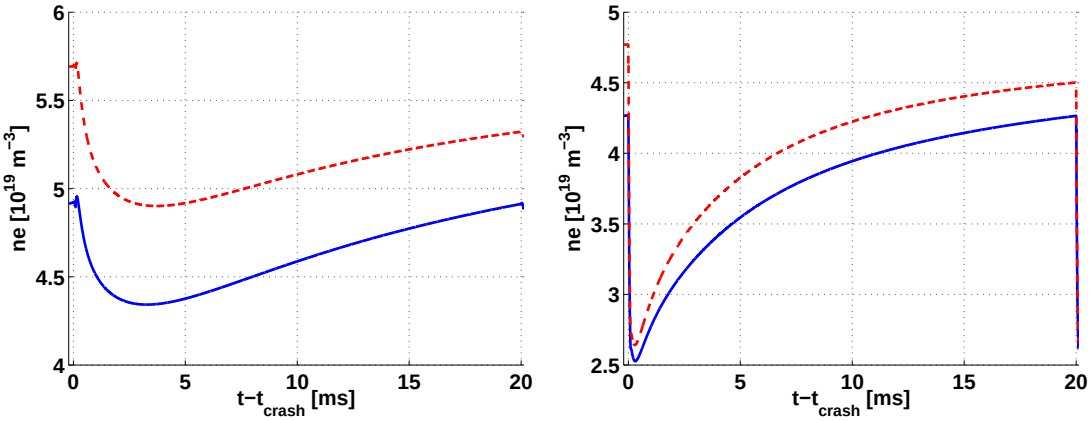

(a) (b)

Figure 5.11: Comparison between first and non-first ELM. The solid blue line is the non-first from the reference case while the dashed red one is the first. The left figure shows the traces at the top of the density pedestal while the right one is at the maximum of the pressure gradient.

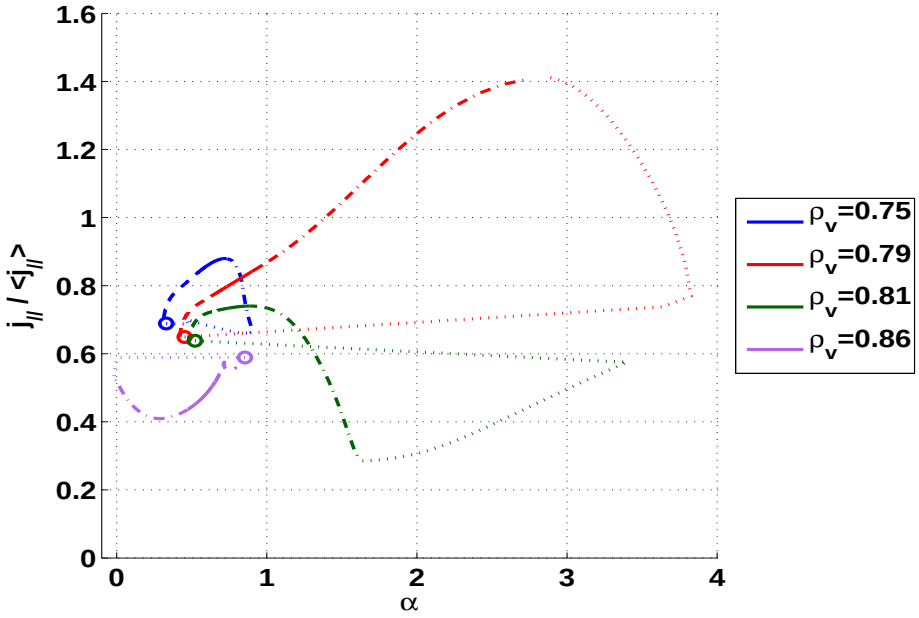

Figure 5.12: $j - \alpha$ diagram for the first ELM cycle of the reference case. Dotted lines are during the ELM crash $0 \leq t < 0.1$, dash-dotted is for $0.1 \leq t < 0.5$, solid lines are $0.5 \leq t < 1$ and dashed lines are from 1 to the next ELM (20) with the time in ms. $\rho_V = 0.75$ is the top of the density pedestal, $\rho_V = 0.79$ is where this diagram is the largest, $\rho_V = 0.81$ is the top of the temperature pedestal and $\rho_V = 0.86$ is the maximum of the pressure gradient.

5.2.4 First ELM

We can now wonder if the first ELM is the same as the following ones or if we have a behavior such that ELMs do not allow to recover fully the steady-state profiles. To investigate this we will compare the first ELM to that previously studied, say the eleventh. This is done for the different cases where we have changed D_n.

The standard case show no significant change between the first and the non-first ELMs. The most significant one is on the density time trace at the top of its pedestal (fig. 5.11a). We note that the non-first recovers to the pre-crash value just before the next crash, whether the first suffers some losses.

Comparing the $j - \alpha$ graph of the first ELM in the reference case (fig. 5.12) to that of the

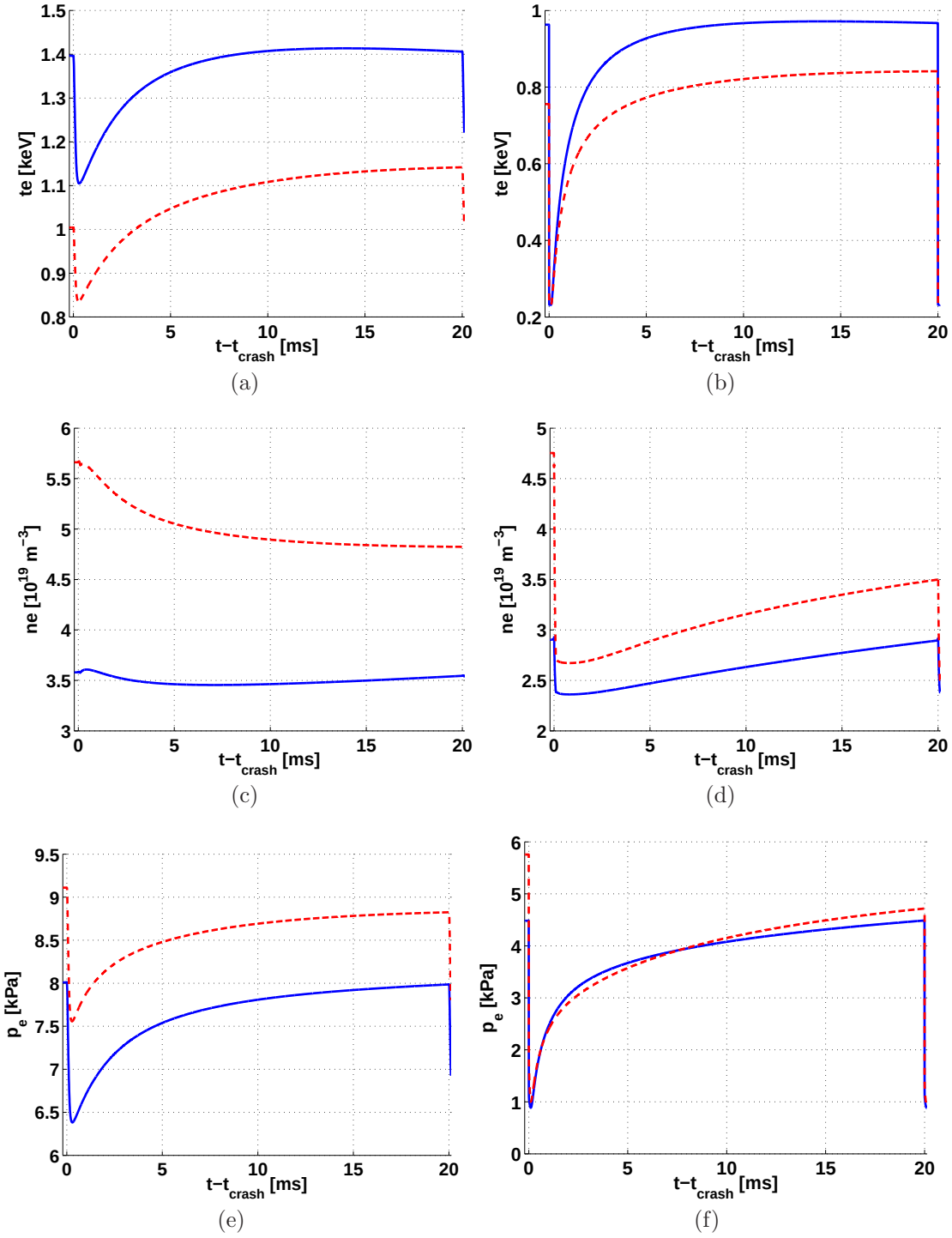

Figure 5.13: Comparison between first and non-first ELM. The solid blue line is the non-first from the "Dn01" case while the dashed red one is the first. The left figures show the traces at the top of the density pedestal while the right ones are at the maximum of the pressure gradient.

non-first (fig. 5.5), we observe that the diagram has been slightly shifted towards the bottom-left corner from the first to the elventh, yielding a gradual decrease of both the pressure gradient and the edge current density among the ELMs.

The case "Dn10" shows less of these, but these changes are also present (results shown in appendix C.3). Comparing the first ELM to the non-first for the case with half-diffusion coefficient, the density recovery time is not much affected. Other quantities show no significant

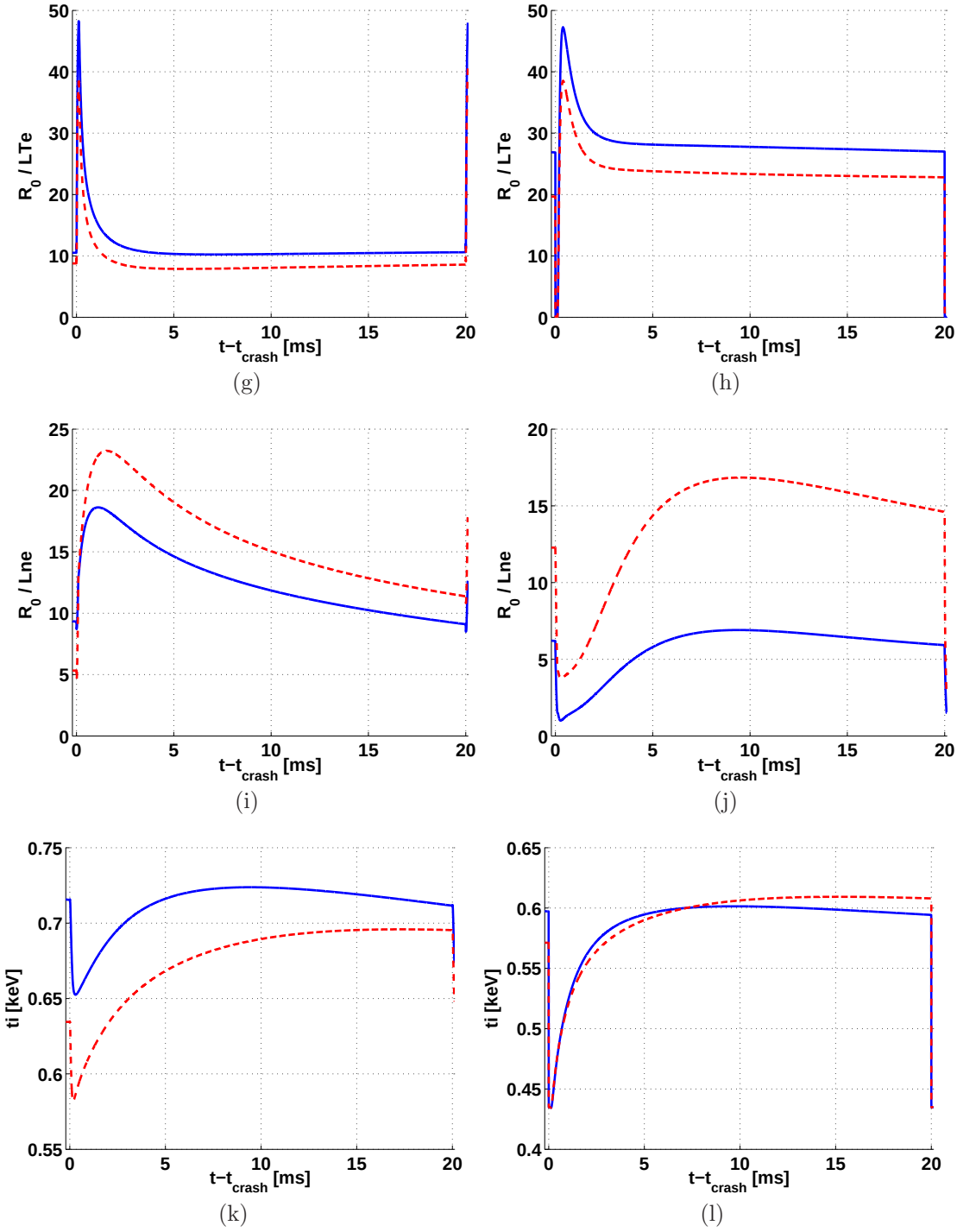

Figure 5.13: Comparison between first and non-first ELM. The solid blue line is the non-first from the "Dn01" case while the dashed red one is the first. The left figures show the traces at the top of the density pedestal while the right ones are at the maximum of the pressure gradient.

changes. Graphs can be seen in appendix C.3.

The tenth-diffusivity case is more interesting (fig. 5.13). If we recall of the diffusion time definition (3.10), dividing the particle diffusivity by ten means multiplying the diffusion time by the same factor. It is then understandable that the recovery time, which is related to the diffusion time, is longer and that the recovery may not be finished when the next ELM comes. This yields a gradual decrease.

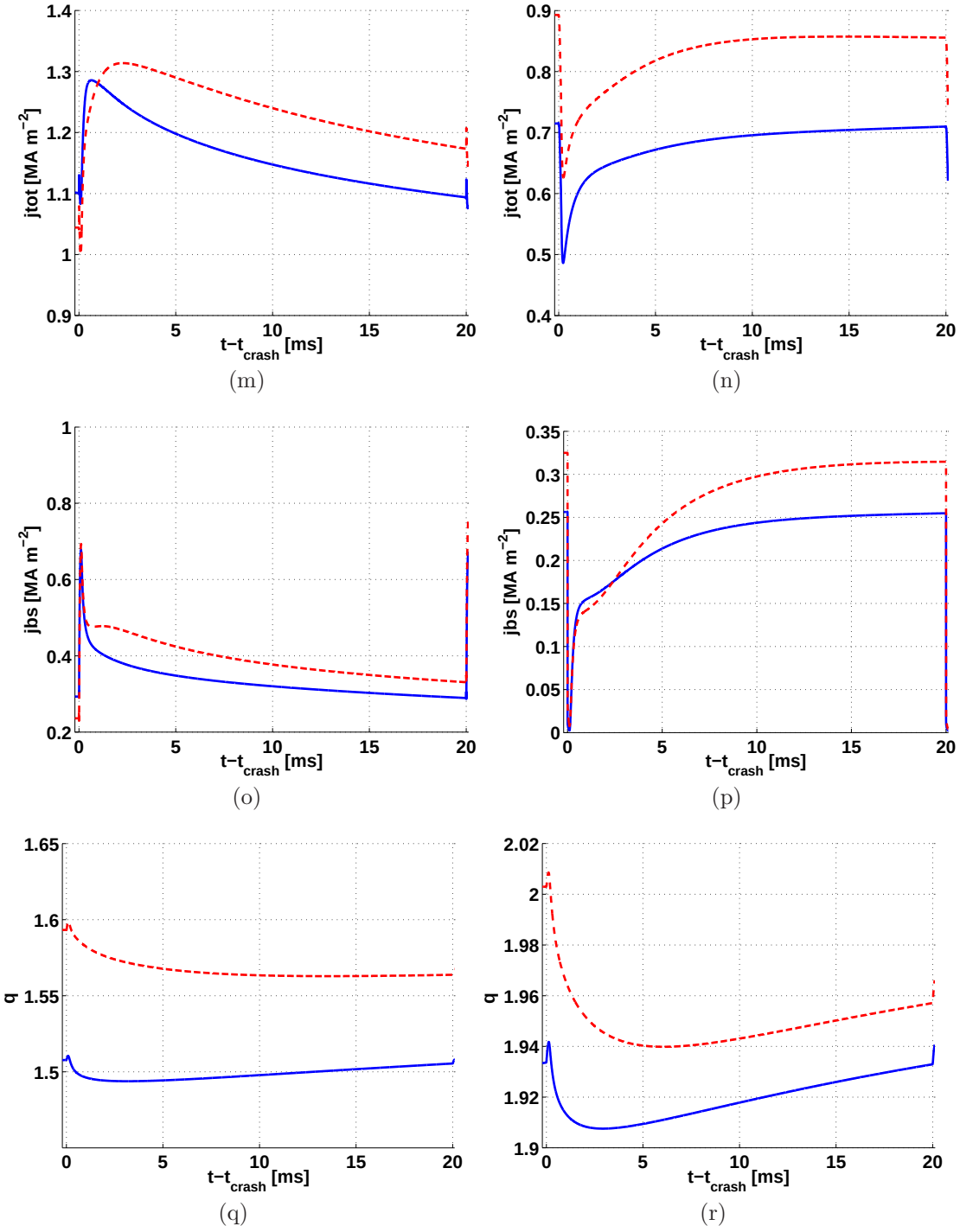

Figure 5.13: Comparison between first and non-first ELM. The solid blue line is the non-first from the "Dn01" case while the dashed red one is the first. The left figures show the traces at the top of the density pedestal while the right ones are at the maximum of the pressure gradient.

We clearly see that this change affects a lot the plasma. The density time traces (figures 5.13c and d) show that its pedestal does not fully recover when the first happens, and almost recovers for the non-first but not fully. The first presents a very large drop of density at the top of its pedestal; but this drop does not come from the ELM itself as it happens during the recovery phase. The ELM losses there are of the same order as the non-first. At the maximum of the pressure gradient, on the other hand, the ELM creates a huge loss of particles. Building the pedestal again yield the core has to provide particles too.

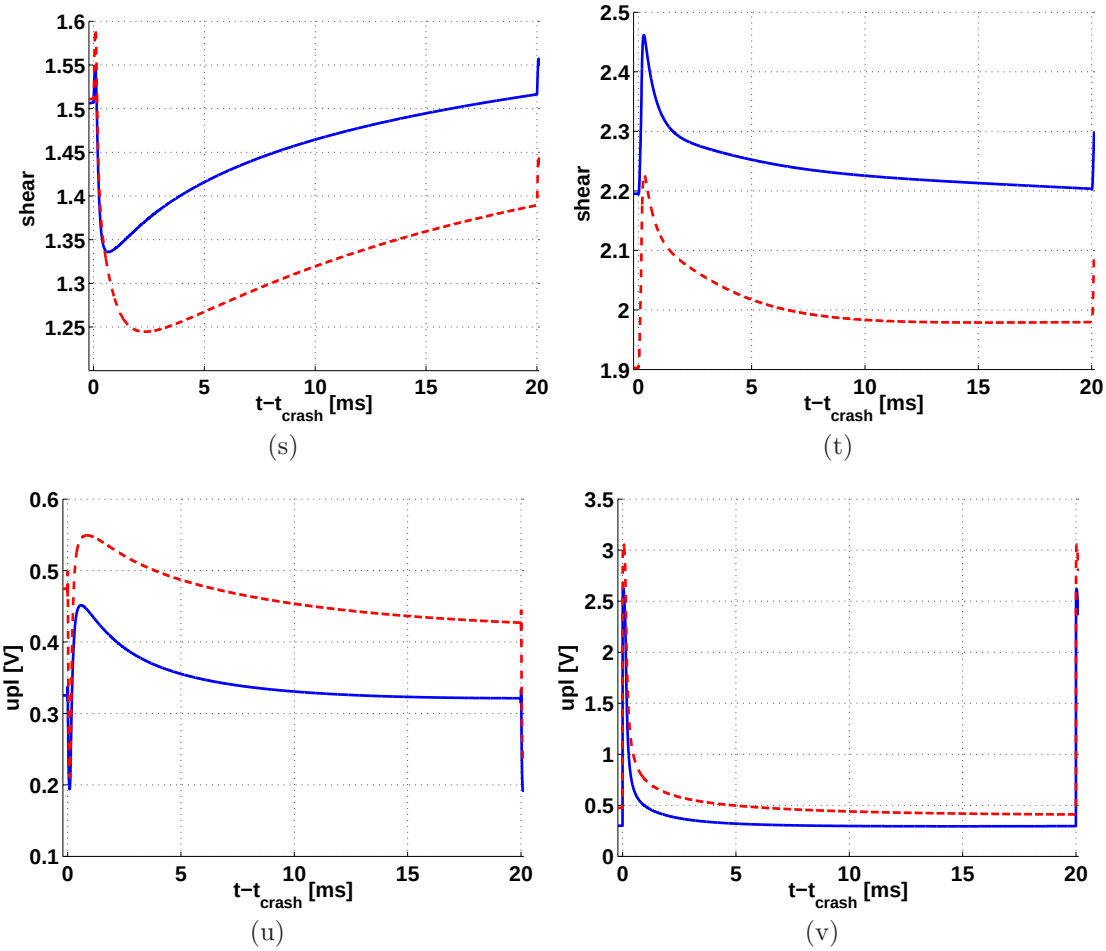

Figure 5.13: Comparison between first and non-first ELM. The solid blue line is the non-first from the "Dn01" case while the dashed red one is the first. The left figures show the traces at the top of the density pedestal while the right ones are at the maximum of the pressure gradient.

This density difference yields a change in the other way for the temperature since the heating remains the same, increasing the core temperature as can be seen in fig. 5.13a. This loss also means less equipartition which reduces the ion temperature as shown in figures 5.13k and l. The safety factor (shown in figures 5.13q and r) also exhibits a more pronounced behavior in this case.

5.2.5 Link between D_n and the ELM period

The density time traces of the reduced particle diffusion coefficients seemed to be stretched and cut after the same time anyway. This looks like we had reduced the ELM period and normalized the abscissa. We try this case by dividing the ELM period by two to compare the change of the particle diffusivity to that of the ELM period. To compare the results, we now display them using the ELM period as abscissa, meaning zero is the crash considered and one is the next crash. We have tested a case with half the period of the reference case. The ELM duration was kept the same to ensure the post-crash values to be accurate, which yields for a normalized abscissa that the case of half-period seems to have an ELM duration of twice those of the other cases.

The density time traces (figures 5.14a and b) show what we expected: the reduction of the ELM period acts in the same way as the reduction of the particle diffusion coefficient. The

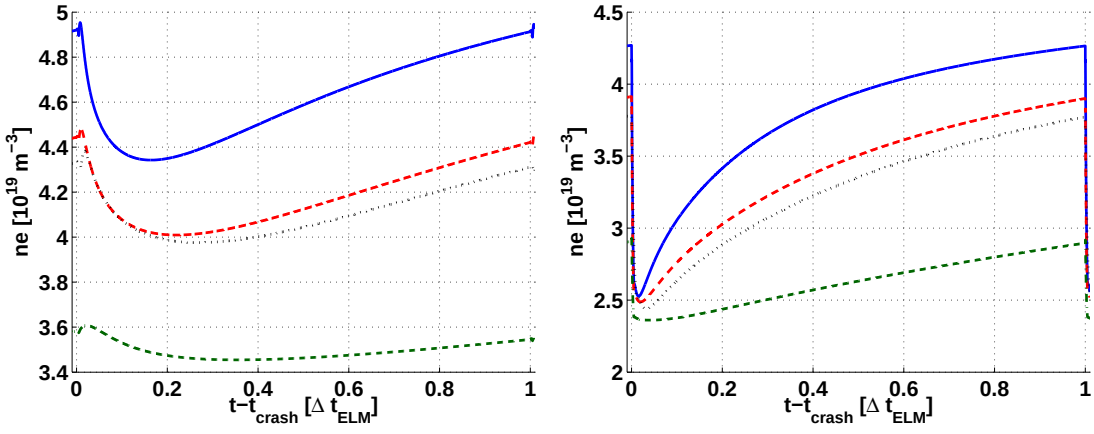

Figure 5.14: Density comparison between for different particle diffusion coefficients and different inter-ELM periods. The solid blue line is the reference case, the dashed red one is the "Dn05" case, the dash-dotted dark green is "Dn01" and the dotted black is with half the ELM period. The left figure shows the traces at the top of the density pedestal while the right one is at the maximum of the pressure gradient. The left figure shows the traces at the top of the density pedestal while the right one is at the maximum of the pressure gradient.

quantification of this observation is more difficult. We note that dividing the period by two seems to change the plasma like dividing the diffusivity by the same factor. The link between the particle diffusivity and the ELM period is obviously that when reducing one of them, the density has less time to recover, which may lead to a gradual decrease. Further studies are required to establish this link.

The other time traces are shown in appendix C.4. We must be careful with this abscissa when speaking of the characteristic times, because it is normalized to the ELM period. As we guessed from the figure 5.4, they do not show any significant difference.

5.2.6 Varying the ELM interaction range

Our reference case used an ELM range that was based upon the density pedestal width. This choice was mainly motivated by experimental observations [28]. MHD activity is not necessarily linked to transport activity. Therefore these two widths have no reason to be the same. It is of interest to change the ELM interaction range to observe the behavior of the transport phenomena when the MHD activity range is not linked to them. We have thus run a simulation with the ELM interaction range doubled. The density pedestal has a width of around $3cm$ thus we now take an interaction range of $6cm$ for the ELM (approximately $0.67 < \rho_\Phi \leq 1$ instead of $0.78 < \rho_\Phi \leq 1$).

The profiles of figure 5.15 show the same behavior as the reference case (fig. 5.3) except that the range of the ELM is broader.

Looking at the time traces, the temperature (fig. 5.16a and b) has a much larger drop, and the recovery takes much more time than in the standard case. This is because the temperature has crashed on a very broad region (around the third of the plasma radius) and thus the energy has been lost over the latter. It is understandable that it needs more time since it has more energy to recover.

The temperature gradient length also climbs less at ρ_1, because the connection between the region flattened by the ELM and the intact region is more inside the plasma. The ion temperature (fig. 5.16e) has the same behavior as the electron's since its heat source comes

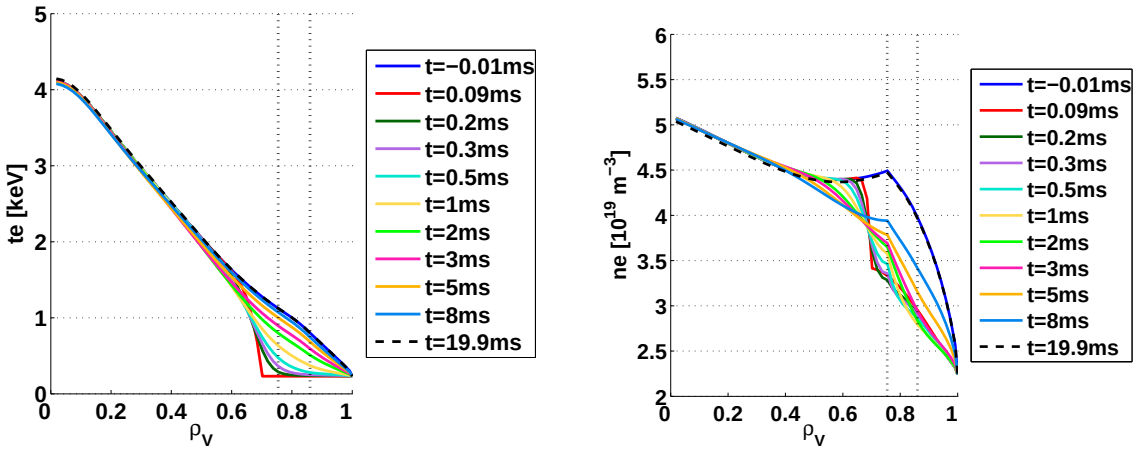

(a) (b)

Figure 5.15: Profiles of the main quantities for the case where we double the ELM range.

from the electron energy.

The density at the top of its pedestal (shown on fig. 5.16c) also has the relaxation due to our model: right after the crash the temperature gradient becomes high for the recovery, implying a high value for V_n/D_n. As the temperature recovers, its gradient flattens, reducing the previous ratio. Since it only changes the pinch velocity ($D_n = 0.2\chi_E$), it means that the first phase after the crash has a high pinch velocity then lower, allowing particles to move faster at first but slower afterwards. This is what we observe on this time trace.

At ρ_2 (figure 5.16d) we have the same behavior as the temperature showed at ρ_1, a longer recovery time due to the larger losses. Both density gradient length (figs. 5.16i and j) also take more time to recover.

These facts imply that the pressure also recovers slower in this case and so does the pedestal bootstrap current. The total current density time traces (figs. 5.16m and n) seem shifted due to the ELM shift. The time trace here at ρ_1 is somehow like that of the reference case at ρ_2.

The safety factor still does not vary much, but at ρ_2 we see a larger recovery time which is what we expected since it depends on the currents. The magnetic shear also presents the same behavior as the current densities, more clearly than the safety factor.

The ELM being much larger, we understand that the energy losses here are higher. The absolute energy drop is about $3.2kJ$, almost twice as much as the reference case. Also, the plasma energy is higher, because the temperature has grown from the gradual decrease of density. The central pre-crash electron temperature is around $0.5keV$ higher here than in the reference case.

The MHD diagram for this case, fig. 5.17, is completely different to that of the reference case (fig. 5.5). Here we only have the ELM crash making a pressure gradient loss at almost constant edge current density. There is a small loss of edge current density only at the end of the crash.

The presented cycles are all rebuilding the same way on this diagram. First the normalized edge current density decreases, probably due to the loss of pressure gradient. The resistive time τ_η (3.11) seems to be longer than the energy confinement time (3.6). Then the pressure gradient builds up and finally both increase. Depending on the location, the normalized edge current density increases more or less fast. At the top of the density pedestal $\rho_V = 0.75$, the pressure gradient and the normalized edge current density have already begun to increase after only $0.5ms$, whilst at the maximum of the pressure gradient $\rho_V = 0.86$ only the pressure gradient

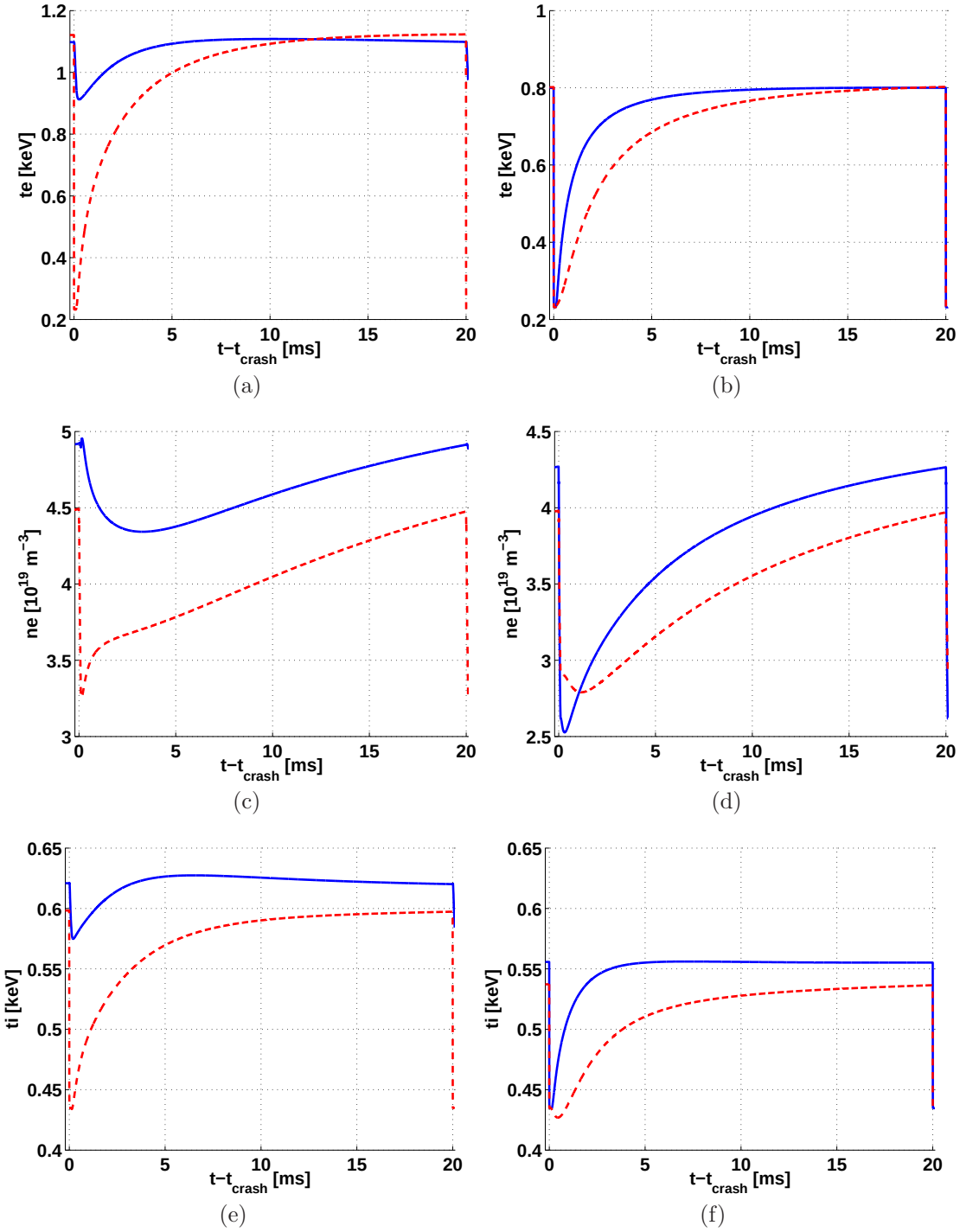

Figure 5.16: Time traces of the main quantities for the case where we double the ELM range. The left figures show the traces at the top of the density pedestal while the right ones are at the maximum of the pressure gradient.

grows up until $1ms$ before the normalized edge current density begins too.

We note that the pressure gradient grows much more at the maximum of itself than at any other location displayed. Unlike the reference case, we have a longer path for the last phase before the next ELM. The pressure gradient needs much more time to rebuild since the density has been affected further than the top of its pedestal.

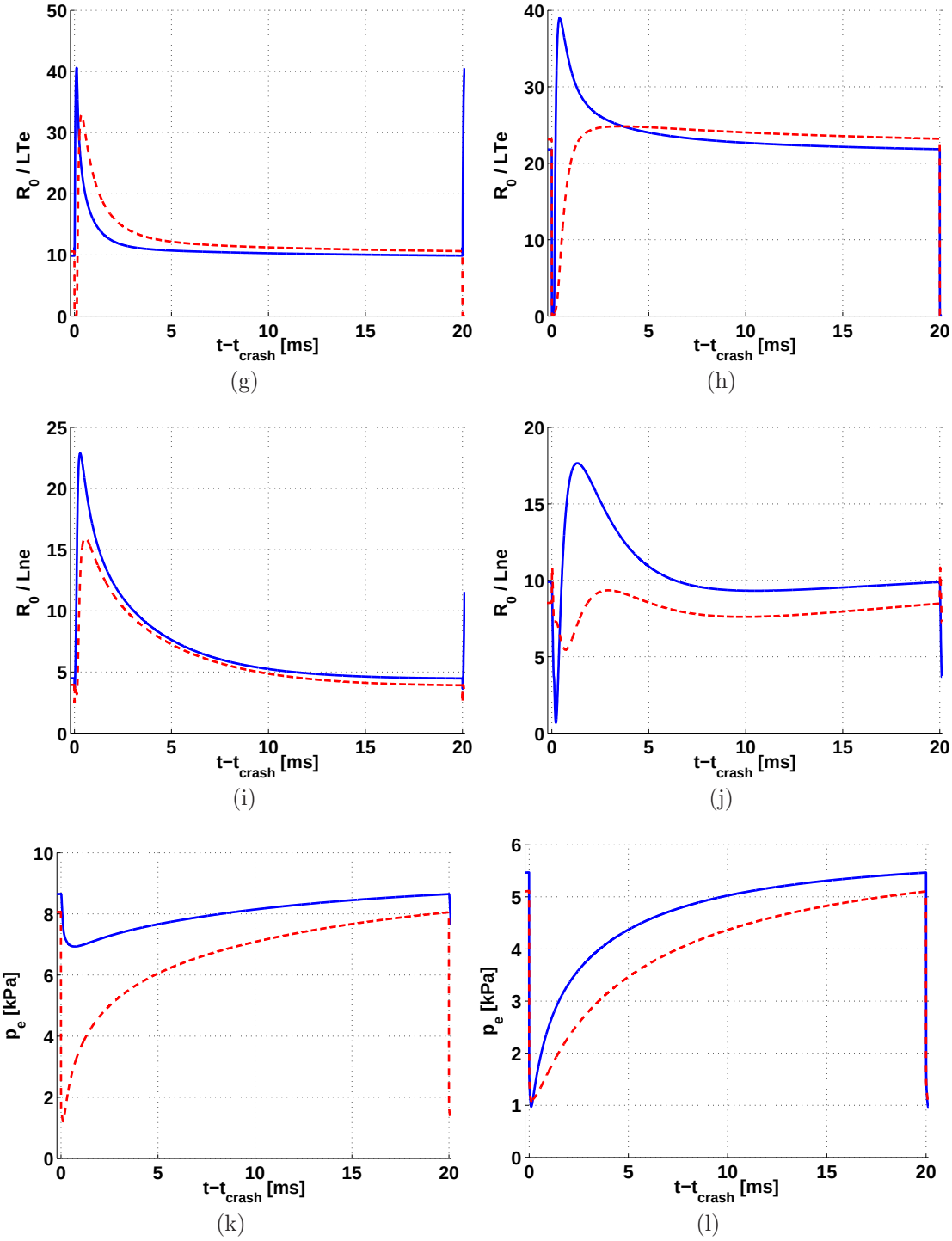

Figure 5.16: Time traces of the main quantities for the case where we double the ELM range. The left figures show the traces at the top of the density pedestal while the right ones are at the maximum of the pressure gradient.

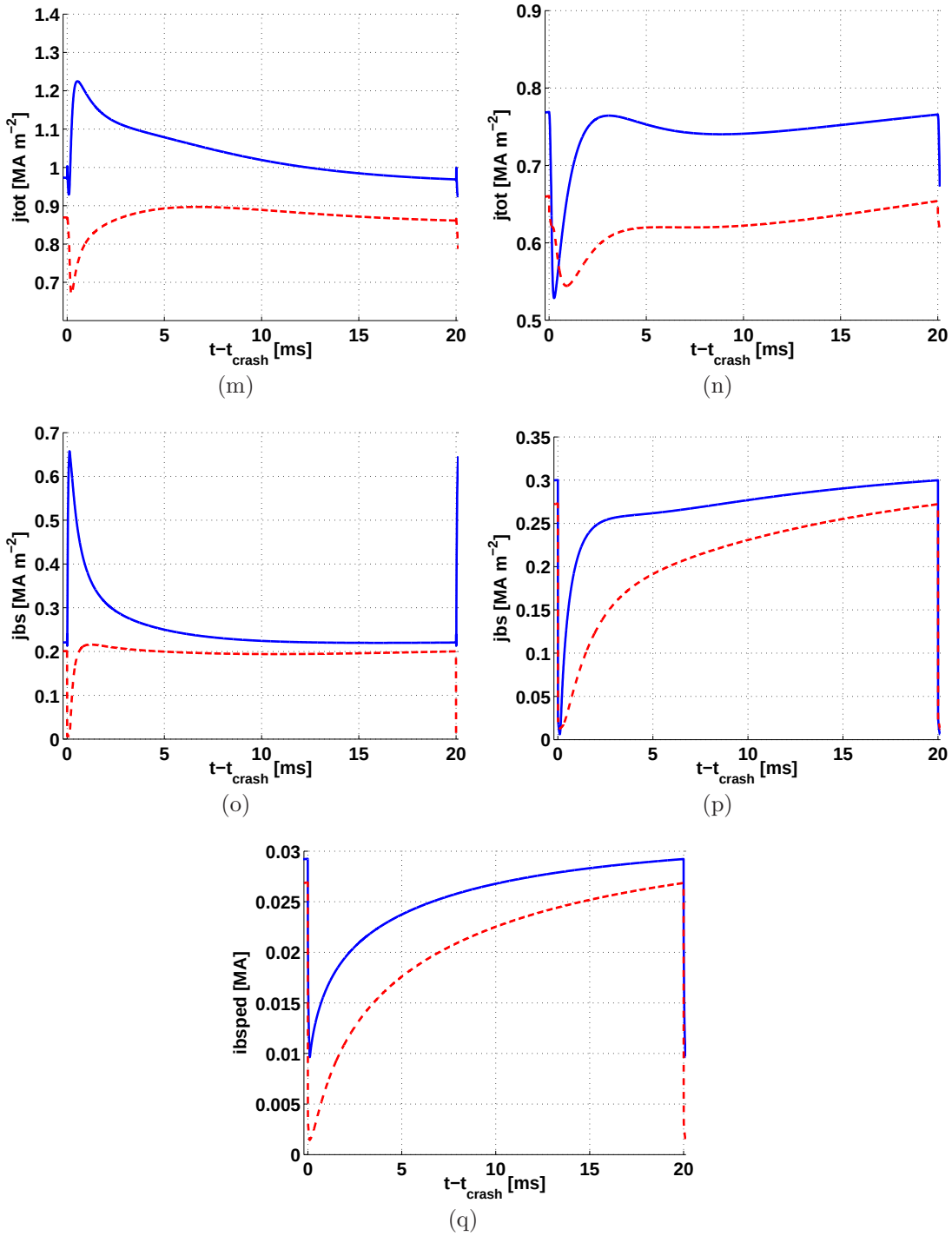

Figure 5.16: Time traces of the main quantities for the case where we double the ELM range. The left figures show the traces at the top of the density pedestal while the right ones are at the maximum of the pressure gradient.

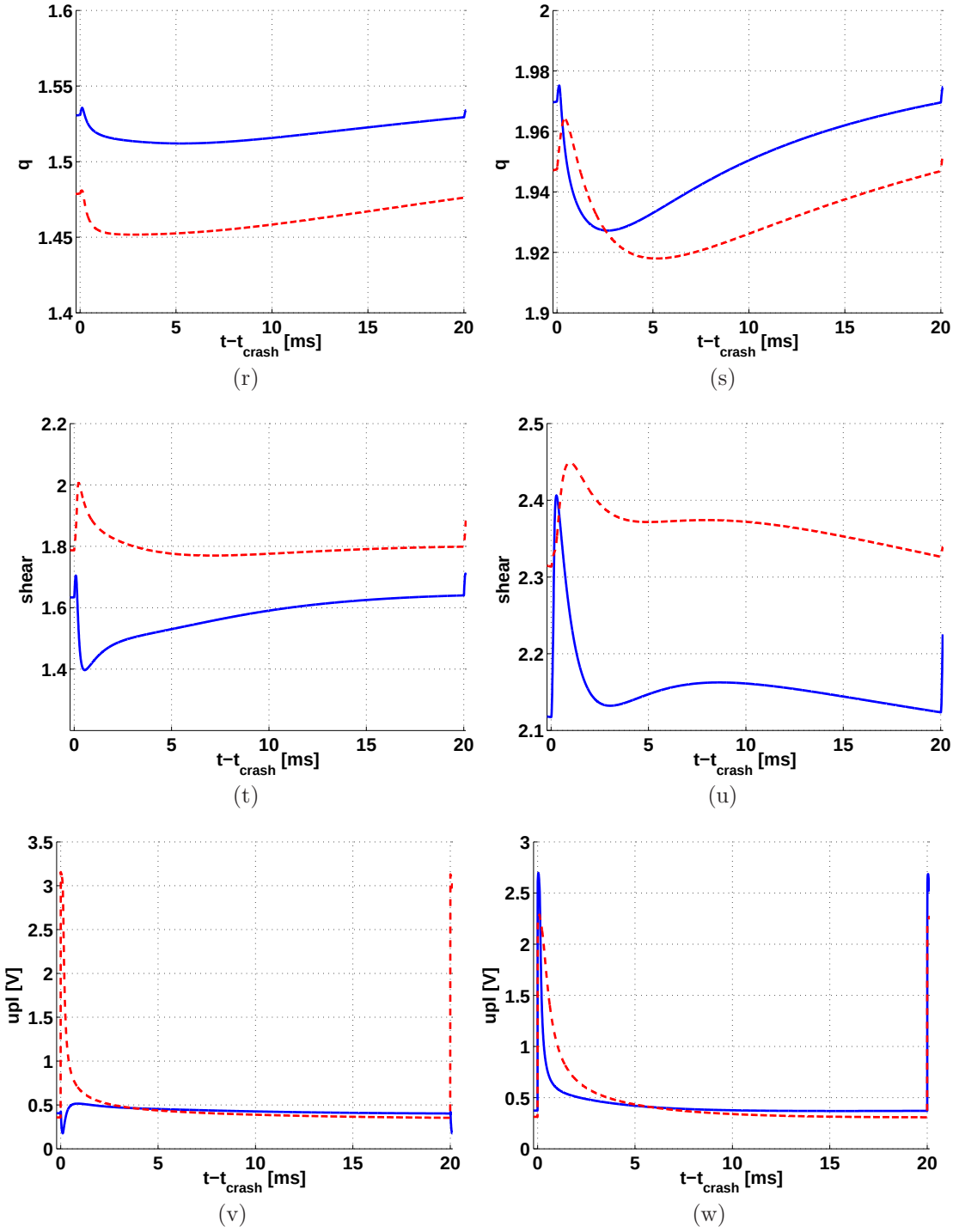

Figure 5.16: Time traces of the main quantities for the case where we double the ELM range. The left figures show the traces at the top of the density pedestal while the right ones are at the maximum of the pressure gradient.

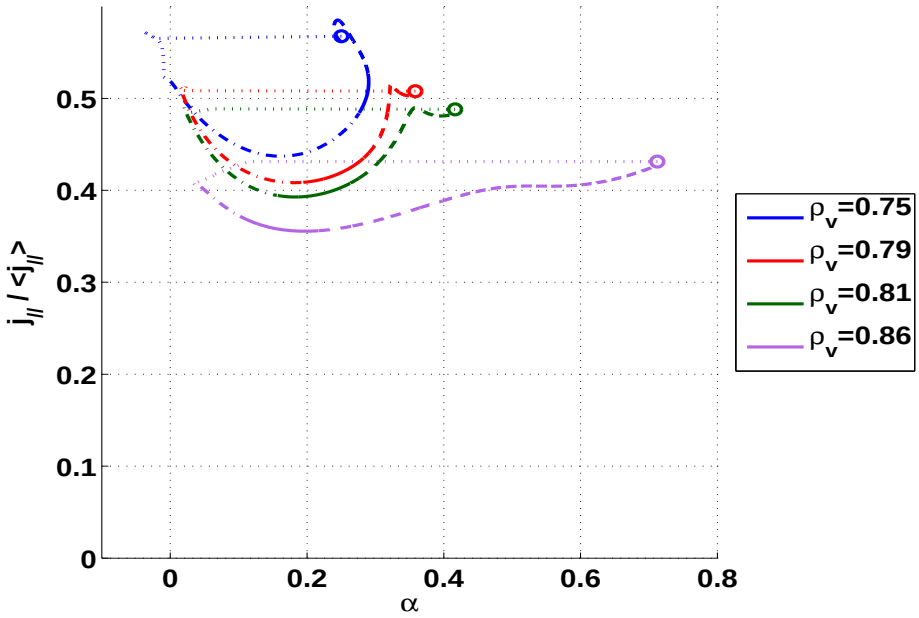

Figure 5.17: $j - \alpha$ diagram for the wider ELM cycle. Dotted lines are during the ELM crash $0 \leq t < 0.1$, dash-dotted is for $0.1 \leq t < 0.5$, solid lines are $0.5 \leq t < 1$ and dashed lines are from 1 to the next ELM (20) with the time in ms. $\rho_V = 0.75$ is the top of the density pedestal, $\rho_V = 0.79$ is where this diagram is the largest, $\rho_V = 0.81$ is the top of the temperature pedestal and $\rho_V = 0.86$ is the maximum of the pressure gradient.

Chapter 6

Conclusion

Building a relevant χ_e profile, we were able to run H-mode simulations. We successfully made it by taking a standard L-mode profile (i.e. parabolic) truncated at the edge to create the barrier. Moreover, to be as accurate as possible with the predictions of empirical laws, we scaled the core profile with a factor depending on the energy confinement time scaling.

The pedestal χ_e was scaled with the relation from [12] between the core and the pedestal energies $W_{\text{core}} \simeq 3.5 W_{\text{ped}}$. Imposing this relation to determine the height of the temperature pedestal yields a good agreement with the experimental data. This link between the core and the pedestal energies has been successfully used and could be used to scale the ion thermal diffusivity as well.

For the density pedestal, we implemented the relation $V_n/D_n \simeq 0.5\ \nabla T_e/T_e$ that yields the relation $L_n \simeq 2L_T$ found in eITBs [14] and in ASDEX Upgrade H-mode pedestal [18]. This was achieved successfully, yielding pretty good results for the pedestal density in our simulations. Linking the pedestal density to the pedestal temperature together with the previous energy scaling was done with success, increasing our confidence in both scaling. However, when ELMs are present, it might be of interest to run a simulation with V_n/D_n fixed to the steady-state $0.5\ \nabla T_e/T_e$ profile, because the density behavior may be different in the post-crash phase.

About the ELM it was found that our model is not very good. The energy difference was not matching the experimental one. There was also some experimental observations that were not seen in our simulations, for instance about the central temperature. It could be due to some global confinement phenomenon. We also spoke of the possibility of a cascading phenomenon, as we saw our ELM model makes a steep pressure gradient at its border. The latter could then trigger an instability of the same kind and so on until it reaches the center. A last case discussed is that the MHD mode itself may be global and may influence the plasma further than just at the edge, maybe to the $q = 1$ radius, or even to the center.

The MHD criteria have also been studied and we saw on the $j_{t,a} - \alpha$ diagram that the plasma was at its pre-crash position long before the ELM comes in the reference case, around $19ms$ for an ELM period of $20ms$. ASTRA provides a way to implement a new drawing mode; it could be interesting to make it draw the $j_{t,a} - \alpha$ diagram at the maximum of the pressure gradient and at some other chosen locations to observe in run-time the stability zone and the evolution of the plasma among the ELMs. As said just above, our ELM model has to be corrected, and this may lead to a change in the MHD stability criteria evolution.

The case with only central ECH was not significantly different. All the quantities showed a similar behavior to those of the reference case. The MHD diagram was also not really changed, unless considering the steady-state changes. The heating profile seems to have insignificant

impact on the recovery behavior. However, since the confinement time is higher in the center, central heating is better than edge one and gives more energy to the plasma.

When reducing the particle diffusivity, the inter-ELM time becomes too short for the density to recover fully. It thus decreases, and so do the pressure gradient and the edge current density. The behavior of both is also slowed down. The MHD diagram showed cycles more compact, due to the slowdown of the density dynamic behavior. The density time traces, when reducing the particle diffusion coefficient, were like we had stretched them and cut them anyway after the same time. This is exactly what happens when reducing the ELM period and normalizing the abscissa. Comparing the studies when varying D_n to that of reduced ELM period, these changes act in the same way on the density since they both increase the density recovery time with regards to the ELM period.

We finally doubled the ELM interaction range to compare with the default case where we use the density pedestal width. ELM losses were much more important and the behavior of the plasma was radically changed. This lead to a change in the MHD diagram as well. It was found that the pedestal region during an ELM crash decreases mainly the pressure gradient, and after an ELM crash first increases the pressure gradient and decreases the normalized edge current density, then builds it up together with the pressure gradient. We also noted that the steady-state pressure gradient seems to grow much more at its maximum than at locations that are more inside the plasma but still in the pedestal.

In order to have a better confidence in these theoretical observations, the spatial resolution of the output of our simulations could be improved. Sawteeth are also present in H-mode plasmas and so should be in our simulations. However, their implemented model may be inaccurate and may need to be changed. Also, our ELM model uses an arbitrary value for the particle diffusion D_n^{ELM} which should be chosen by experimental observations or theoretical assumptions.

ELMs are MHD instabilities and we used a transport code. ASTRA has been written such that it is easy to add user-defined modules. It could be of interest to implement the ELM crash according to the MHD limits, instead of doing the crash manually, by writing a model that could be implemented in a separated module of the code as has already been done for the sawteeth [22]. This might give us more informations.

Bibliography

[1] J. D. Lawson, "Some criteria for a useful thermonuclear reactor," Harwell, Berkshire, UK, 1955. Cited on page 1.

[2] R. Arnoux, "How Fritz Wagner "discovered" the H-Mode," June 19 2009. [Online:] http://www.iter.org/newsline/86/659 (consulted on December 21, 2010). Cited on page 1.

[3] J. P. Freidberg, *Plasma physics and fusion energy*. Cambridge: Cambridge University Press, 2008. Cited on pages 3, 4, 5, 10, and 12.

[4] T. J. M. Boyd and J. J. Sanderson, *The Physics of Plasmas*. Cambridge: Cambridge University Press, 2007. Cited on pages 3, 4, 5, and 12.

[5] J. P. Freidberg, *Ideal Magnetohydrodynamics*. New York: Plenum Press, 1987. Cited on page 3.

[6] J. Wesson, *Tokamaks*. International Series of Monographs on Physics (118), Oxford: Clarendon Press, 3rd ed., 2004. Cited on pages 3, 7, 9, and 10.

[7] C. G. Gimblett *et al.*, "The role of edge current-driven modes in ELM activity," *Plasma Phys. Control. Fusion*, vol. 48, p. 1531, 2006. Cited on pages 5 and 6.

[8] J. A. Wesson, "Hydromagnetic stability of tokamaks," *Nucl. Fusion*, vol. 18, p. 87, 1978. Cited on page 6.

[9] D. Lortz, "The general "peeling" instability," *Nucl. Fusion*, vol. 15, p. 41, 1975. Cited on page 6.

[10] J. W. Connor *et al.*, "Magnetohydrodynamic stability of tokamak edge plasmas," *Phys. Plasmas*, vol. 5, no. 7, p. 2687, 1998. Cited on page 6.

[11] J.-S. Lönnroth *et al.*, "Predictive transport modelling of type I ELMy H-mode dynamics using a theory-motivated combined balooning-peeling model," *Plasma Phys. Control. Fusion*, vol. 46, p. 1197, 2004. Cited on page 7.

[12] A. Pitzschke, *Pedestal Characteristics and MHD stability of H-mode Plasmas in TCV*. PhD thesis, EPFL, Lausanne, 2011. EPFL thesis 4917. Cited on pages 7, 14, 16, 17, 18, 24, 25, 26, 27, 28, and 47.

[13] O. Sauter, C. Angioni, and Z. A. Pietrzyk, "*Heat diffusion coefficients from experimental profiles on TCV.*". Cited on page 9.

[14] E. Fable *et al.*, "Inward thermodiffusive particle pinch in electron internal transport barriers in TCV," *Plasma Phys. Control. Fusion*, vol. 48, no. 9, p. 1271, 2006. Cited on pages 9, 13, and 47.

[15] K. Itoh, S.-I. Itoh, and A. Fukuyama, *Transport and Structural Formation in Plamsas*. Plasma Physics Series, Bristol: Institute of Physics Publishing, 1999. Cited on page 10.

[16] ITER Physics Expert Groups on Confinement and Transport and others, "Chapter 2: Plasma confinement and transport," *Nucl. Fusion*, vol. 39, no. 12, p. 2175, 1999. Cited on page 11.

[17] F. Ryter *et al.*, "Experimental Evidence for Gradient Length-Driven Electron Transport in Tokamaks," *Phys. Rev. Lett.*, vol. 86, no. 11, p. 2325, 2001. Cited on page 12.

[18] J. Neuhauser *et al.*, "Transport into and across the scrape-off layer in the ASDEX Upgrade divertor tokamak," *Plasma Phys. Contr. Fusion*, vol. 44, p. 855, 2002. Cited on pages 13 and 47.

[19] F. Piras *et al.*, "Snowflake Divertor Experiments on TCV," *Plasma Phys. Control. Fusion*, vol. 52, p. 124010, 2010. Cited on page 14.

[20] F. Piras *et al.*, ""Snowflake" H-mode in a tokamak plasma," *Phys. Rev. Lett.*, vol. 105, p. 155003, 2010. Cited on page 14.

[21] G. V. Pereverzev and P. N. Yushmanov, *ASTRA Automated System for TRansport Analysis*. IPP, Max-Planck-Institut für Plasmaphysik, München, February 2002. Cited on page 15.

[22] E. Fable *et al.*, "Sawtooth relaxation model package in Fortran 90," tech. rep., Integrated Tokamak Modelling Task Force, EFDA, München, 2007. Cited on pages 15 and 48.

[23] R. Behn *et al.*, "The Thomson Scattering Diagnostic on TCV," in *7th International Symposium on Laser-aided plasma diagnostics (LAPD-7)*, pp. 392–397, 1995. Cited on page 16.

[24] P. Bosshard, *Confinement ionique dans le tokamak TCV mesuré par spectroscopie d'échange de charge.* PhD thesis, EPFL, Lausanne, 2003. EPFL thesis 2723. Cited on page 16.

[25] C. Angioni and O. Sauter, "Neoclassical transport coefficients for general axisymmetric equilibria in the banana regime," *Phys. Plasmas*, vol. 7, p. 1224, 2000. Cited on page 16.

[26] K. Matsuda, "Ray Tracing Stduy of the Electron Cyclotron Current Drive in DIII-D Using 60 GHz," *IEEE Trans. Plasma Sci.*, vol. 17, no. 1, p. 6, 1989. Cited on page 16.

[27] E. Fable, *Experimental and Theoretical Study of Particle Transport in the TCV Tokamak*. PhD thesis, EPFL, Lausanne, June 2009. EPFL thesis 4334. Cited on page 17.

[28] A. Bruckhart *et al.*, "Inter-ELM behaviour of the electron density and temperature pedestal in ASDEX Upgrade," *Plasma Phys. Control. Fusion*, vol. 52, p. 105010, 2010. Cited on page 40.

[29] R. B. White, *The theory of toroidally confined plasmas*. London: Imperial College Press, 2006. Not cited.

[30] R. D. Hazeltine and J. D. Meiss, *Plasma Confinement*. Mineola: Dover Publications, Inc., 2003. Not cited.

[31] J. B. Lister, *Physique des plasmas III (Fusion Controlêe)*. CRPP-EPFL, 2010. Not cited.

[32] F. Porcelli, D. Boucher, and M. N. Rosenbluth, "Model for the sawtooth period and amplitude," *Plasma Phys. Control. Fusion*, vol. 38, no. 12, p. 2163, 1996. Not cited.

[33] E. Asp *et al.*, "Electron thermal transport analysis in Tokamak à Configuration Variable," *Phys. Plasmas*, vol. 15, p. 082317, 2008. Not cited.

[34] W. M. Stacey and R. J. Groebner, "Experimentally inferred thermal diffusivities in the edge pedestal between edge-localized modes in DIII-D," *Phys. Plasmas*, vol. 14, p. 122504, 2007. Not cited.

[35] W. M. Stacey and R. J. Groebner, "Interpretation of particle pinches and diffusion coefficients in the edge pedestal of DIII-D H-mode plasmas," *Phys. Plasmas*, vol. 16, p. 102504, 2009. Not cited.

[36] A. Y. Pankin *et al.*, "Combined model for the H-mode pedestal and ELMs," *Plasma Phys. Control. Fusion*, vol. 47, p. 483, 2005. Not cited.

[37] J.-S. Lönnroth *et al.*, "Predictive transport modelling and MHD stability analysis of mixed type I-II ELMy H-mode JET plasmas," *Plasma Phys. Control. Fusion*, vol. 46, p. 767, 2004. Not cited.

[38] P. B. Snyder *et al.*, "Edge localized modes and the pedestal: A model based on coupled peeling-ballooning modes," *Phys. plasmas*, vol. 9, no. 5, p. 2037, 2002. Not cited.

[39] A. Y. Pankin *et al.*, "Theory-based model for the pedestal, edge stability and ELMs in tokamaks," *Nucl. Fusion*, vol. 46, p. 403, 2006. Not cited.

[40] B. Gulejova, *SOLPS Modelling of ELMing H-mode*. PhD thesis, EPFL, Lausanne, February 2010. EPFL thesis 4562. Not cited.

[41] C. Angioni, *Modelling of electron transport and of sawtooth activity in tokamaks*. PhD thesis, EPFL, Lausanne, 2001. EPFL thesis 2469. Not cited.

[42] S. Y. Medvedev *et al.*, "Edge kink/ballooning mode stability in tokamaks with separatrix," *Plasma Phys. Control. Fusion*, vol. 48, no. 7, p. 927, 2006. Not cited.

[43] V. Igochine *et al.*, "Structure and dynamics of sawteeth crashes in ASDEX Upgrade," *Phys. Plasmas.*, vol. 17, p. 122506, 2010. Not cited.

[44] F. L. Hinton and R. D. Hazeltine, "Theory of plasma transport in toroidal confinement systems," *Rev. Mod. Phys.*, vol. 48, no. 2, p. 239, 1976. Not cited.

Acknowledgements

This work was really enjoyable for me as it is my first step in the scientific research. I have been glad to learn it and how to work as a scientist. I am particularly thankful to my supervisor Dr. Olivier Sauter for all his help and support. He taught me how a scientist must think and what one has to look for and understand as a scientific person.

Dr. E. Fable has also been helpful with his sawtooth package and the package-support and I thank him for it. I also would like to thank Dr. Alexander Karpushov for the ion temperature data management, Dr. B. P. Duval for his computer and psychological support, Prof. Jo Lister, F. Felici for the ASTRA-hotline, and A. Pitzschke, L. Curchod and all the PhD students for the many helps, advices and else they gave to me.

Appendix A

Sources of experimental data used

Path of the ASTRA input files used on LAC: /home/induni/astra/exp/40080_0.8_EXP and /home/induni/astra/equ/TCV_H, informations about the dumb parameters can be found on the CRPP Wiki on the page User:Induni/ASTRA/TCV_H

Shot number	**Time taken**	Z_{eff}	**Comments**
29892	0.53	2.2	SN Ohmic
	0.7	3.5	SN
	1.0		SN
	1.3		SN
39857	0.6	1.55	SN
	1.044		SF
39863	0.86	1.7	SN
39874	0.5	2.0	SN
	1.3		SF+
40045	1.099	1.8	SN
40080	0.8	2.9	SN
40346	1.255	3.0	SN
40378	1.253	2.9	SN
40894	0.85	2.9	SN

Appendix B

Fortran subroutines for ASTRA

B.1 Energy scaling

Listing B.1: Energy scaling, path on LAC: /home/induni/astra/sbr/wscaling.f

```
! Scaling for W changing HE
! By G. Induni (2010)
      subroutine WSCALING(int_p_input,scaling_factor)
      implicit none
      include 'for/parameter.inc'
      include 'for/const.inc'
      include 'for/status.inc'
      double precision THQ99,NECHR,WE,WI,int_p_input,
     & tau_scal,tau_inst,ratio,scaling_factor
      double precision, dimension(1:NA1) :: we_now,wi_now
      integer j
      do j = 1,NA1
        include 'fml/we'
        we_now(j)=WE
        include 'fml/wi'
        wi_now(j)=WI
      enddo
      include 'fml/thq99'
      tau_scal=THQ99/int_p_input**0.69              ! Scaling tau_E,H98
      tau_inst=(wi_now(NA1)+we_now(NA1))/int_p_input ! Instant. tau_E
      scaling_factor=tau_inst/tau_scal
      return
      end
```

B.2 Pedestal scaling

Listing B.2: Pedestal scaling, path on LAC: /home/induni/astra/sbr/pedscaling.f

```
! Scaling for W_ped
! By G. Induni (2010)
      subroutine PEDSCALING(back,do_scaling,rho_in,corr_coeff)
```

```
      implicit none
      include 'for/parameter.inc'
      include 'for/const.inc'
      include 'for/status.inc'
      real*8, dimension(1:NA1) :: we_now,wi_now,rho_vol
      double precision wtot_now,w_ped,w_core,wcoreped_scal,
     & WE,WI,rho_ped,back,new_factor,do_scaling,
     & rho_in,corr_coeff
      integer j,irho_ped
      if( back .eq. 0 ) then ! initializing
        back=1.
      endif
      ! Storing WE and WI 'profiles'
      do j = 1,NA1
        include 'fml/we'
        we_now(j)=WE
        include 'fml/wi'
        wi_now(j)=WI
      enddo

      rho_vol=SQRT(VOLUM/MAXVAL(VOLUM))
      ! Rounded index of pedestal position
      irho_ped=MINLOC(ABS(rho_vol-rho_in),1)
      rho_ped=rho_vol(irho_ped)

      ! Total energy
      wtot_now=we_now(NA1)+wi_now(NA1)
      ! Core energy
      w_core=we_now(irho_ped)+wi_now(irho_ped)
      ! Pedestal energy
      w_ped=wtot_now-w_core

      ! Core to pedestal scaling
      wcoreped_scal=3.5*corr_coeff

      write(19,'(a,f7.5,a,i2,a,f5.3,a,f4.1,a,f5.2,a,f5.2)')
     &     't=',TIME,' irho=',irho_ped,' rhovol_ped=',rho_ped,
     &     ' ',wcoreped_scal,'=',w_core/w_ped,' fac=',back
      if( do_scaling .ne. 0 ) then
        new_factor=(w_core/w_ped)/wcoreped_scal
        back=MAX(back/new_factor,0.01)
      endif
      return
      end
```

Appendix C

Additional graphs

C.1 Edge EC heating replaced by central

C.1.1 Profiles

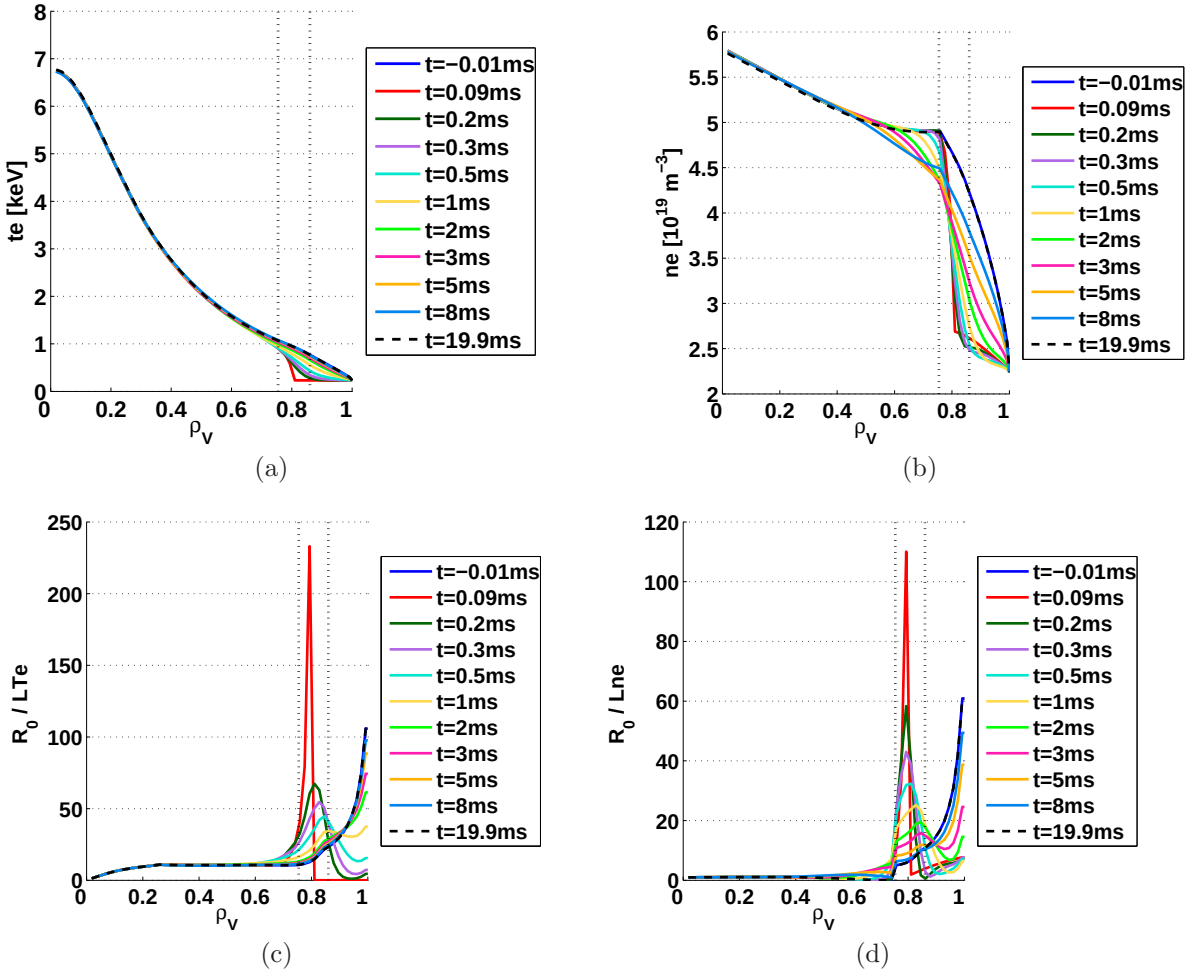

Figure C.1: Profiles of the main quantities where we have replaced the edge ECH by central one.

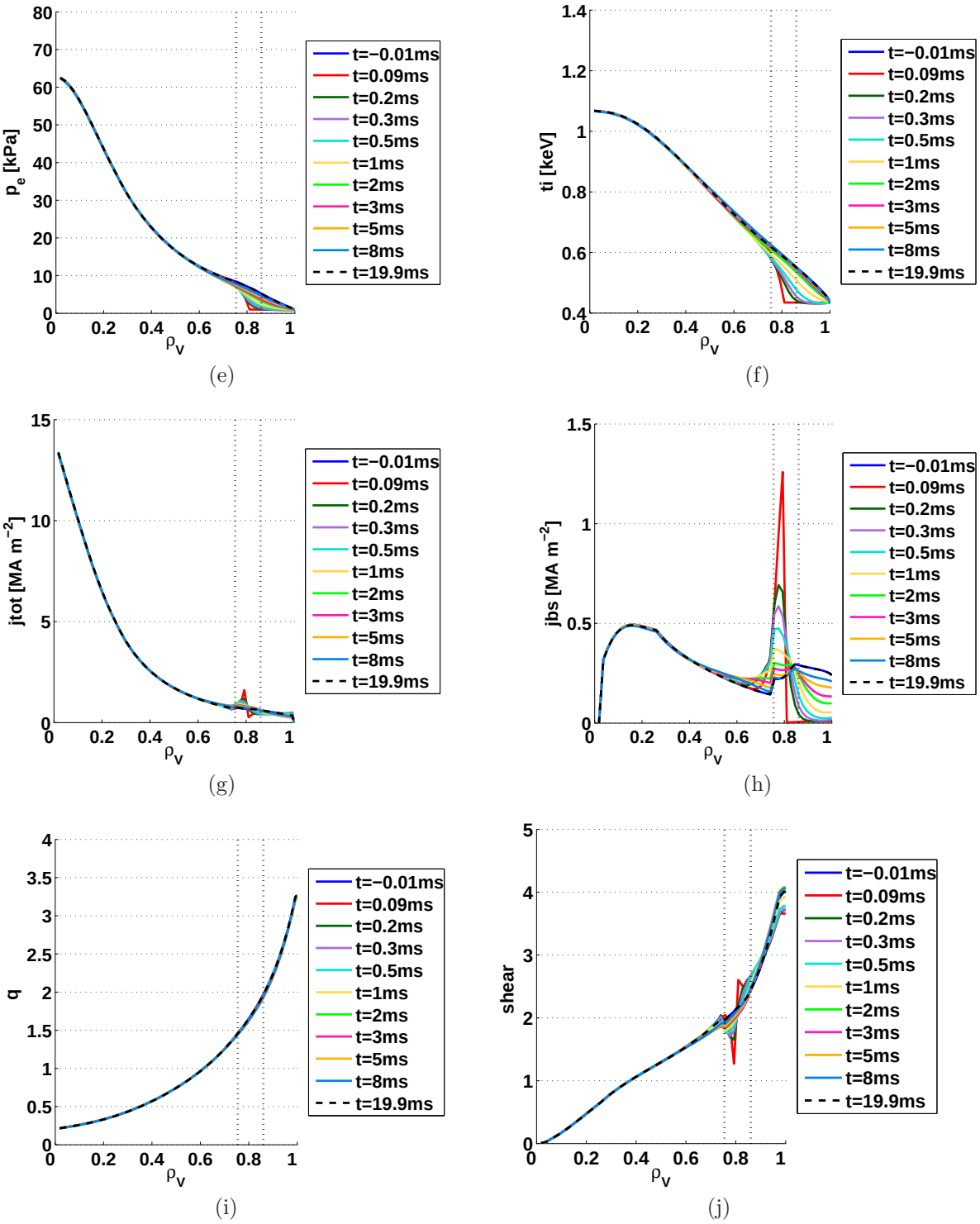

Figure C.1: Profiles of the main quantities where we have replaced the edge ECH by central one.

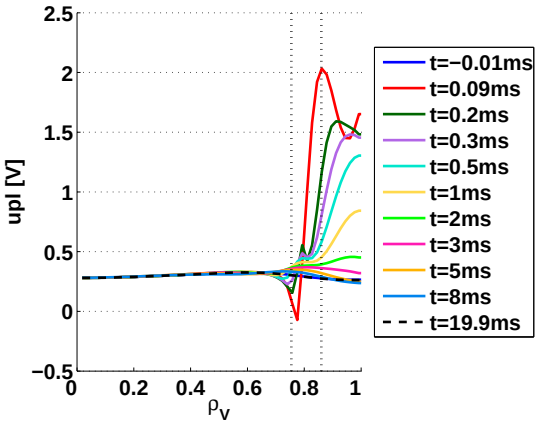

(k)

Figure C.1: Profiles of the main quantities where we have replaced the edge ECH by central one.

C.1.2 Time traces

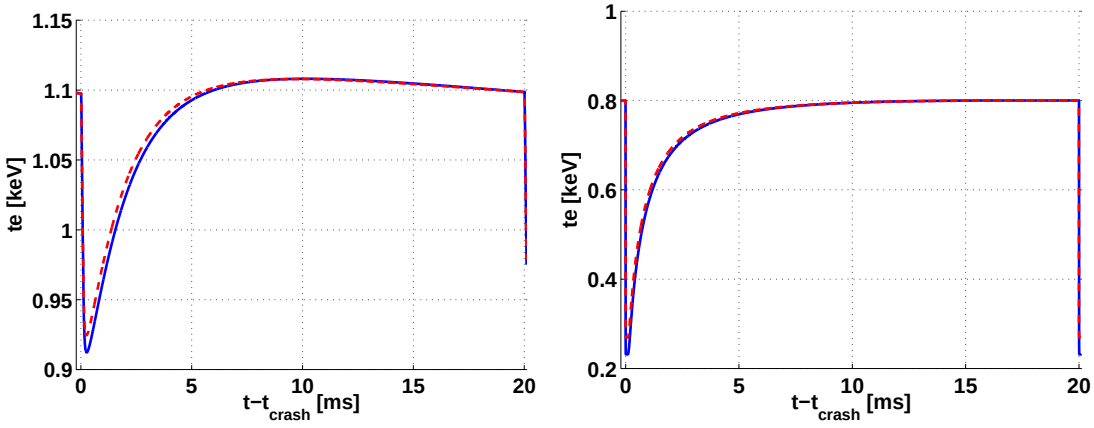

(a) (b)

Figure C.2: Comparison between experimental profile and only central ECH. The solid blue line is the standard case, the dashed red one is the central ECH one. The left figure shows the traces at the top of the density pedestal while the right one is at the maximum of the pressure gradient.

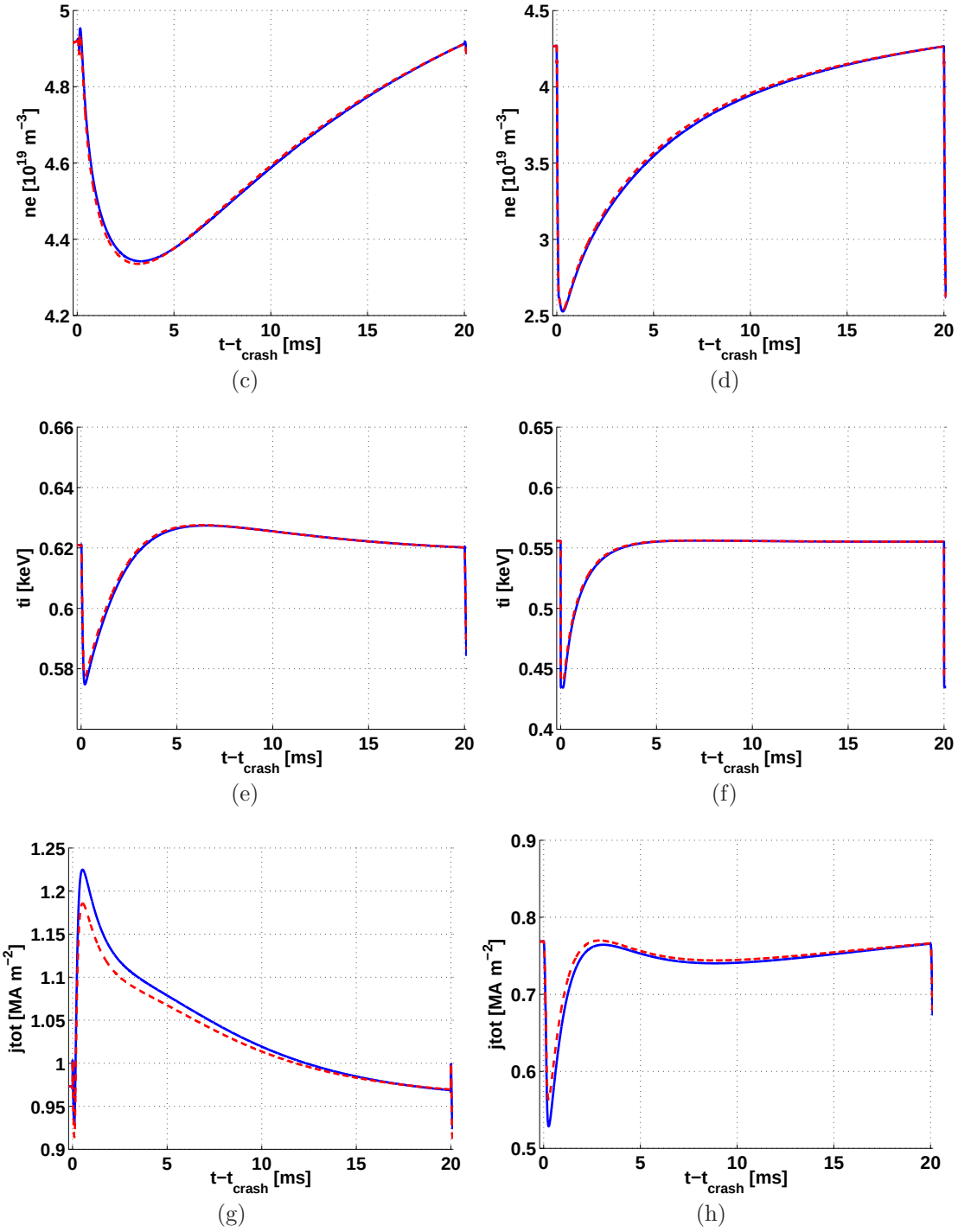

Figure C.2: Comparison between experimental profile and only central ECH. The solid blue line is the standard case, the dashed red one is the central ECH one. The left figures show the traces at the top of the density pedestal while the right ones are at the maximum of the pressure gradient.

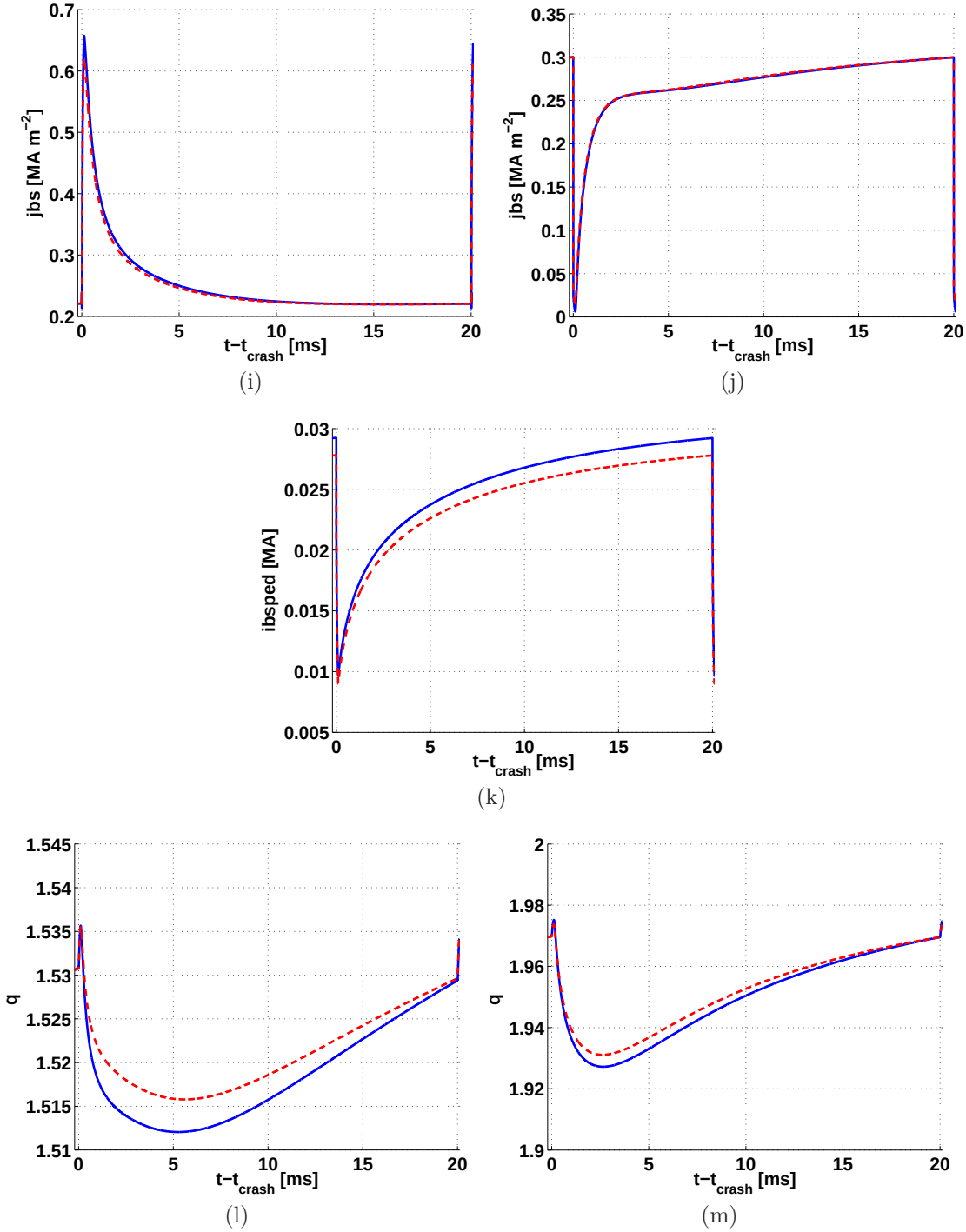

Figure C.2: Comparison between experimental profile and only central ECH. The solid blue line is the standard case, the dashed red one is the central ECH one. The left figures show the traces at the top of the density pedestal while the right ones are at the maximum of the pressure gradient.

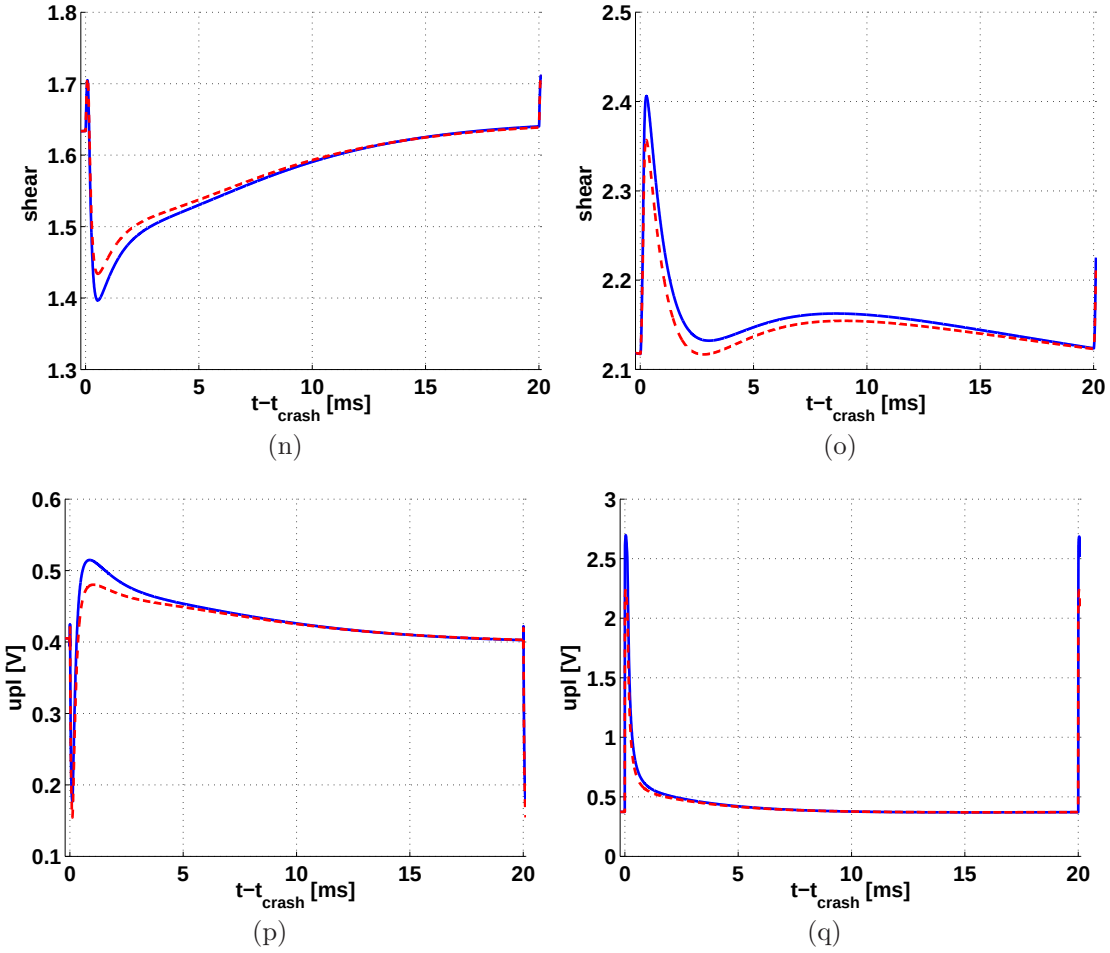

Figure C.2: Comparison between experimental profile and only central ECH. The solid blue line is the standard case, the dashed red one is the central ECH one. The left figures show the traces at the top of the density pedestal while the right ones are at the maximum of the pressure gradient.

C.2 Varying D_n

C.2.1 Profiles

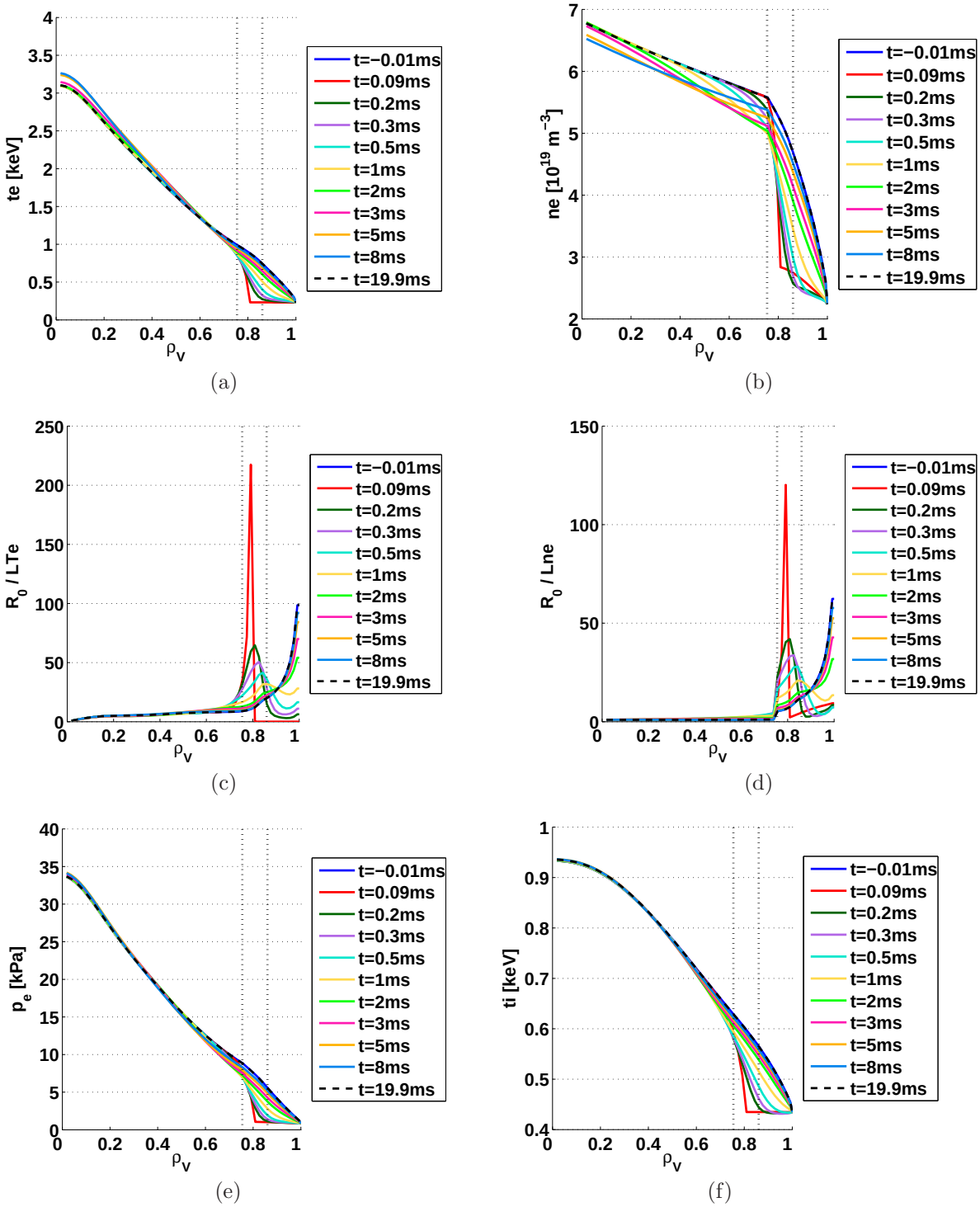

Figure C.3: Profiles of the main quantities for an inter-ELM with particle diffusivity multiplied by ten.

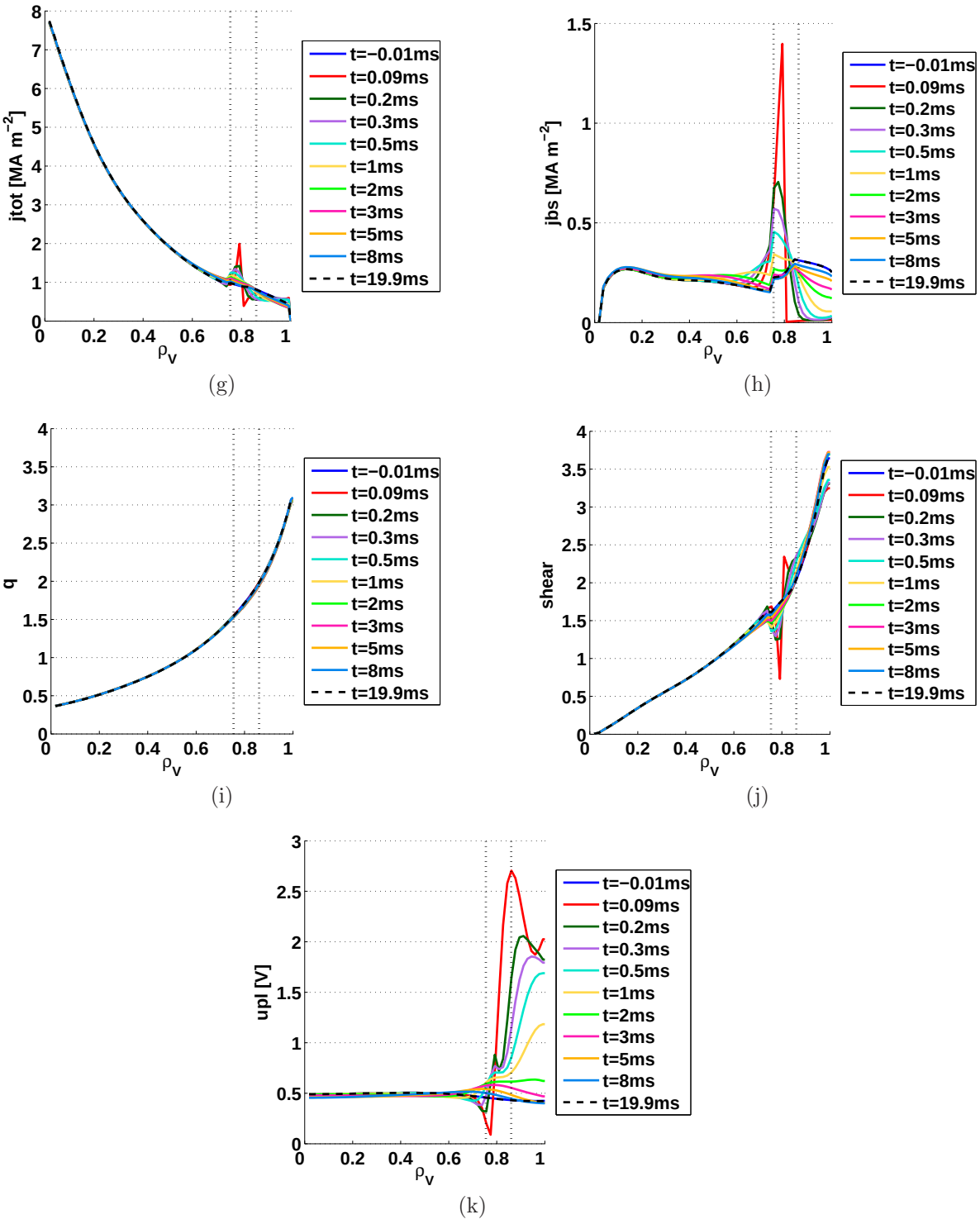

(g) (h) (i) (j) (k)

Figure C.3: Profiles of the main quantities for an inter-ELM with particle diffusivity multiplied by ten.

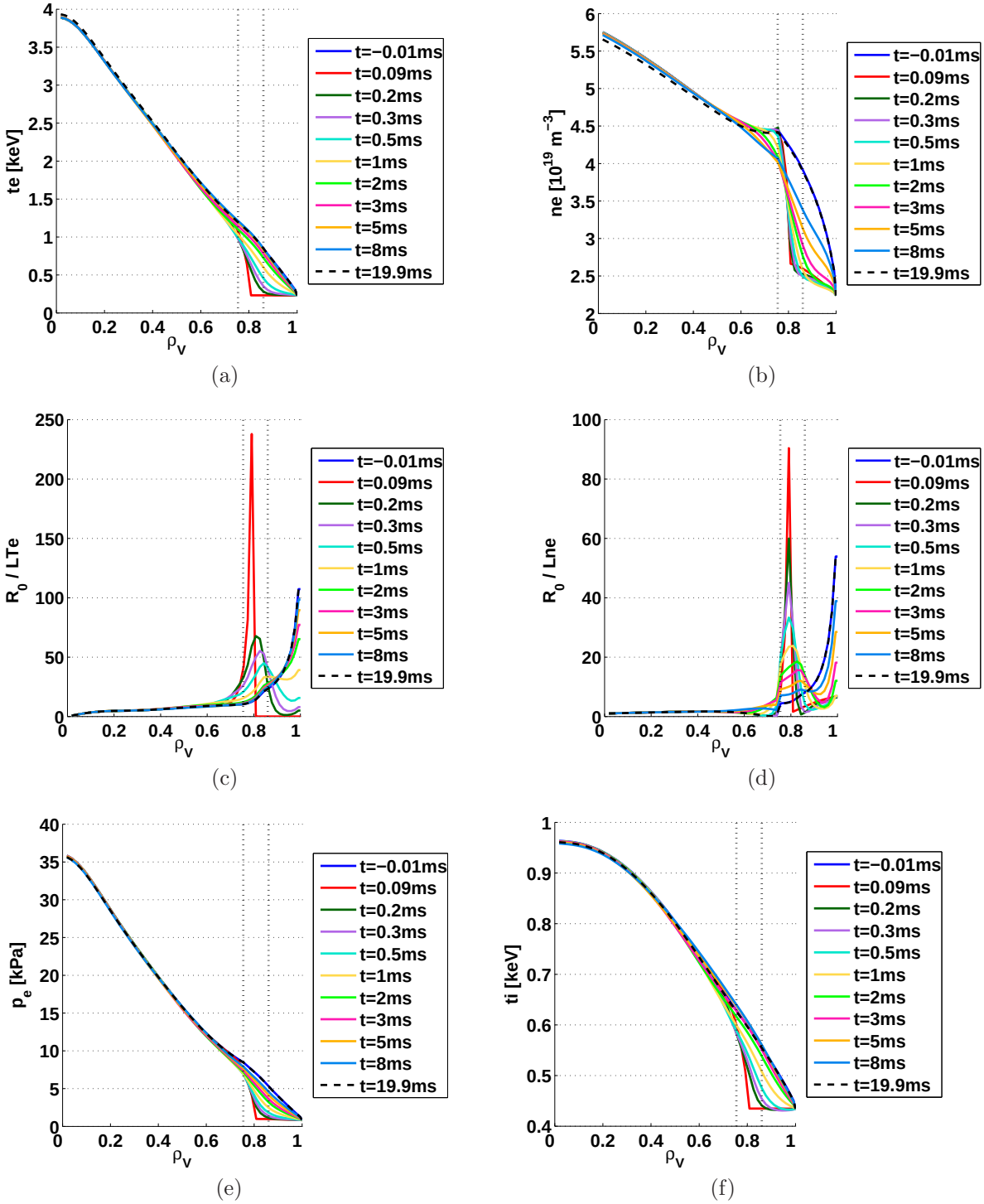

Figure C.4: Profiles of the main quantities for an inter-ELM with particle diffusivity divided by two.

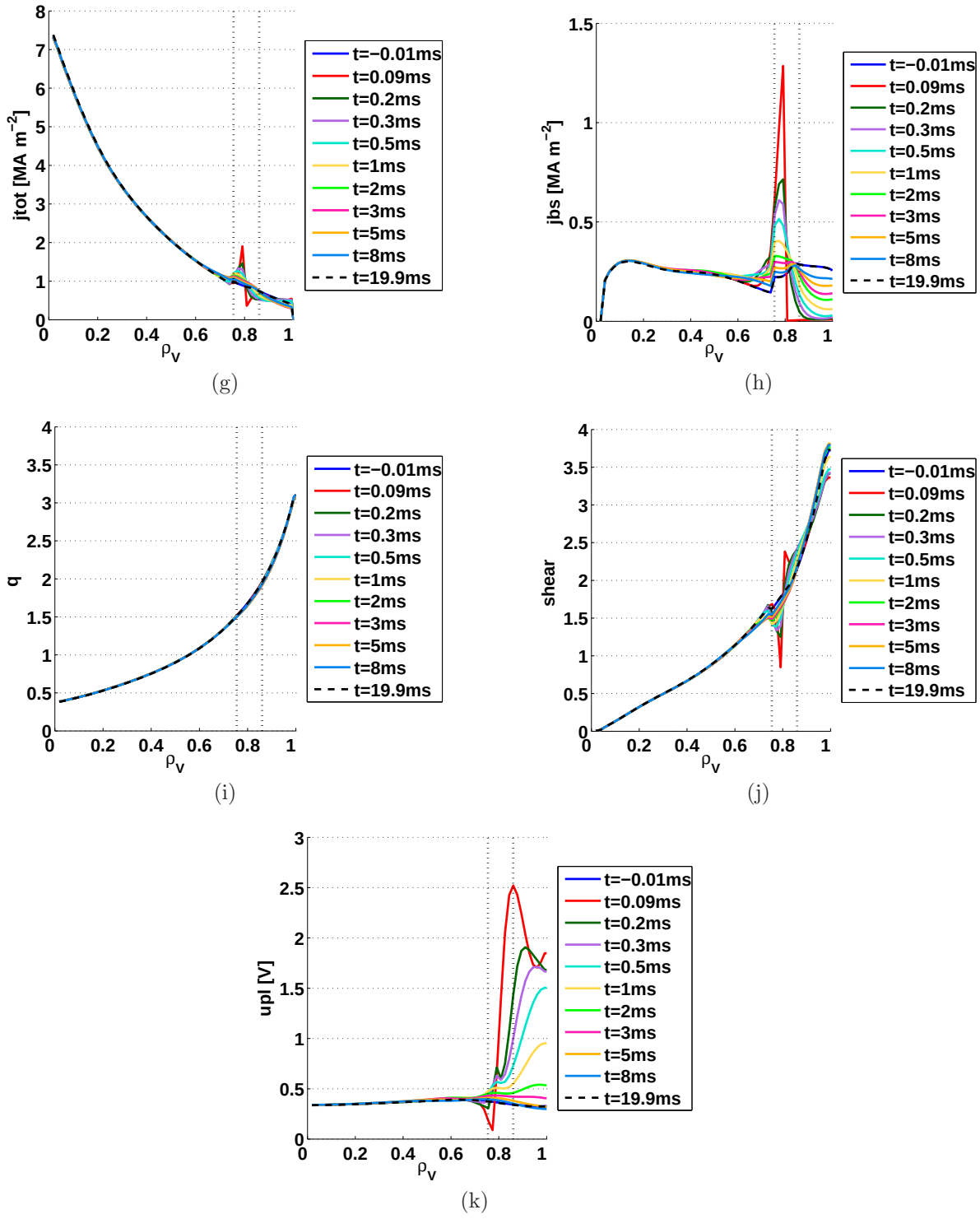

(g) (h) (i) (j) (k)

Figure C.4: Profiles of the main quantities for an inter-ELM with particle diffusivity divided by two.

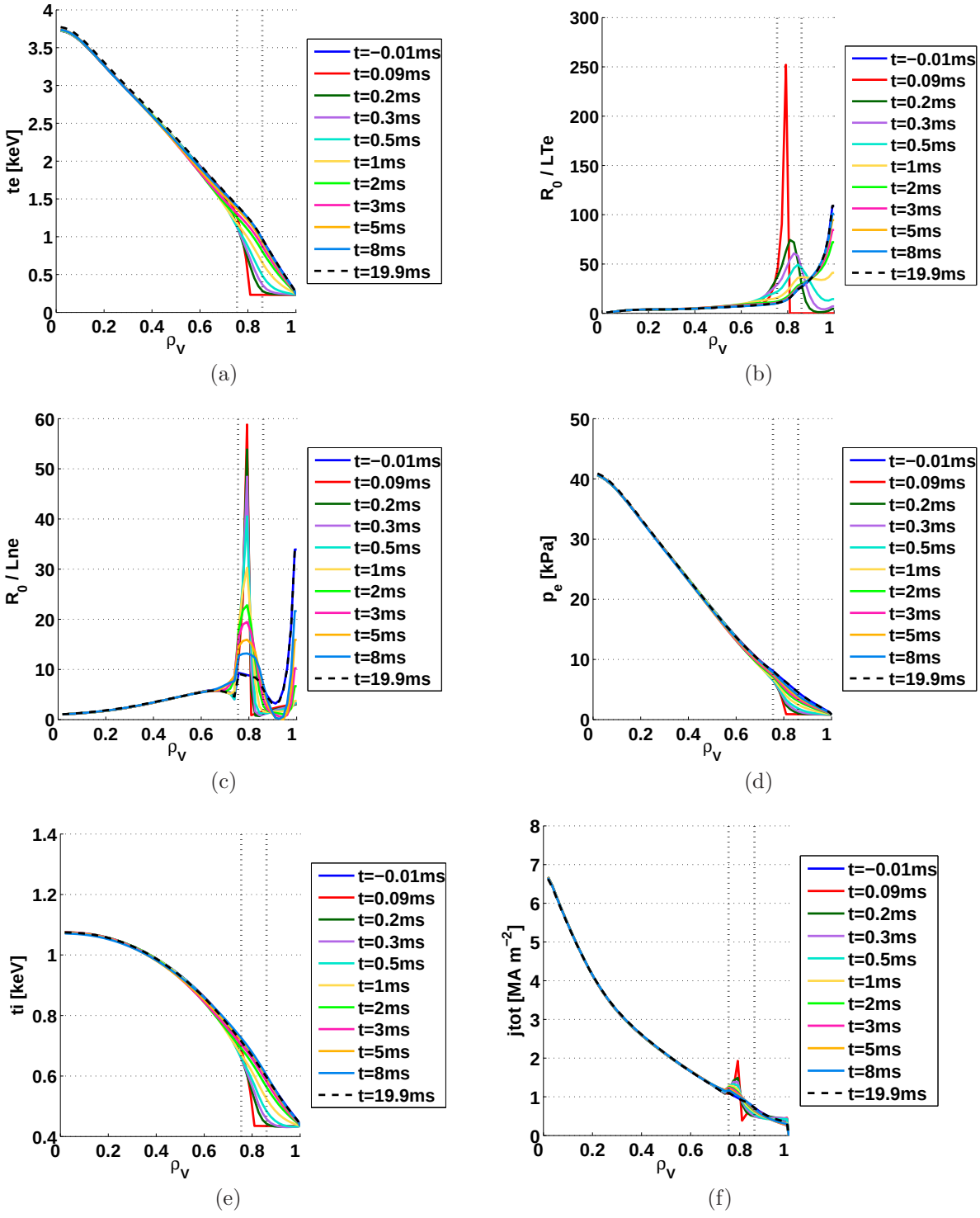

Figure C.5: Profiles of the main quantities for an inter-ELM with particle diffusivity divided by ten.

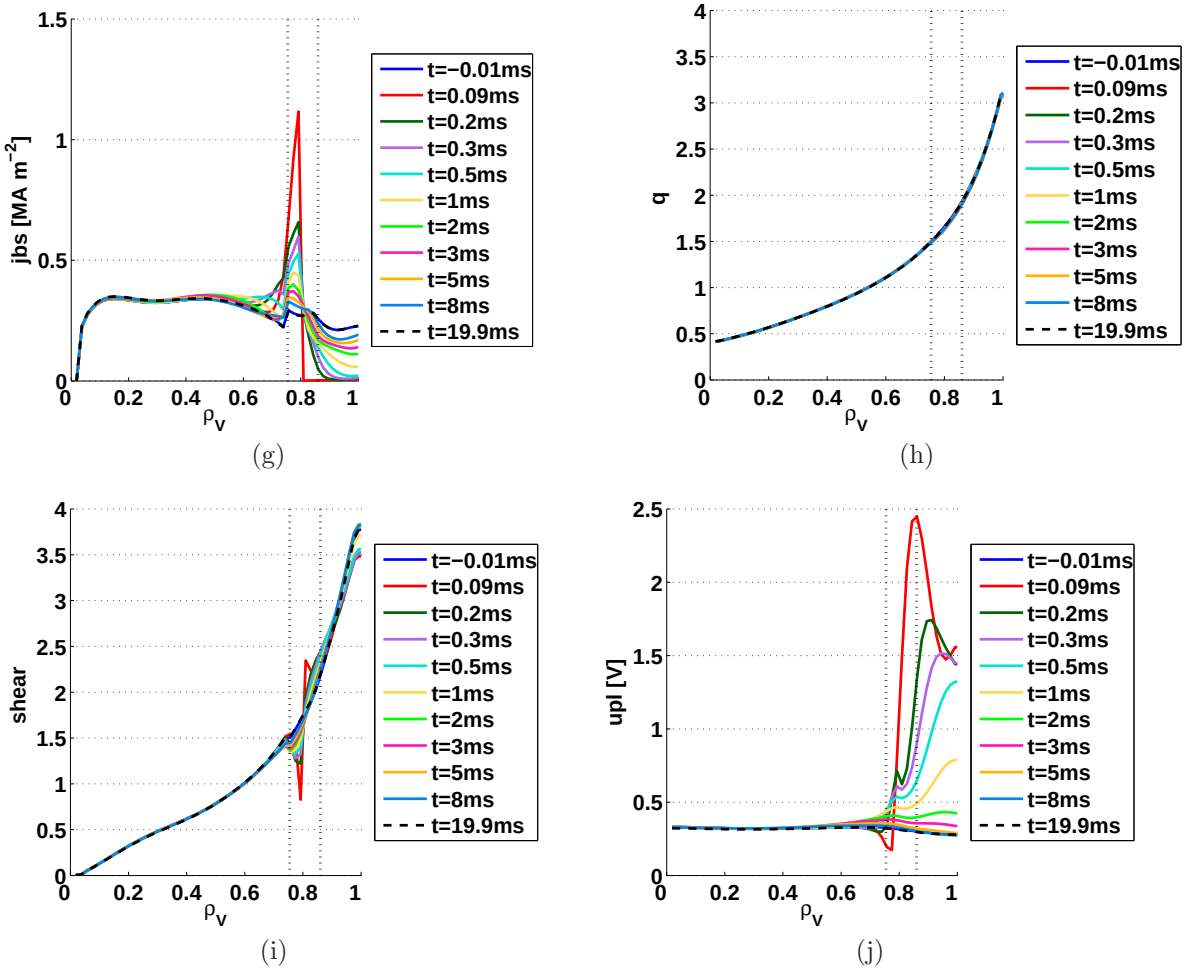

Figure C.5: Profiles of the main quantities for an inter-ELM with particle diffusivity divided by ten.

C.2.2 Time traces

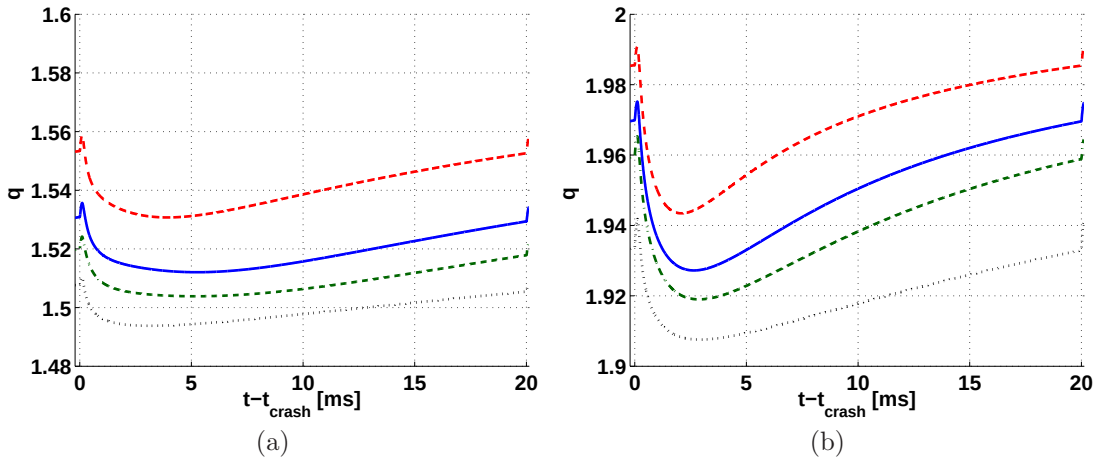

Figure C.6: Comparison between different values for Dn. The solid blue line is the reference case, the dashed red one is the "Dn10" case, the dash-dotted dark green is "Dn05" and the dotted black is "Dn01". The left figure shows the traces at the top of the density pedestal while the right one is at the maximum of the pressure gradient.

C.2.3 MHD diagrams

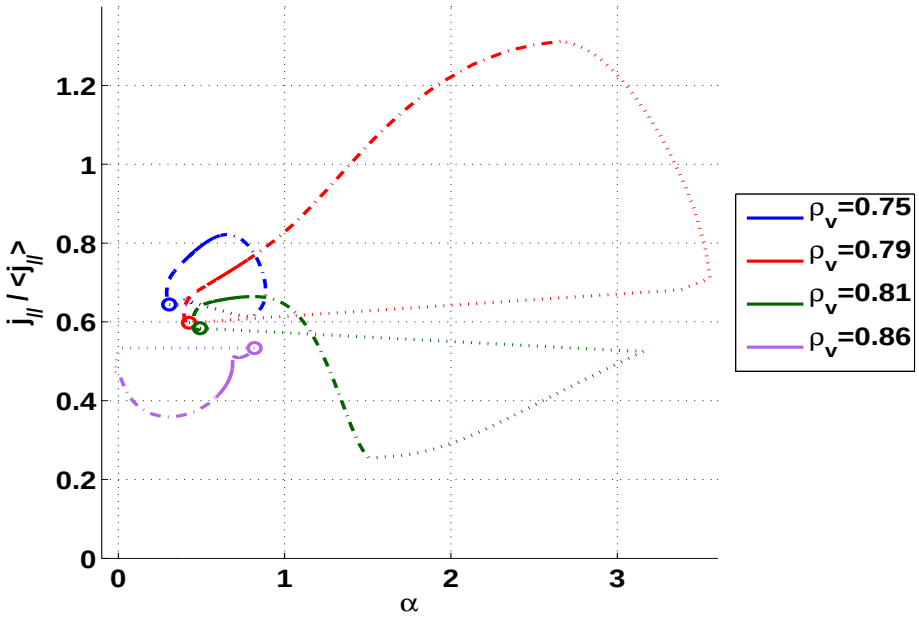

Figure C.7: $j - \alpha$ diagram for the "Dn10" ELM cycle. Dotted lines are during the ELM crash $0 \leq t < 0.1$, dash-dotted is for $0.1 \leq t < 0.5$, solid lines are $0.5 \leq t < 1$ and dashed lines are from 1 to the next ELM (20) with the time in ms. $\rho_V = 0.75$ is the top of the density pedestal, $\rho_V = 0.79$ is where this diagram is the largest, $\rho_V = 0.81$ is the top of the temperature pedestal and $\rho_V = 0.86$ is the maximum of the pressure gradient.

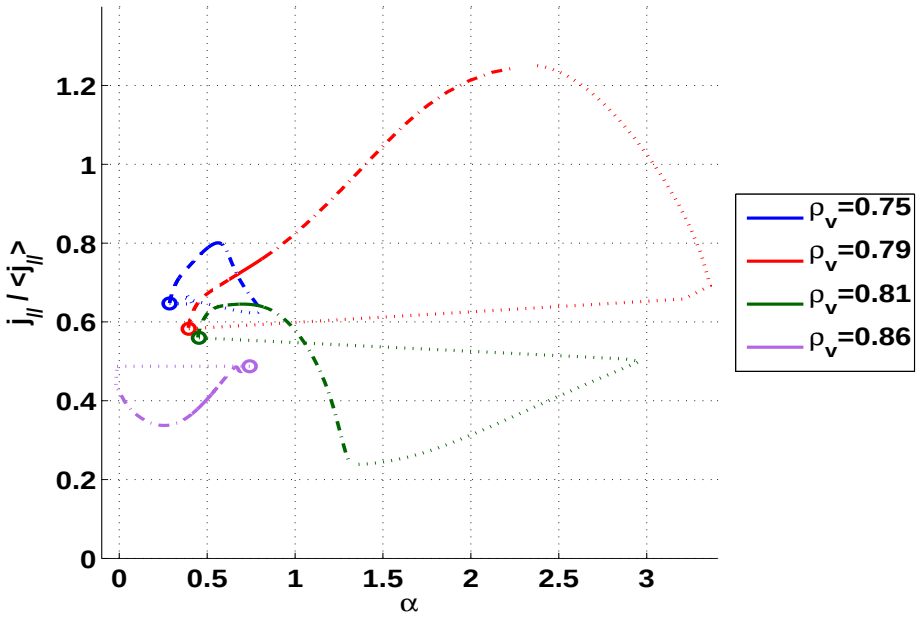

Figure C.8: $j - \alpha$ diagram for the "Dn05" ELM cycle. Dotted lines are during the ELM crash $0 \leq t < 0.1$, dash-dotted is for $0.1 \leq t < 0.5$, solid lines are $0.5 \leq t < 1$ and dashed lines are from 1 to the next ELM (20) with the time in ms. $\rho_V = 0.75$ is the top of the density pedestal, $\rho_V = 0.79$ is where this diagram is the largest, $\rho_V = 0.81$ is the top of the temperature pedestal and $\rho_V = 0.86$ is the maximum of the pressure gradient.

C.3 First vs non-first

C.3.1 Reference case

Profiles

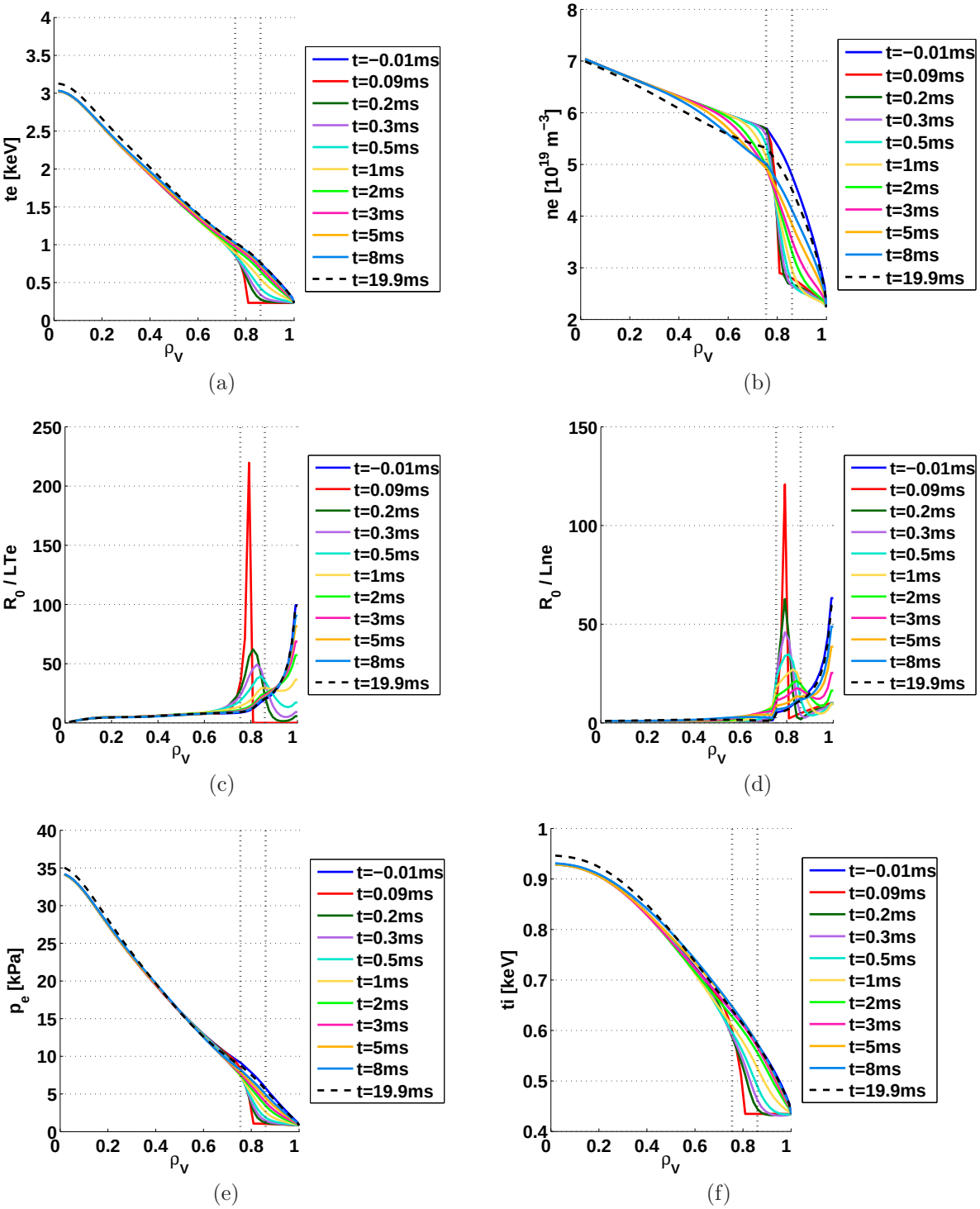

Figure C.9: Profiles of the main quantities for an inter-ELM in the reference case for the first ELM.

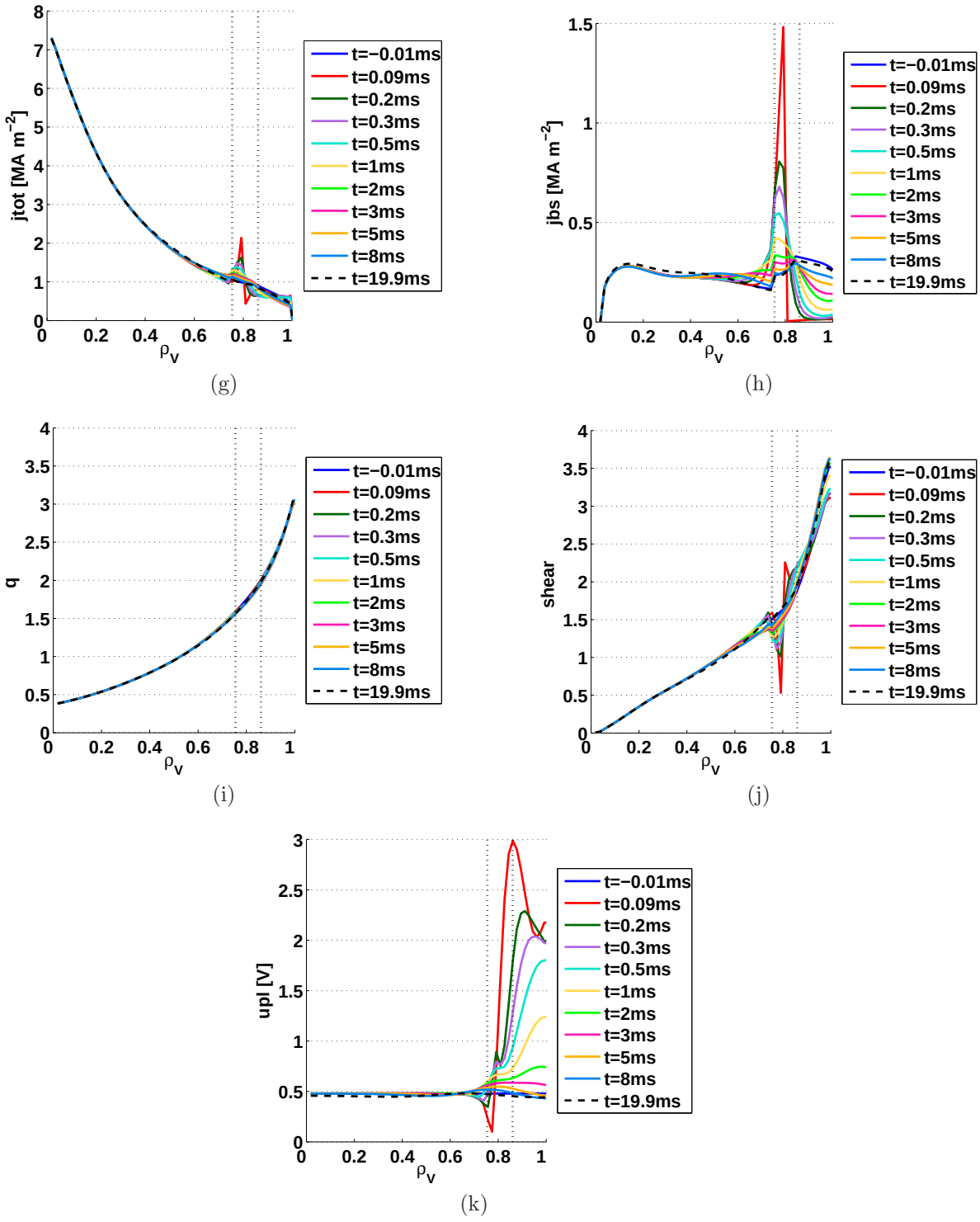

Figure C.9: Profiles of the main quantities for an inter-ELM in the reference case for the first ELM.

Time traces

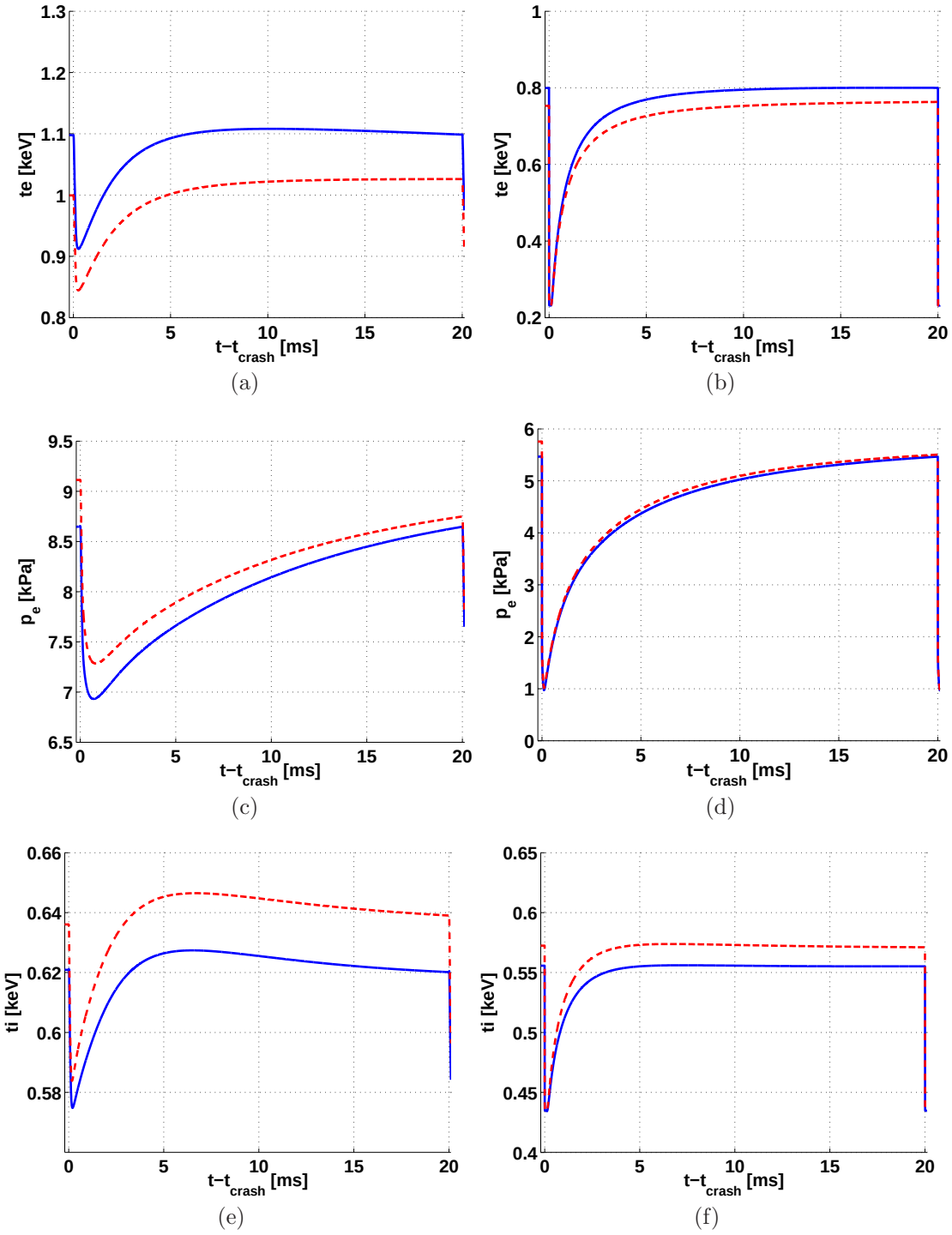

Figure C.10: Comparison between first and non-first ELM. The solid blue line is the non-first from the standard case while the dashed red one is the first. The left figures show the traces at the top of the density pedestal while the right ones are at the maximum of the pressure gradient.

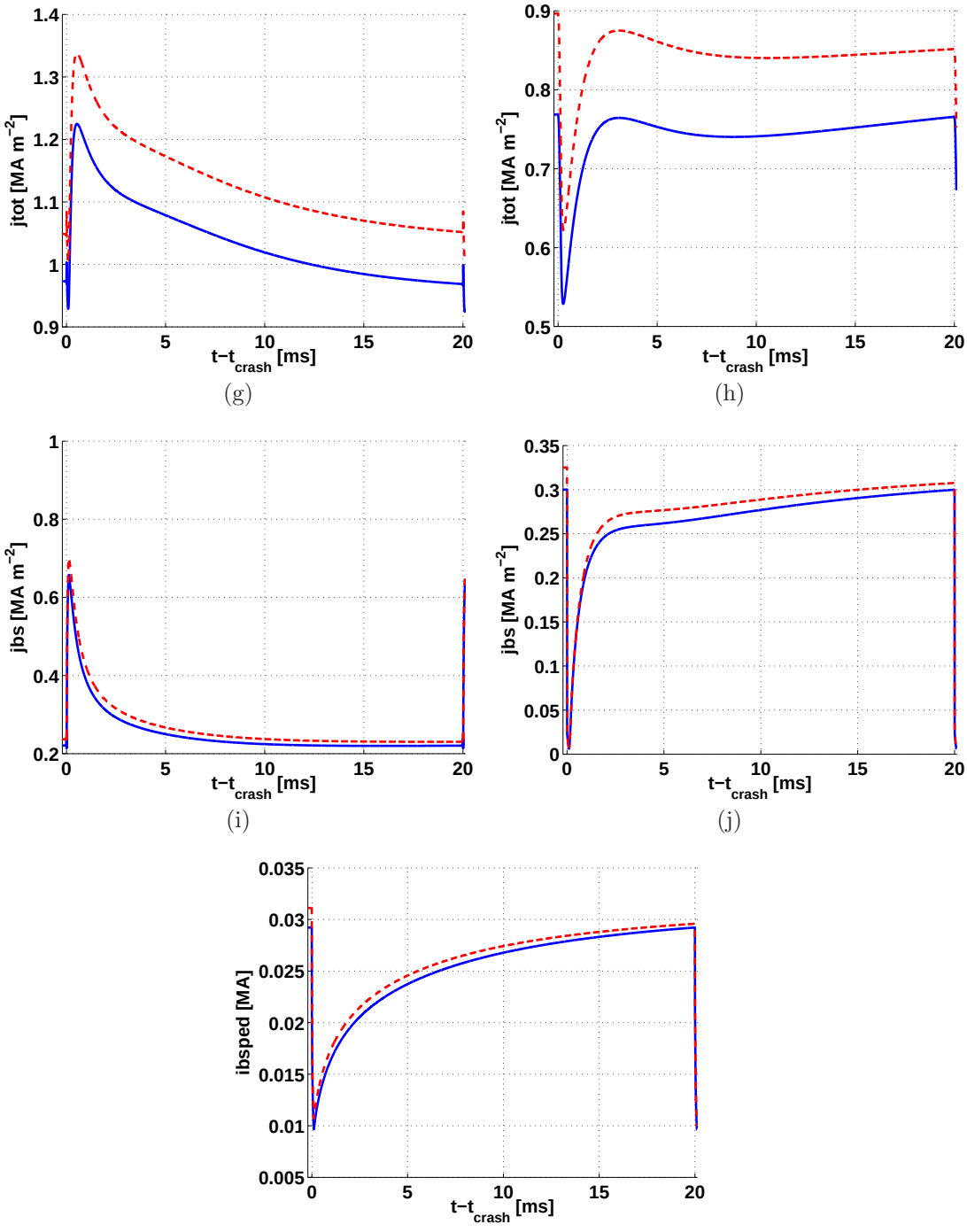

Figure C.10: Comparison between first and non-first ELM. The solid blue line is the non-first from the standard case while the dashed red one is the first. The left figures show the traces at the top of the density pedestal while the right ones are at the maximum of the pressure gradient.

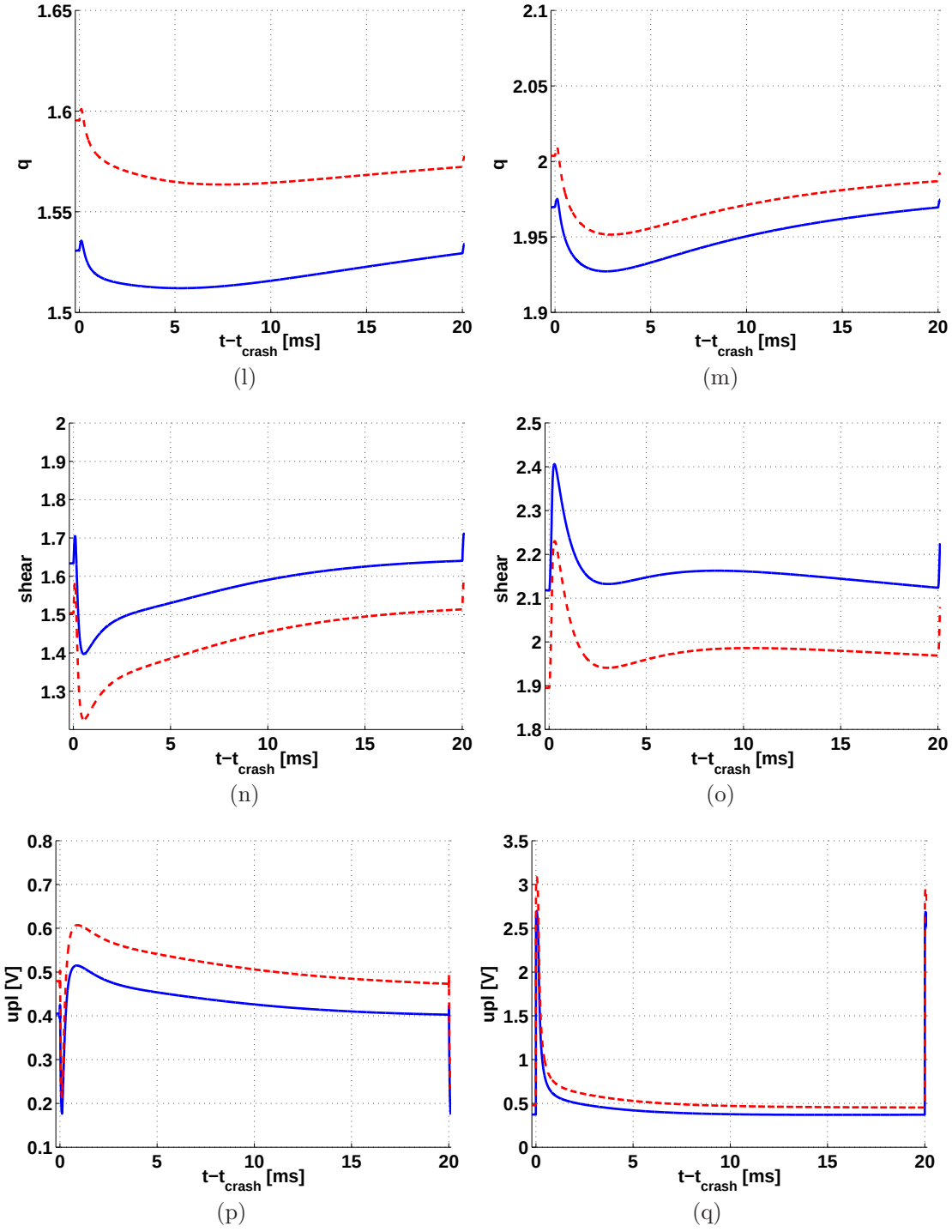

Figure C.10: Comparison between first and non-first ELM. The solid blue line is the non-first from the standard case while the dashed red one is the first. The left figures show the traces at the top of the density pedestal while the right ones are at the maximum of the pressure gradient.

C.3.2 Particle diffusivity multiplied by ten

Profiles

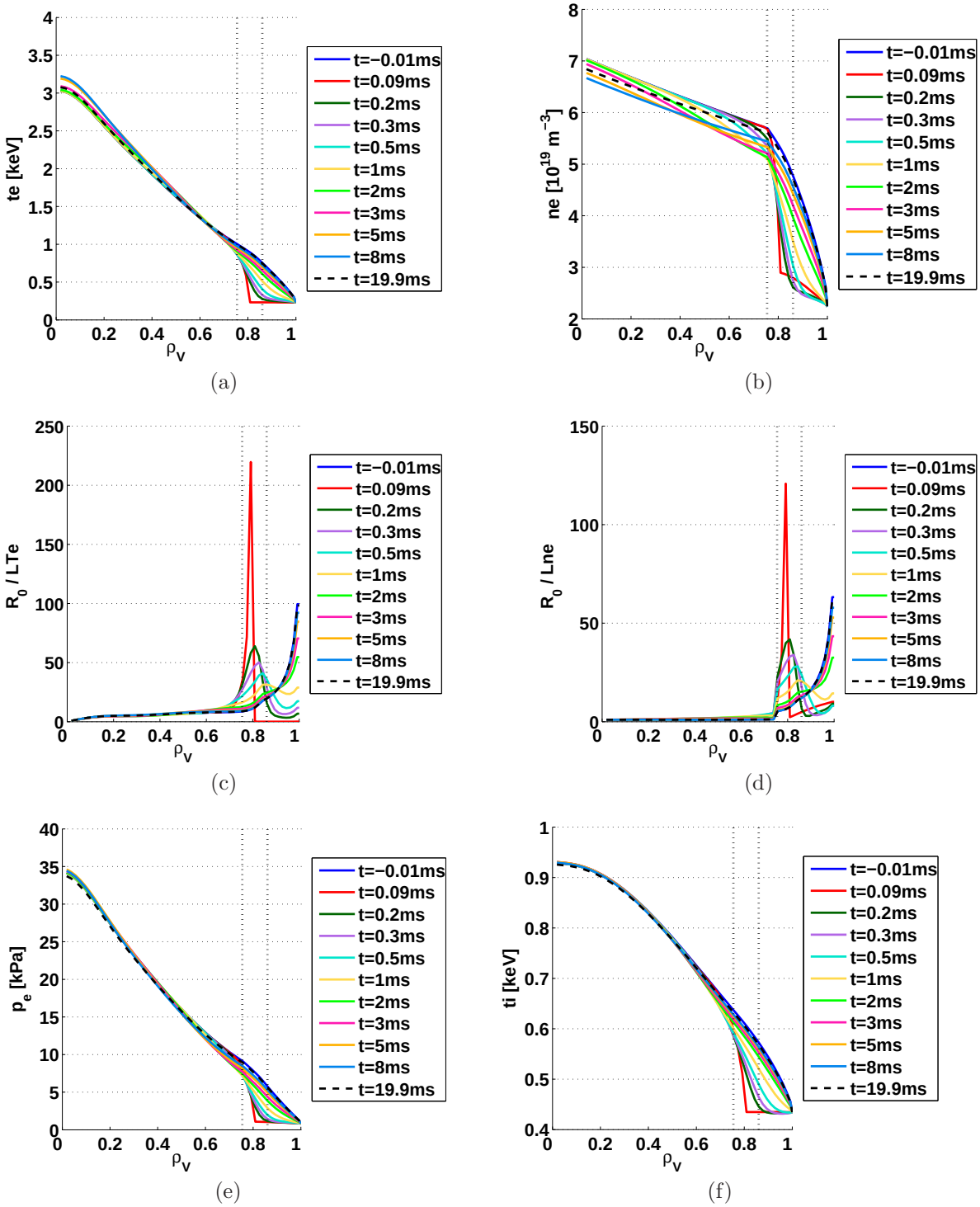

Figure C.11: Profiles of the main quantities for an inter-ELM for the case "Dn10" for the first ELM.

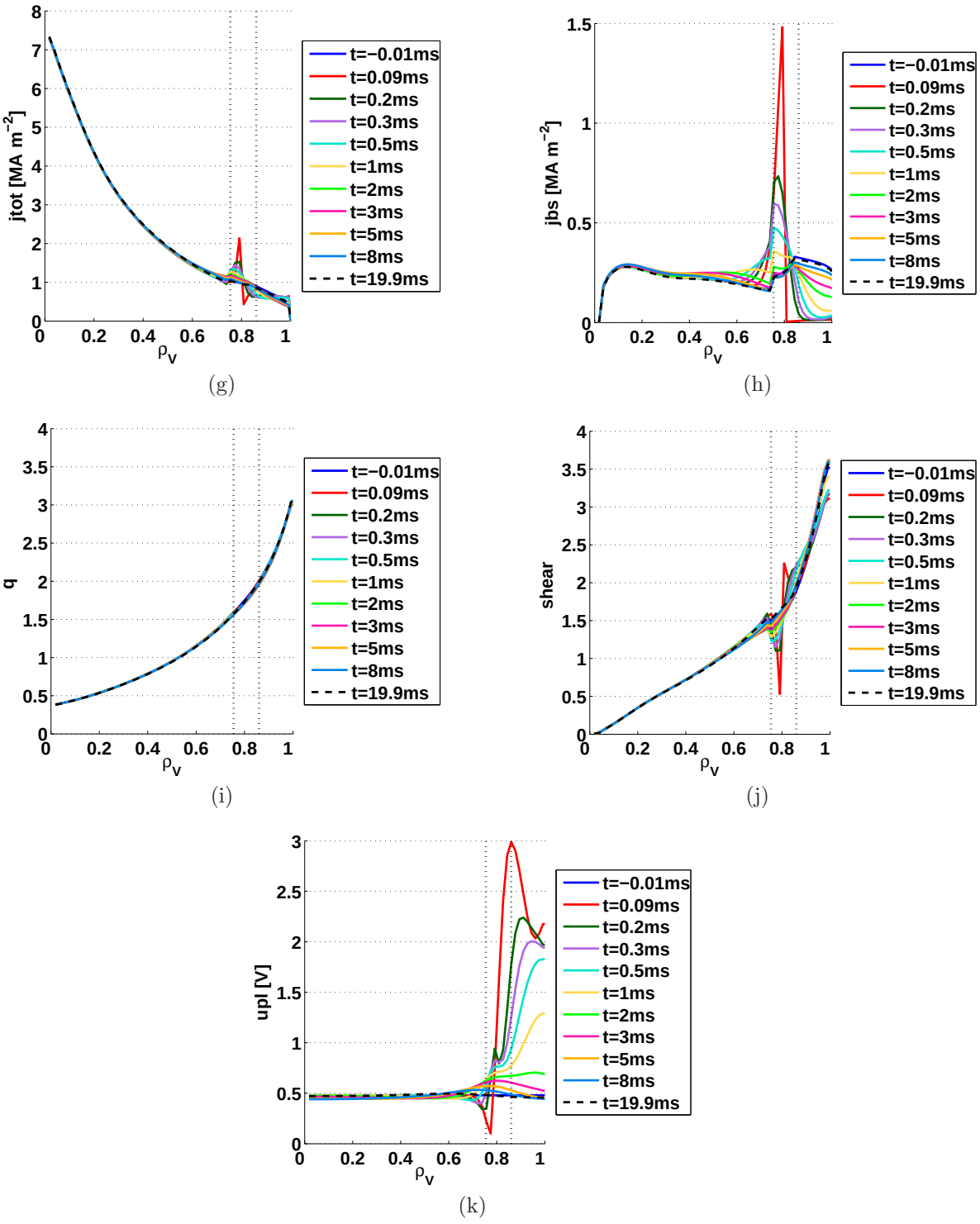

(g) (h) (i) (j) (k)

Figure C.11: Profiles of the main quantities for an inter-ELM for the case "Dn10" for the first ELM.

Time traces

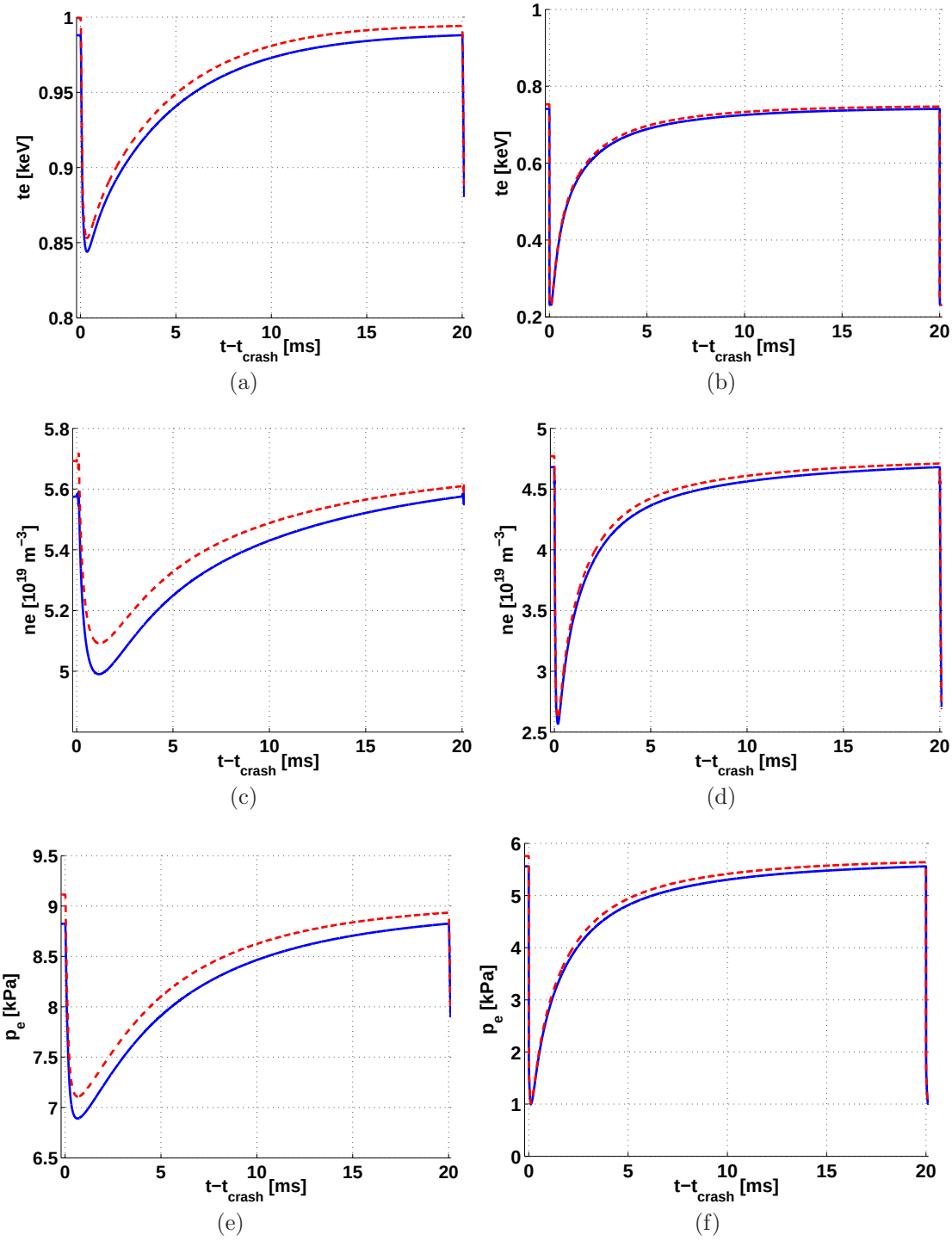

Figure C.12: Comparison between first and non-first ELM. The solid blue line is the non-first from case "Dn10" while the dashed red one is the first. The left figures show the traces at the top of the density pedestal while the right ones are at the maximum of the pressure gradient.

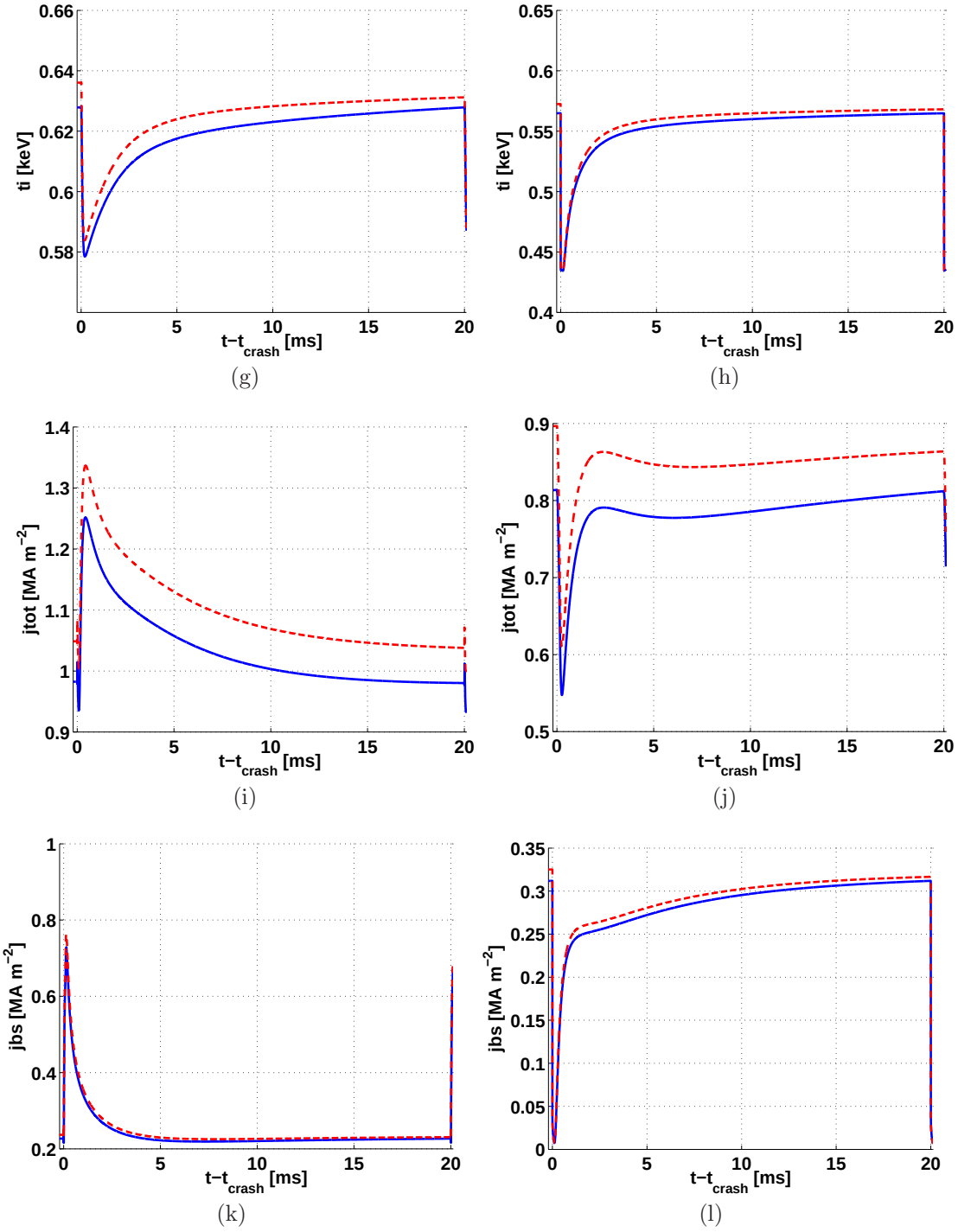

Figure C.12: Comparison between first and non-first ELM. The solid blue line is the non-first from case "Dn10" while the dashed red one is the first. The left figures show the traces at the top of the density pedestal while the right ones are at the maximum of the pressure gradient.

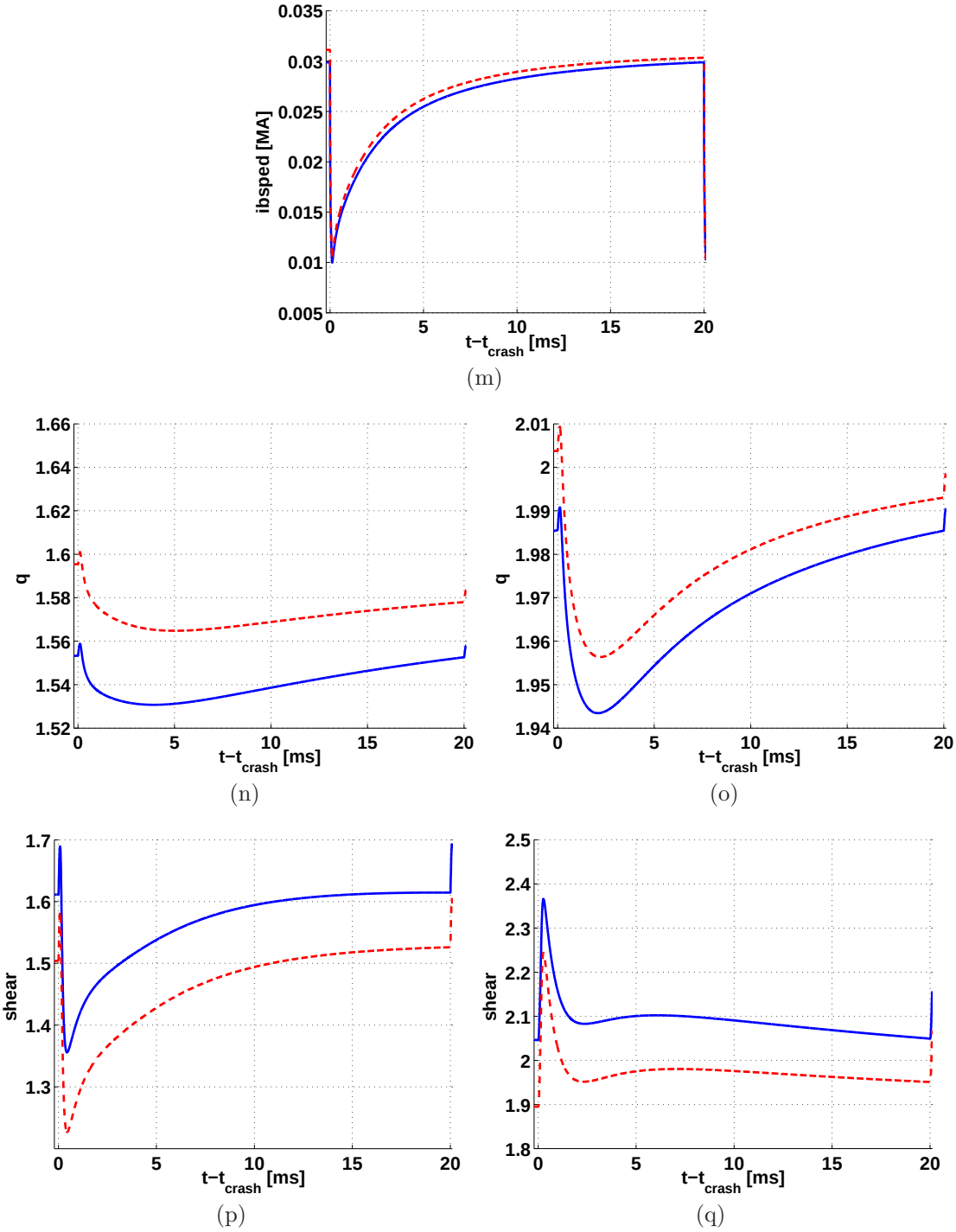

(m) (n) (o) (p) (q)

Figure C.12: Comparison between first and non-first ELM. The solid blue line is the non-first from case "Dn10" while the dashed red one is the first. The left figures show the traces at the top of the density pedestal while the right ones are at the maximum of the pressure gradient.

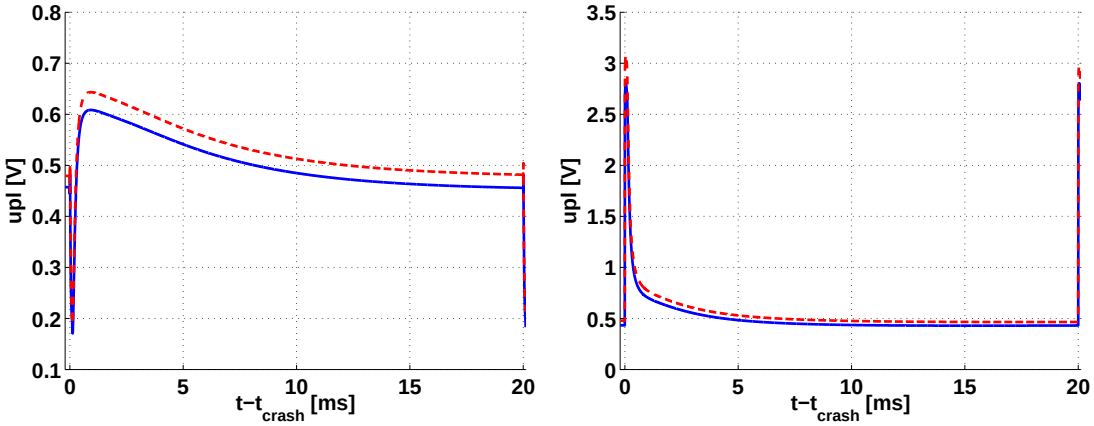

(r) (s)

Figure C.12: Comparison between first and non-first ELM. The solid blue line is the non-first from case "Dn10" while the dashed red one is the first. The left figure shows the traces at the top of the density pedestal while the right one is at the maximum of the pressure gradient.

MHD diagram

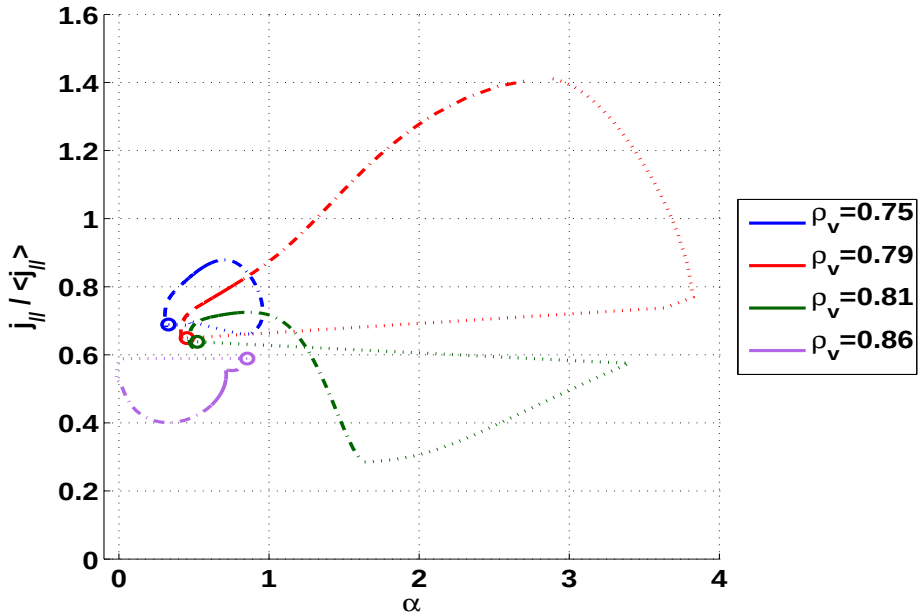

Figure C.13: $j - \alpha$ diagram for the first ELM cycle of the "Dn10" case. Dotted lines are during the ELM crash $0 \leq t < 0.1$, dash-dotted is for $0.1 \leq t < 0.5$, solid lines are $0.5 \leq t < 1$ and dashed lines are from 1 to the next ELM (20) with the time in ms. $\rho_V = 0.75$ is the top of the density pedestal, $\rho_V = 0.79$ is where this diagram is the largest, $\rho_V = 0.81$ is the top of the temperature pedestal and $\rho_V = 0.86$ is the maximum of the pressure gradient.

C.3.3 Particle diffusivity divided by two

Profiles

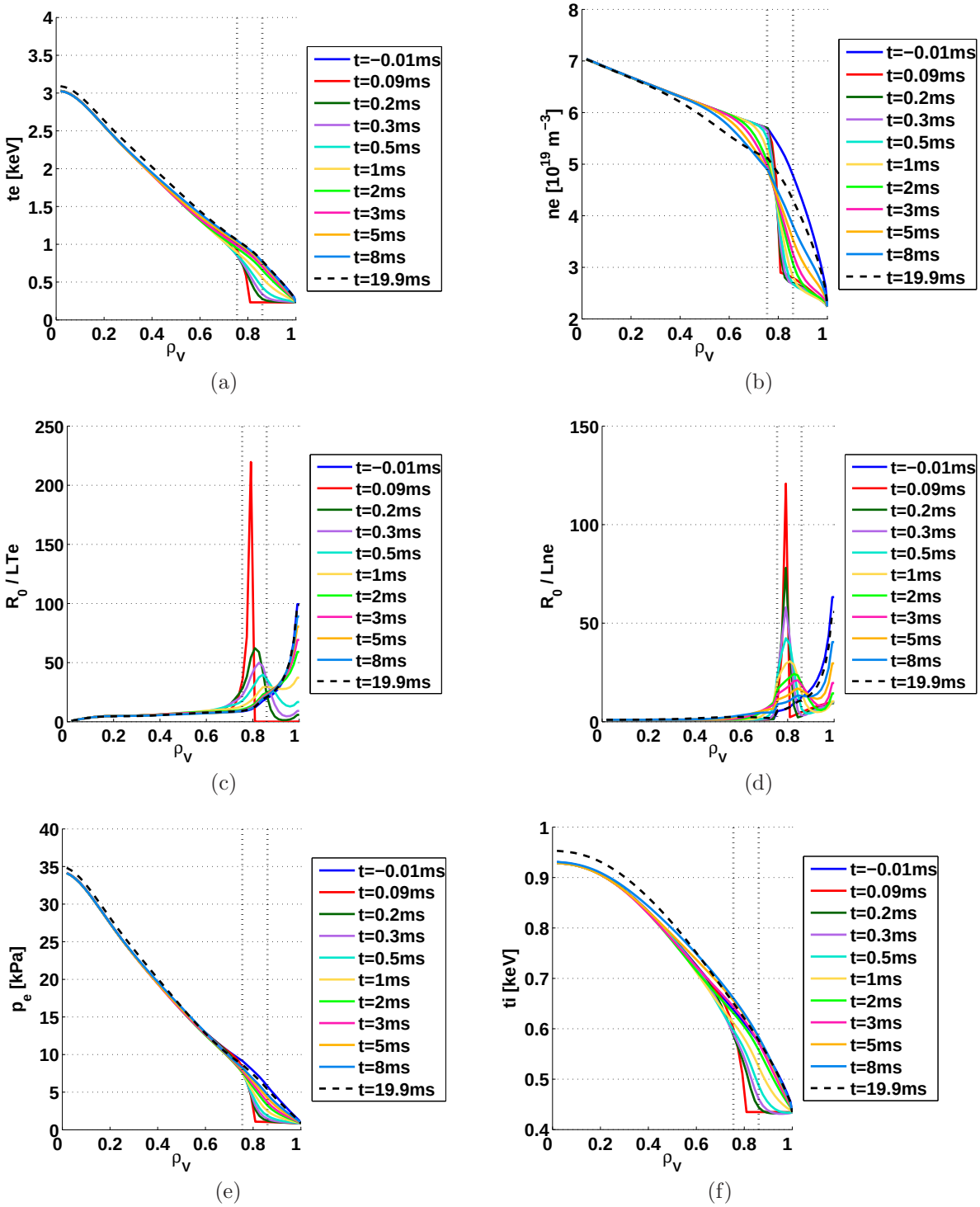

Figure C.14: Profiles of the main quantities for an inter-ELM for the case "Dn05" for the first ELM.

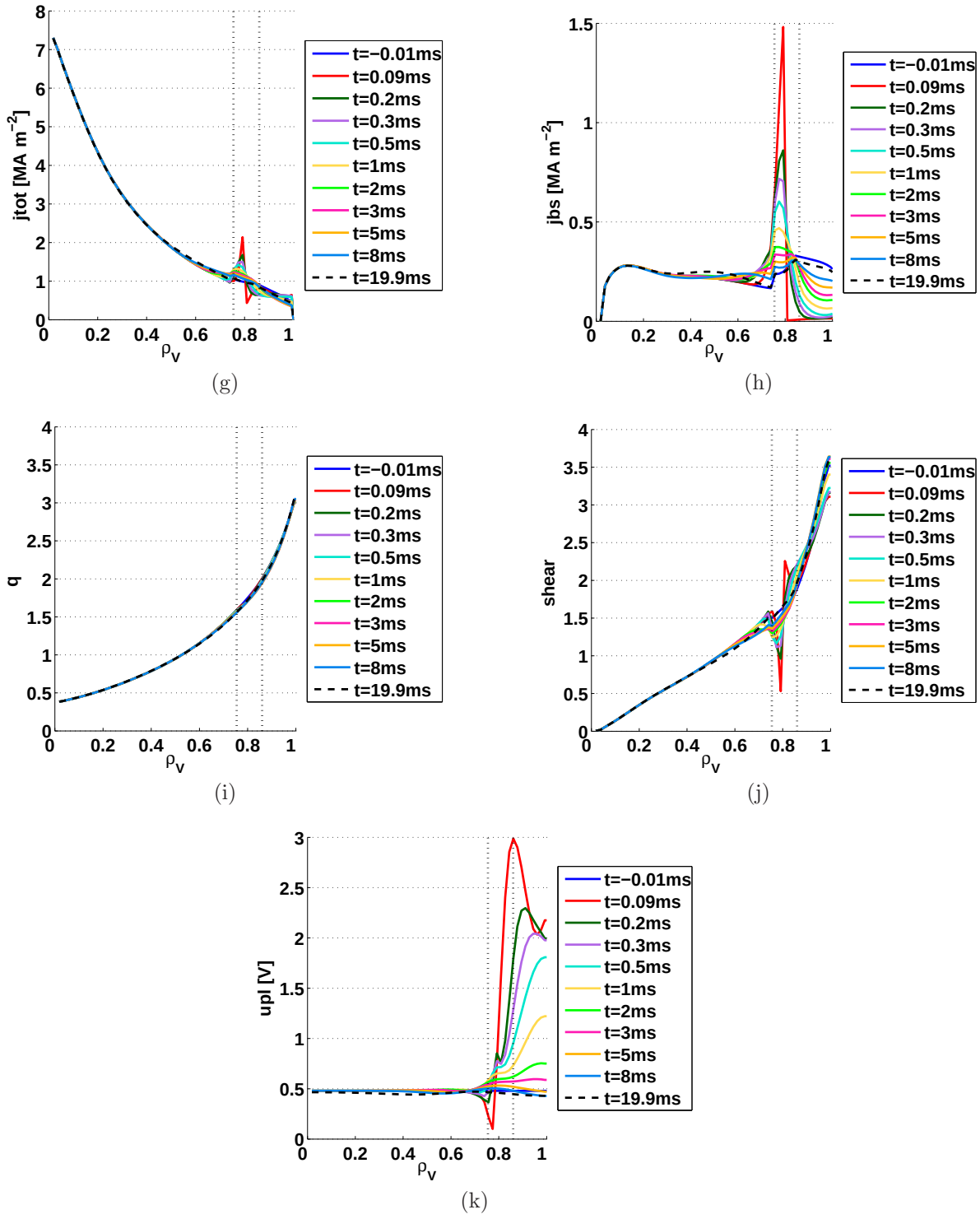

(g) (h) (i) (j) (k)

Figure C.14: Profiles of the main quantities for an inter-ELM for the case "Dn05" for the first ELM.

Time traces

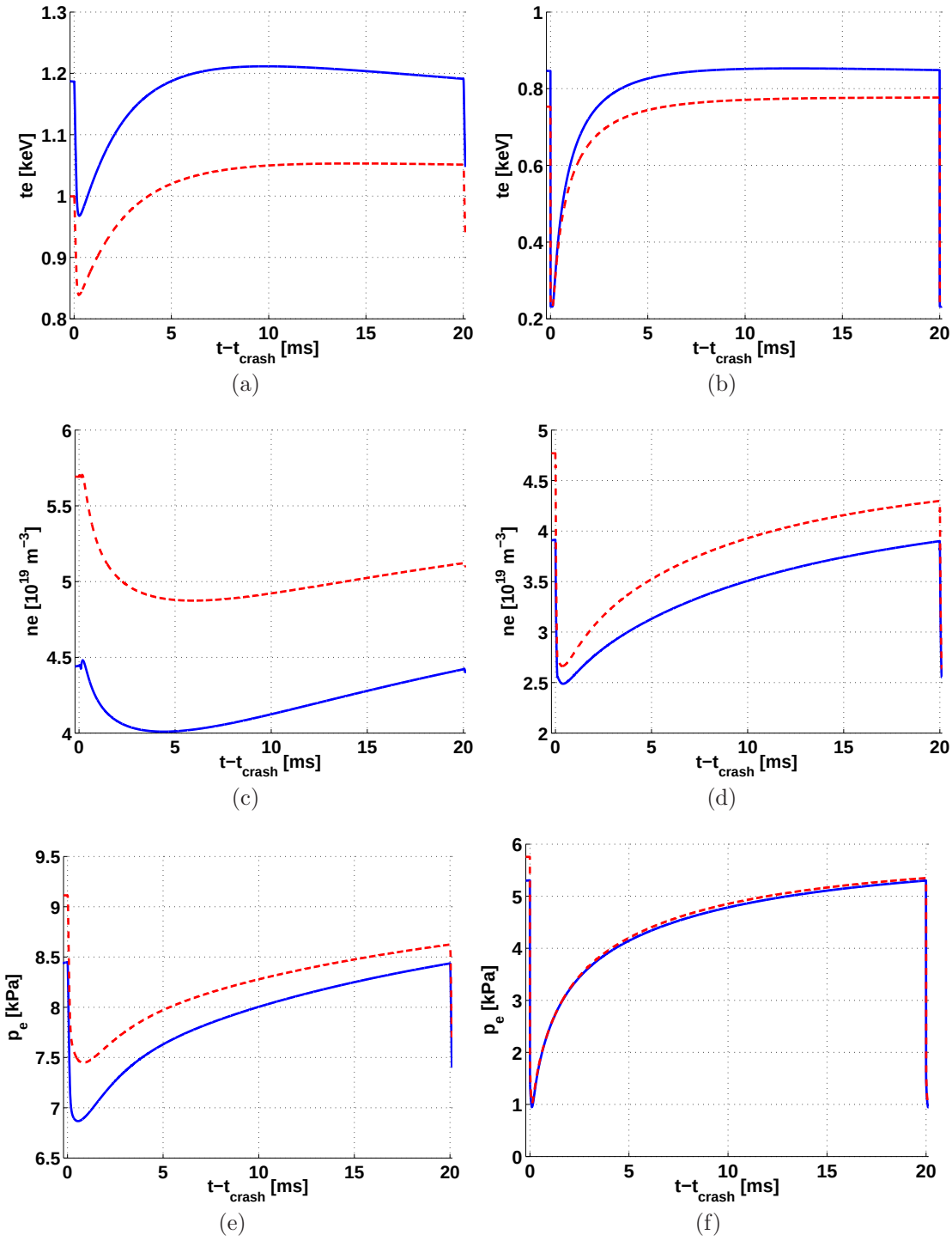

Figure C.15: Comparison between first and non-first ELM. The solid blue line is the non-first from the half-diffusivity case while the dashed red one is the first. The left figures show the traces at the top of the density pedestal while the right ones are at the maximum of the pressure gradient.

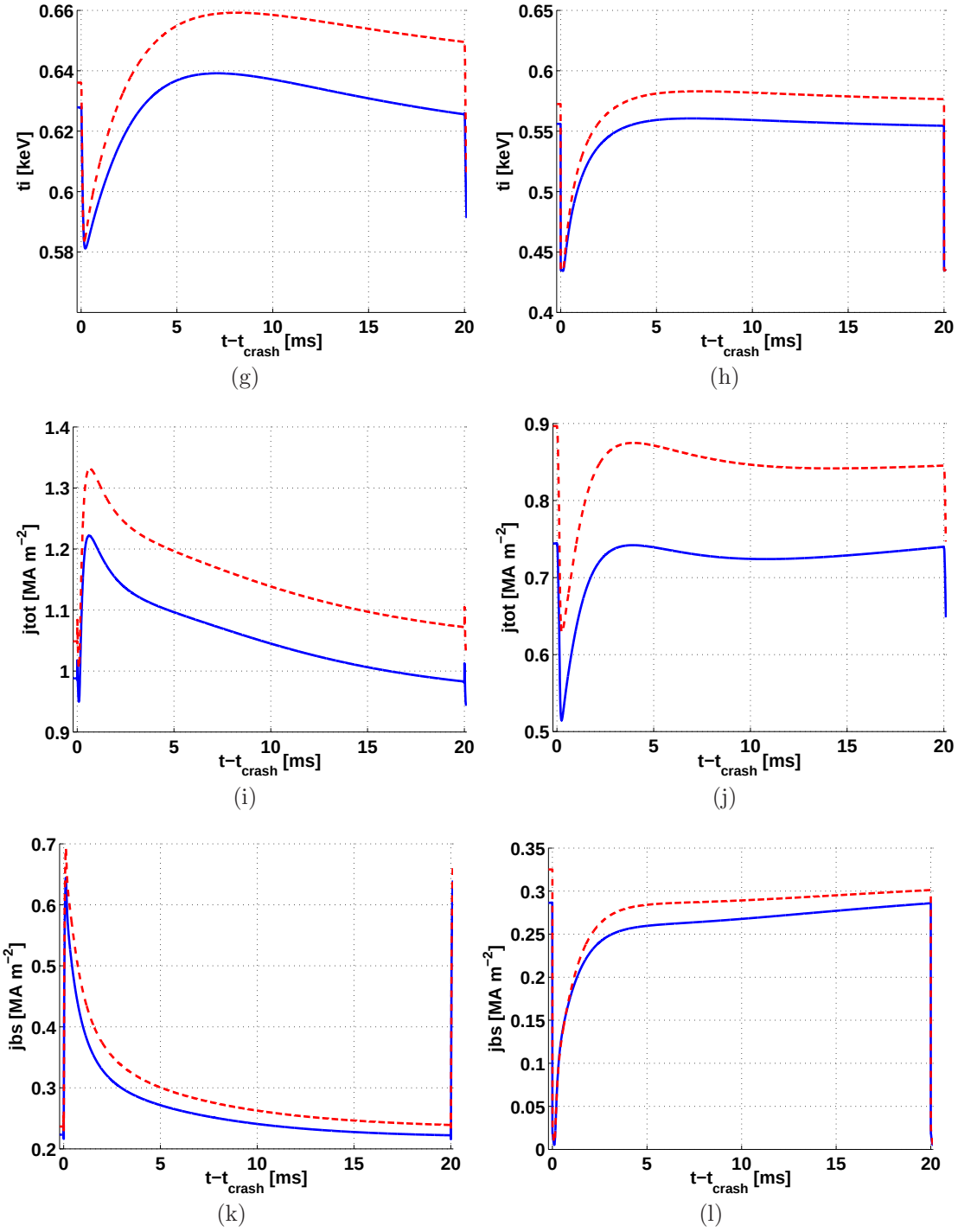

Figure C.15: Comparison between first and non-first ELM. The solid blue line is the non-first from the half-diffusivity case while the dashed red one is the first. The left figures show the traces at the top of the density pedestal while the right ones are at the maximum of the pressure gradient.

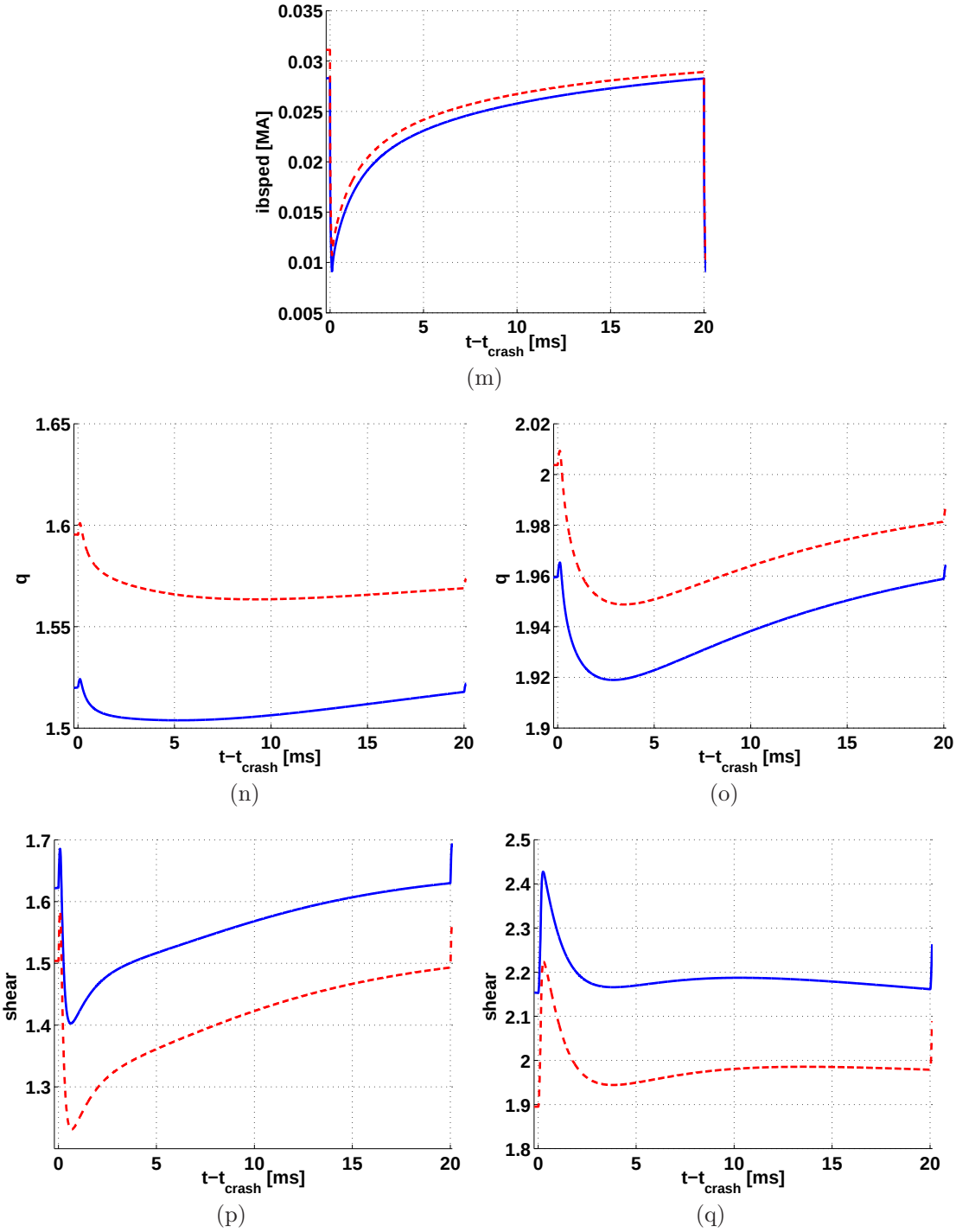

(m) (n) (o) (p) (q)

Figure C.15: Comparison between first and non-first ELM. The solid blue line is the non-first from the half-diffusivity case while the dashed red one is the first. The left figures show the traces at the top of the density pedestal while the right ones are at the maximum of the pressure gradient.

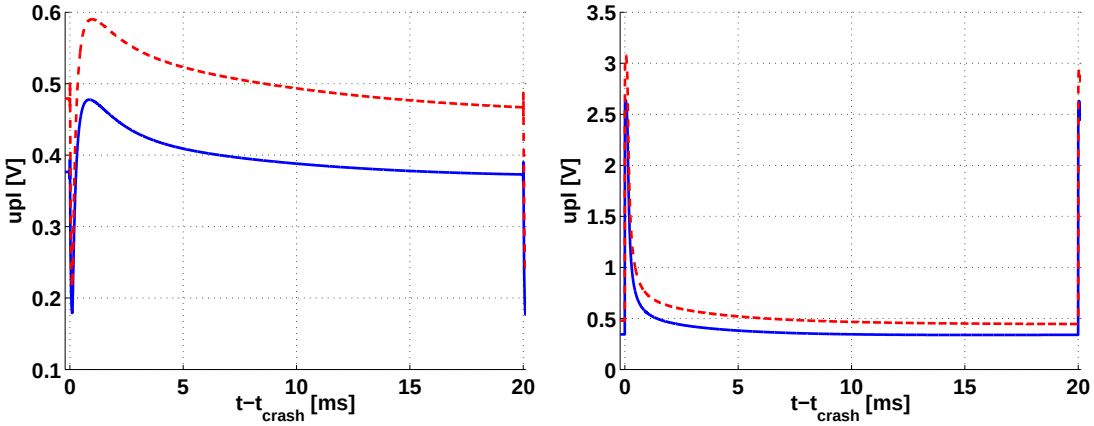

(r) (s)

Figure C.15: Comparison between first and non-first ELM. The solid blue line is the non-first from the half-diffusivity case while the dashed red one is the first. The left figure shows the traces at the top of the density pedestal while the right one is at the maximum of the pressure gradient.

MHD diagram

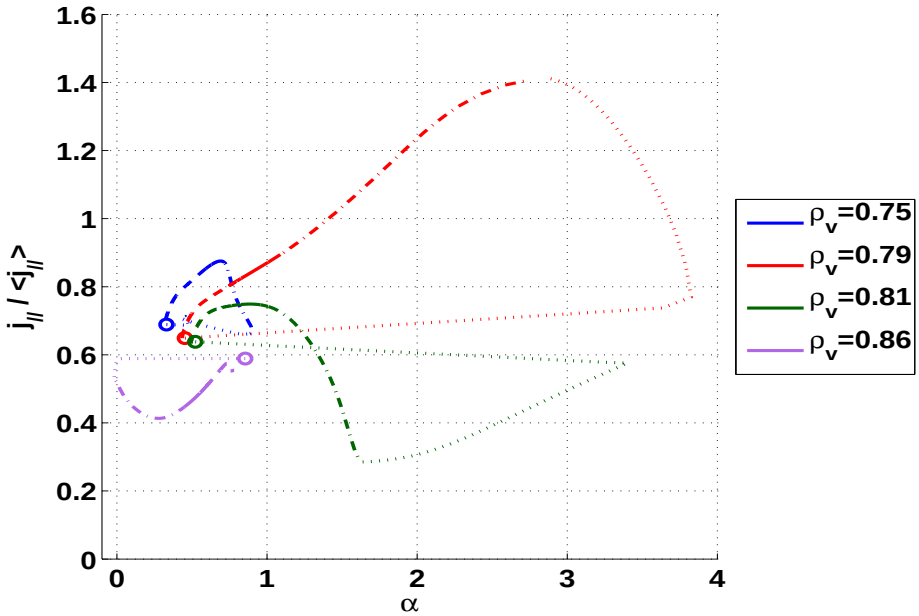

Figure C.16: $j - \alpha$ diagram for the first ELM cycle of the "Dn05" case. Dotted lines are during the ELM crash $0 \leq t < 0.1$, dash-dotted is for $0.1 \leq t < 0.5$, solid lines are $0.5 \leq t < 1$ and dashed lines are from 1 to the next ELM (20) with the time in ms. $\rho_V = 0.75$ is the top of the density pedestal, $\rho_V = 0.79$ is where this diagram is the largest, $\rho_V = 0.81$ is the top of the temperature pedestal and $\rho_V = 0.86$ is the maximum of the pressure gradient.

C.3.4 Particle diffusivity divided by ten

Profiles

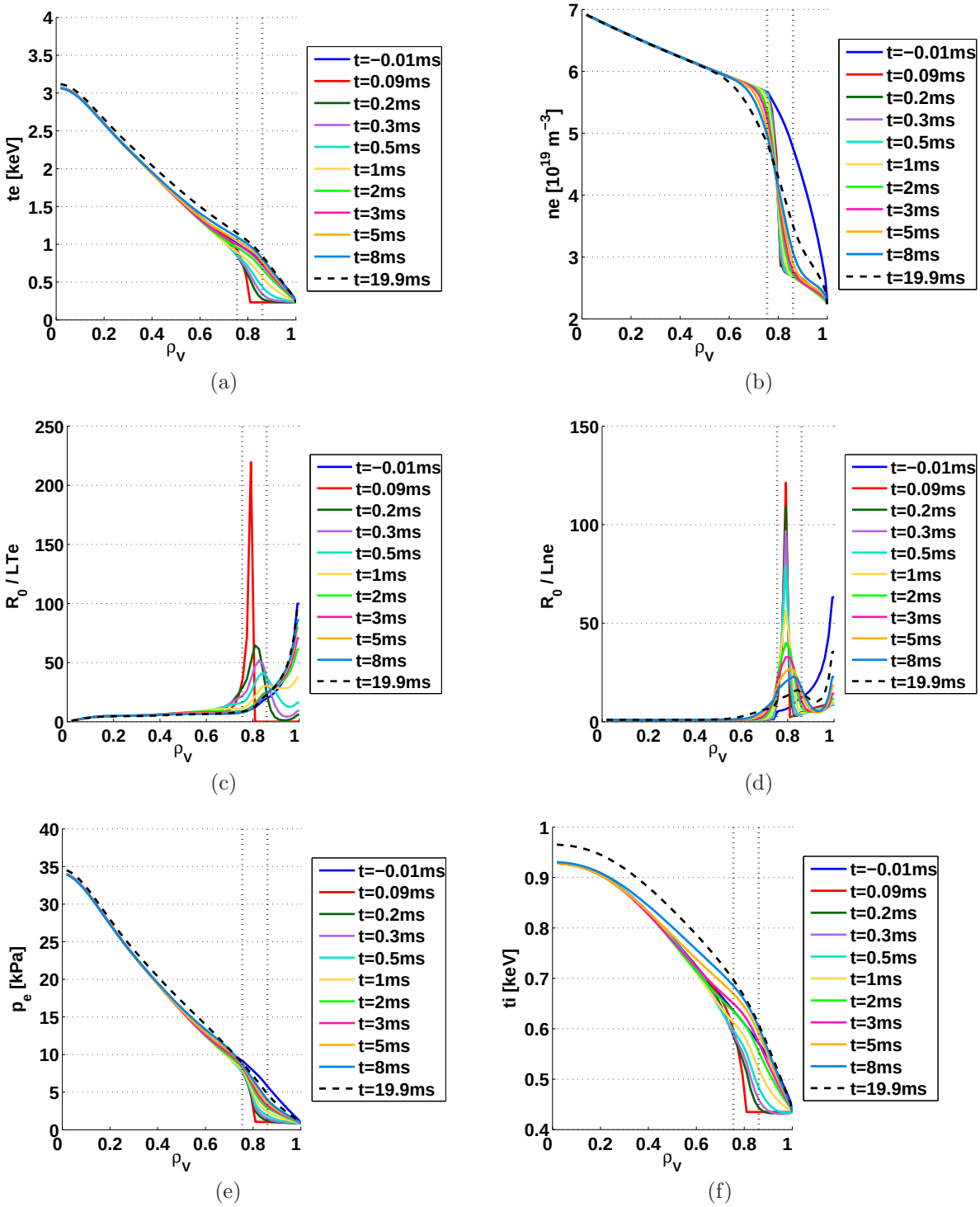

Figure C.17: Profiles of the main quantities for an inter-ELM for the case "Dn01" for the first ELM.

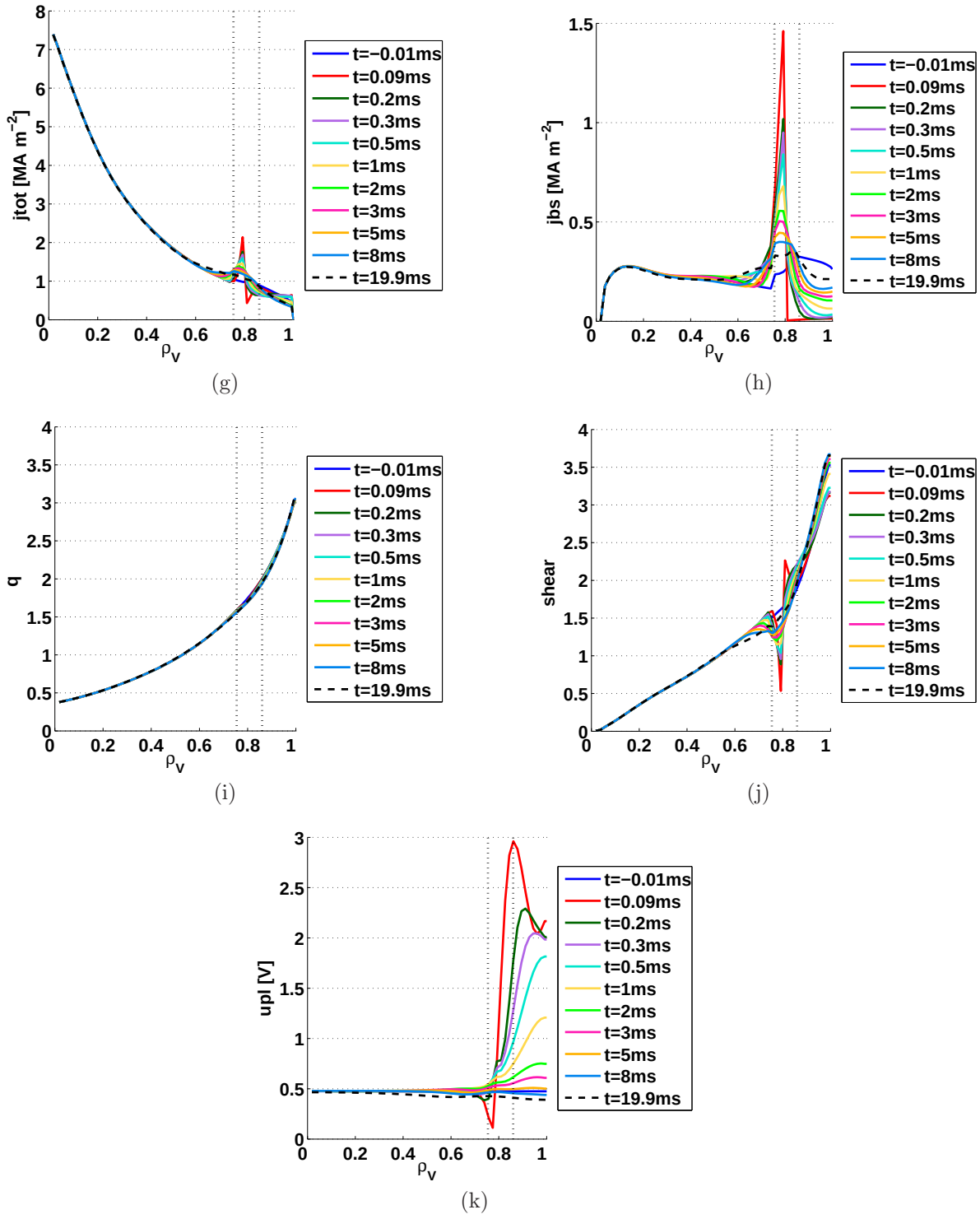

(g) (h) (i) (j) (k)

Figure C.17: Profiles of the main quantities for an inter-ELM for the case "Dn01" for the first ELM.

Time traces

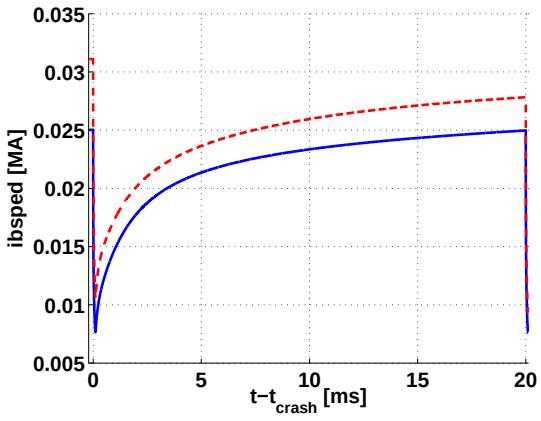

(a)

Figure C.18: Comparison between first and non-first ELM. The solid blue line is the non-first from the "Dn01" case while the dashed red one is the first. The left figure shows the traces at the top of the density pedestal while the right one is at the maximum of the pressure gradient.

MHD diagram

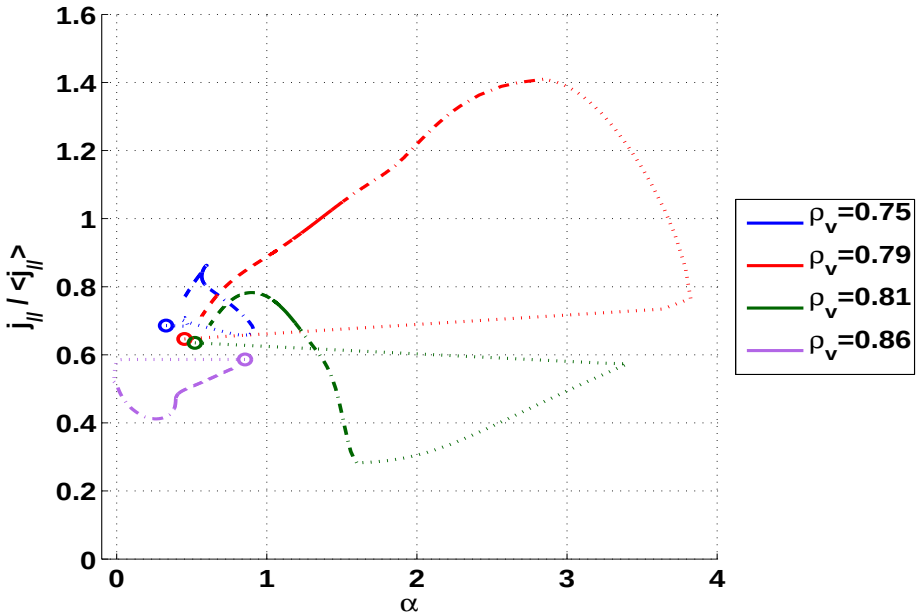

Figure C.19: $j - \alpha$ diagram for the first ELM cycle of the "Dn01" case. Dotted lines are during the ELM crash $0 \leq t < 0.1$, dash-dotted is for $0.1 \leq t < 0.5$, solid lines are $0.5 \leq t < 1$ and dashed lines are from 1 to the next ELM (20) with the time in ms. $\rho_V = 0.75$ is the top of the density pedestal, $\rho_V = 0.79$ is where this diagram is the largest, $\rho_V = 0.81$ is the top of the temperature pedestal and $\rho_V = 0.86$ is the maximum of the pressure gradient.

C.4 Comparing the change in D_n to that in the ELM period

C.4.1 Profiles

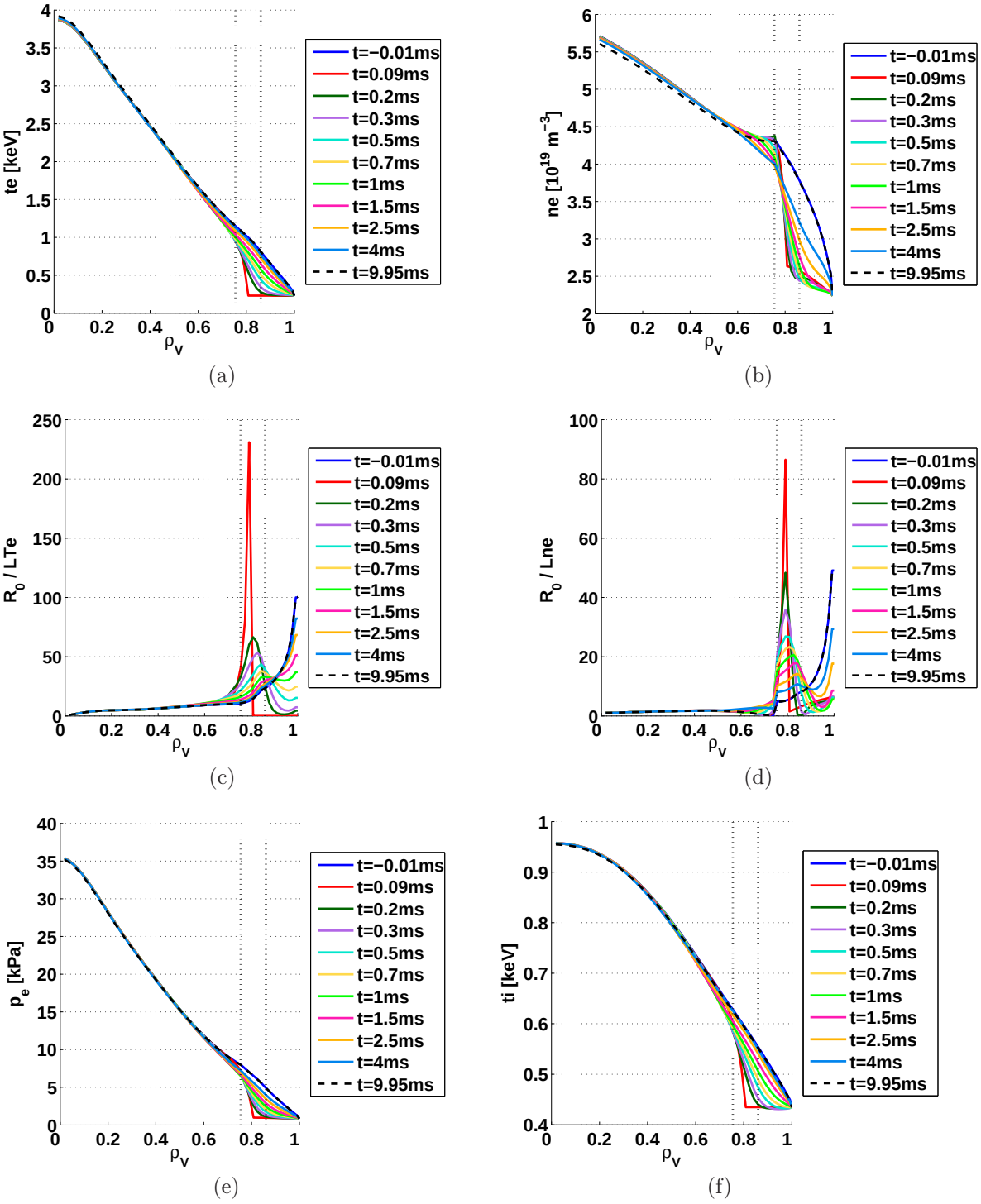

Figure C.20: Profiles of the main quantities for an inter-ELM for when dividing the ELM period by two.

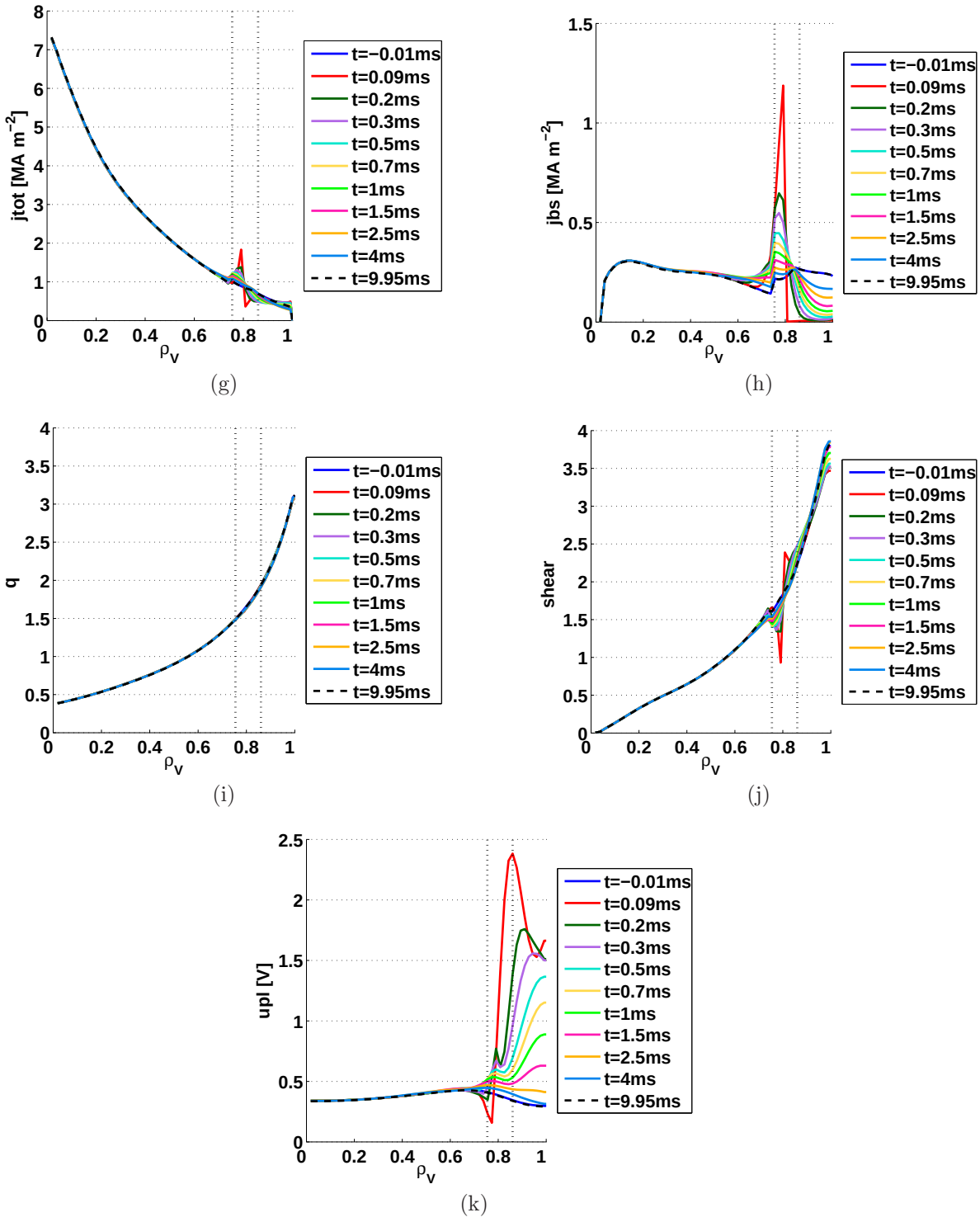

Figure C.20: Profiles of the main quantities for an inter-ELM for when dividing the ELM period by two.

C.4.2 Time traces

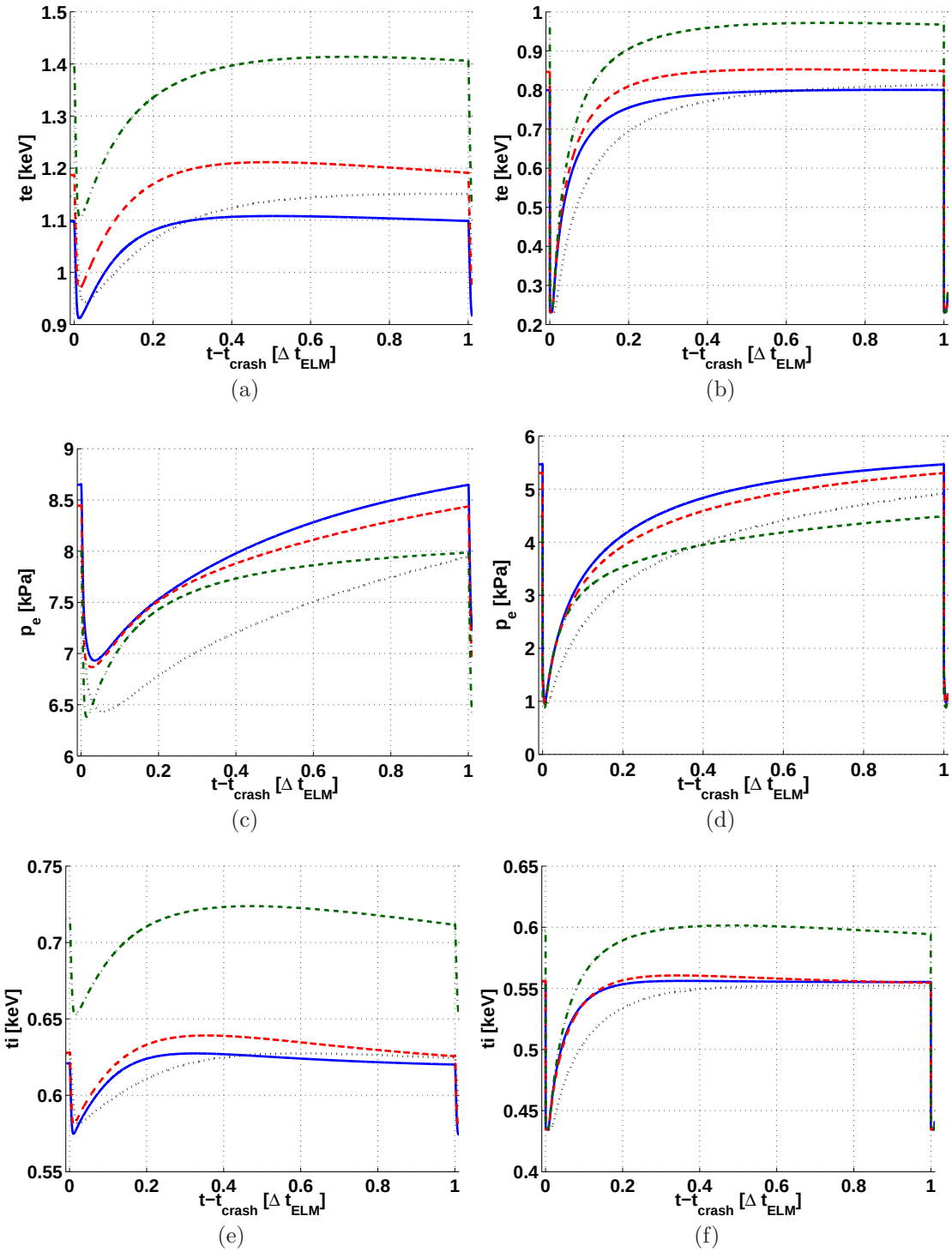

Figure C.21: Comparison between changing D_n and the ELM period. The left figures show the traces at the top of the density pedestal while the right ones are at the maximum of the pressure gradient.

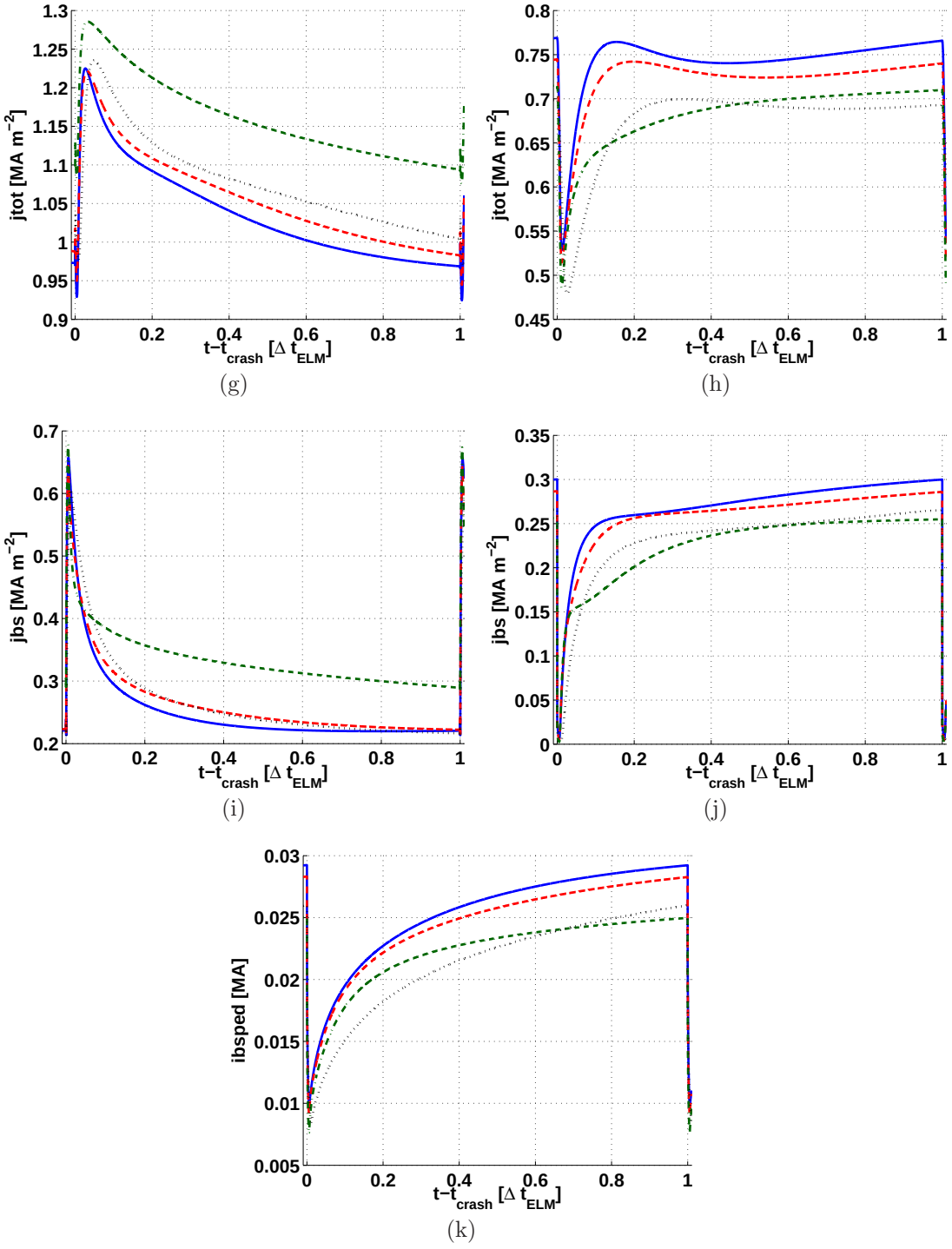

Figure C.21: Comparison between changing D_n and the ELM period. The left figures show the traces at the top of the density pedestal while the right ones are at the maximum of the pressure gradient.

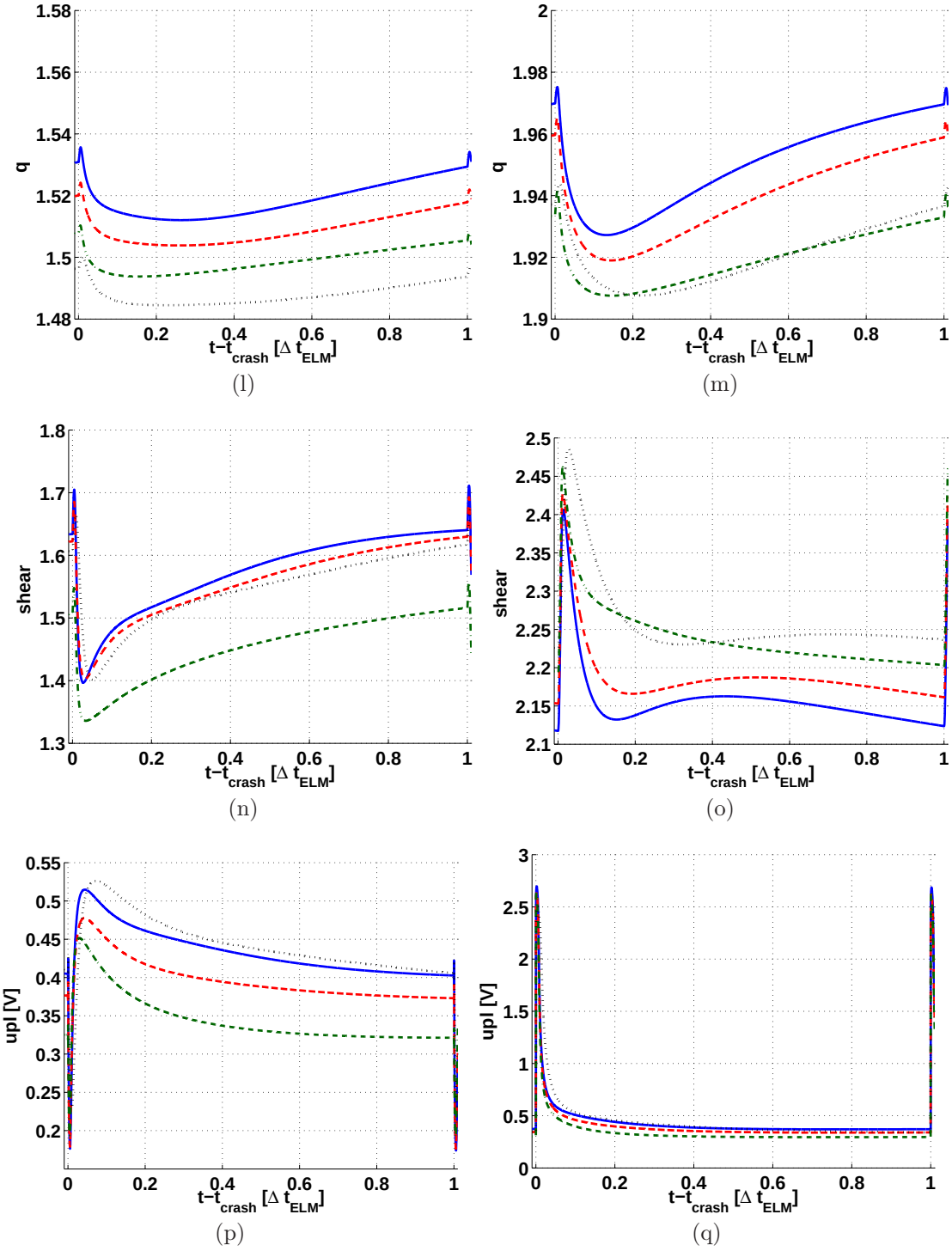

Figure C.21: Comparison between changing D_n and the ELM period. The left figures show the traces at the top of the density pedestal while the right ones are at the maximum of the pressure gradient.

C.4.3 MHD diagram

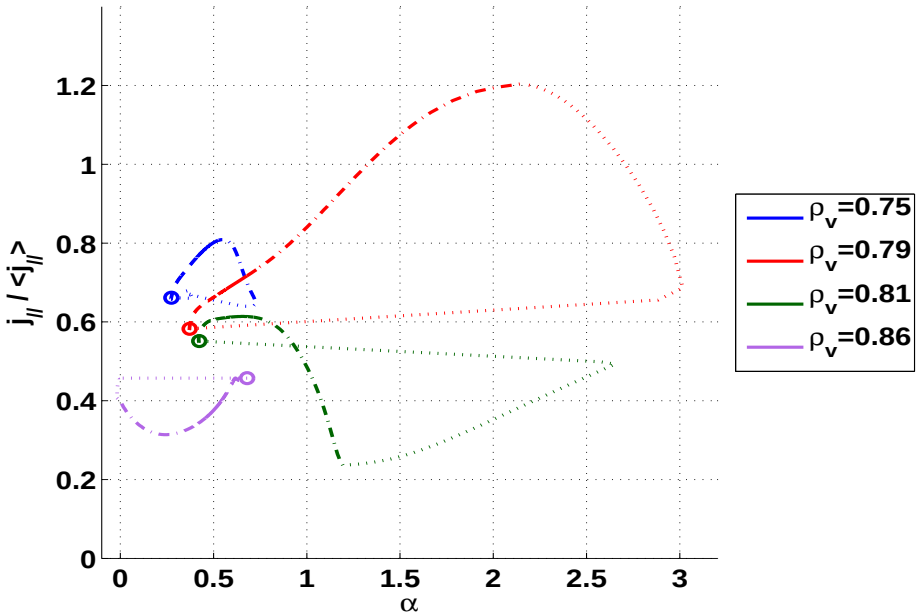

Figure C.22: $j - \alpha$ diagram for the ELM cycle with half the period. Dotted lines are during the ELM crash $0 \leq t < 0.1$, dash-dotted is for $0.1 \leq t < 0.5$, solid lines are $0.5 \leq t < 1$ and dashed lines are from 1 to the next ELM (10) with the time in ms. $\rho_V = 0.75$ is the top of the density pedestal, $\rho_V = 0.79$ is where this diagram is the largest, $\rho_V = 0.81$ is the top of the temperature pedestal and $\rho_V = 0.86$ is the maximum of the pressure gradient.

C.5 Doubling the ELM interaction region

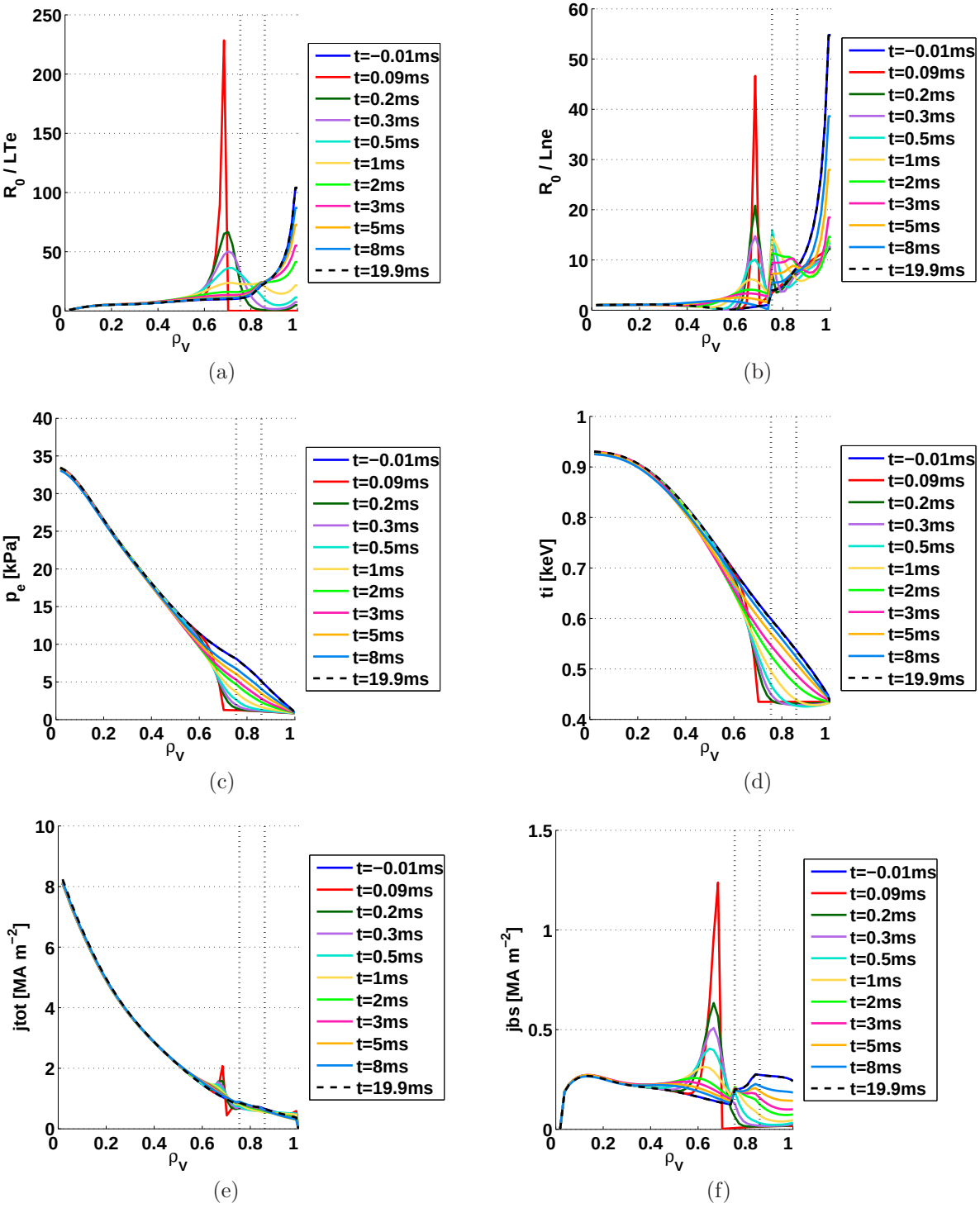

Figure C.23: Profiles of the main quantities for the case where we double the ELM range.

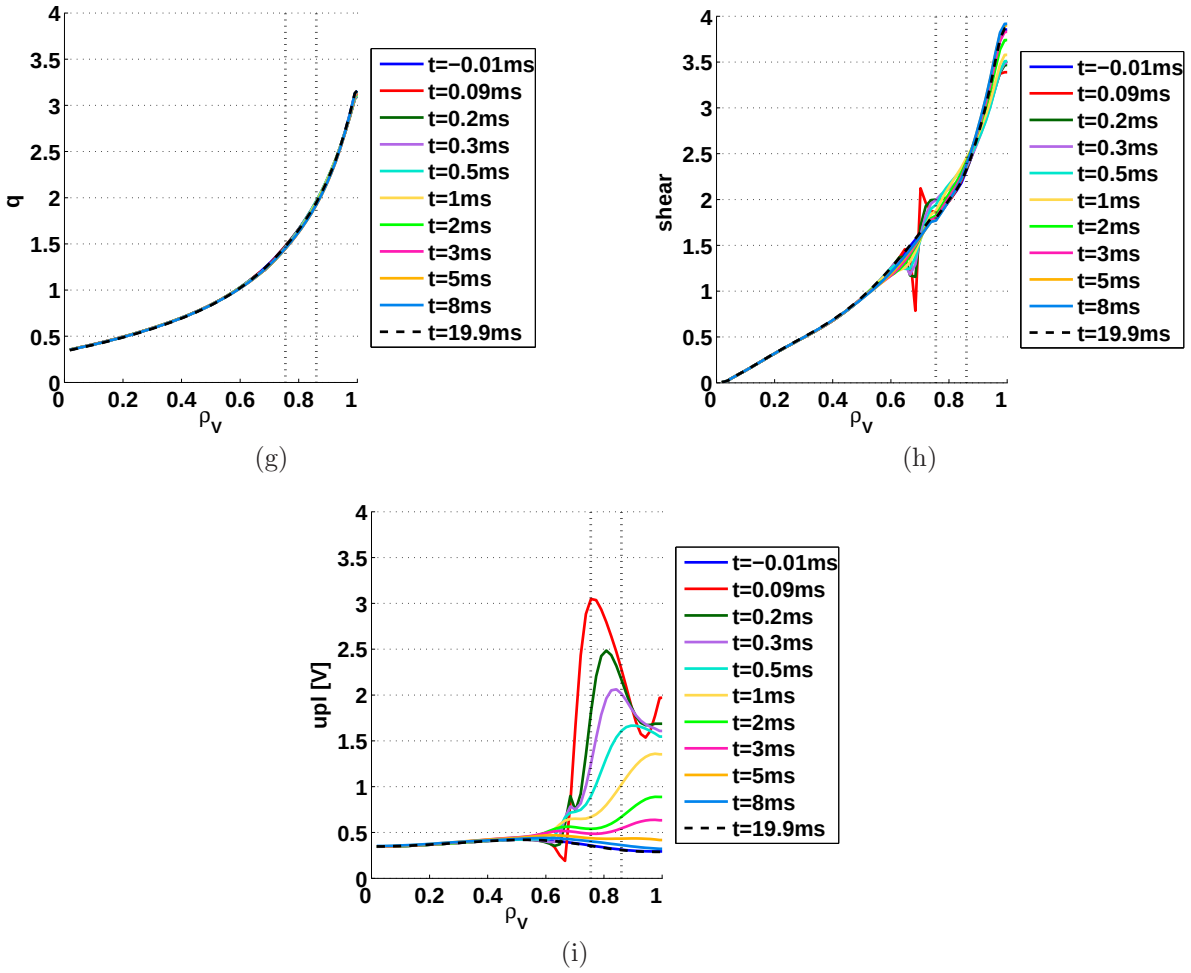

(g) (h)

(i)

Figure C.23: Profiles of the main quantities for the case where we double the ELM range.